



UiT The Arctic University of Norway

Faculty of Science and Technology
Department of Physics and Technology

On the linkage between atmospheric circulation changes and Arctic climate change

Tuomas Ilkka Henrikki Heiskanen

A dissertation for the degree of Philosophiae Doctor

April 2022



This thesis document was typeset using the *UiT Thesis L^AT_EX Template*.

© 2022 – <http://github.com/egraff/uit-thesis>

Abstract

Polar amplification is a prominent feature of recent and projected climate change. The Arctic region shows some of the strongest signs of climate change, including sea-ice retreat and temperatures increasing at twice the rate averaged over the northern hemisphere. A major concern for humanity is the sea-level rise associated with the melting of the ice-sheets and glaciers due to climate change. The atmospheric circulation transports an amount of energy into to the Arctic equivalent that received by the Arctic from the Sun. Thus, the atmospheric energy transport is an important subject to study in the light of Arctic climate change. The atmospheric energy transport may be decomposed into contributions by planetary-scale waves such as Rossby waves and small-scale waves such as cyclones. The energy transport contributions by the different length-scale separated systems are shown to affect the Arctic differently. The meridional energy transport is separated into length-scale contributions using a Fourier-series-based approach. Here we evaluate this approach by comparing it to a novel wavelet-based length-scale decomposition, developed as a part of this project. Further a machine-learning-based length-scale decomposition approximator is developed. The approximator may be applied to climate model output to investigate future changes in the length-scale decomposed energy transport. From the comparisons it is apparent that both the Fourier and wavelet-based length-scale decompositions are skilled approaches, which produce physically meaningful decompositions. Additionally, the Fourier-based decomposition is further developed to yield a length-scale decomposition on a latitude-longitude grid. Once evaluated the Fourier and wavelet-based decompositions are applied to investigate the effects of recent climate change on the atmospheric energy transport, and how these changes affect the Arctic and the Greenland ice-sheet. Through these studies it is conspicuous that shifts of energy transport between length-scale components has occurred during the last decades, and that these shifts have contributed to Greenland ice-sheet melt and Arctic warming.

Acknowledgements

Finally, this project is coming to an end. On my first year of the research project I had yet no idea what these years would contain. I have met a lot of interesting and knowledgeable people, published papers, been teaching in several courses, partaken in courses, went to conferences, and experienced a global pandemic. Many of the events and experiences during the PhD-project were foreseeable, but I would never have guessed that a global pandemic would occur during my second year of the project. The pandemic lead to an acute change of working routines, where the offices were emptied and everyone was working from home. This lead to many challenges: an overlying fear of the unknown was apparent during the first few months, and the borders between work and free time were gone. This was challenging, but with the support of great colleagues within the research group, my family, and my girlfriend the lock down was bearable.

After a little over three years of research there is a number of people I would like to thank. First and foremost Rune, my main supervisor, it has been an honor to work with you and learn from you. This project would not have been possible if it was not for your efforts. Thank you for all the time you have invested in discussions and collaboration with me. I have been lucky to be part of a research group which has been growing tremendously during the last years, it has been a pleasure to get to know all of you. I am especially grateful for having had the opportunity to collaborate with Johanne, it has been great to have someone else working on the same topic as me, which is not something that is given during a PhD-project. I am extremely grateful for the collaborations with the co-authors the papers written during this project, and Richard Bintanja, my co-supervisor, for the valuable insights to this thesis.

I want to thank my family and friends for being there throughout these years. Karoline, my girlfriend and best friend, thanks for your love and support. I could not have done this without you.

Contents

Abstract	i
Acknowledgements	iii
List of Figures	vii
1 Introduction	1
1.1 Outline	3
1.2 Atmospheric circulation	3
1.2.1 Hadley circulation	4
1.2.2 Eddies	4
1.2.3 Energy transport	5
2 Energy transport decompositions	7
2.1 Transient and stationary eddies	8
2.2 Fourier decomposition	10
2.2.1 Latitude-longitude-resolved length-scale decomposition	16
2.2.2 Convergence of energy transport	18
2.2.3 Decorrelation of length-scale components	19
2.3 Wavelet decomposition	21
2.4 Machine learning for length-scale decomposition	26
2.4.1 Residual networks	27
2.4.2 Machine-learning-based length-scale decomposition .	27
3 Thesis objectives	29
3.1 Evaluation and development of length-scale decompositions	29
3.2 Effects of energy transport changes on Arctic climate	30
4 Summary of papers	31
4.1 Paper I	31
4.2 Paper II	33
4.3 Paper III	34
4.4 Paper IV	35

5 Main conclusion	37
6 Paper I	47
7 Paper II	63
8 Paper III	77
9 Paper IV	97

List of Figures

2.1	Timescale decomposition of the annual and zonal-mean total northward energy transport. The solid line (tot) is the total energy transport, the dash-dotted line (mc) corresponds to the energy transport by meridional circulation, the dashed line (se) to stationary eddy energy transport, and the dotted line (te) to the transport by transient eddies. The energy transport is computed from ERA5 data for the period 1979-2018.	9
2.2	As in Figure 2.1 but for latent heat transport.	10
2.3	As in Figure 2.1 but for dry-static energy transport.	11
2.4	Fourier decomposition of the annual and zonal mean total northward energy transport. The solid line (tot) is the total energy transport, the dash-dotted line (mc) corresponds to the energy transport by meridional circulation, the dashed line (pw) to planetary-scale eddy energy transport, and the dotted line (sw) to the transport by small-scale eddies. The energy transport is computed from ERA5 data for the period 1979-2018.	13
2.5	As in Figure 2.4 but for latent heat transport.	14
2.6	As in Figure 2.4 but for dry-static energy transport.	15
2.7	Average meridional total energy transport decomposed into length-scale components. The meridional energy transport contributions by (a) planetary-scale waves ($n = 0-3$) and (b) small-scale perturbations ($n \geq 4$). The transports are computed following Equation 2.18, however the zonally symmetric transport contribution is included in the planetary waves component. The transports are computed from ERA5 data for the years 1979-2018.	18
2.8	As in Figure 2.7 but for latent heat transport.	19

2.9	Average convergence of total energy transport decomposed into length-scale components. The energy transport convergence contributions by (a) planetary-scale waves ($n = 0-3$), (b) small-scale perturbations ($n \geq 4$), and (c) small-scale perturbations ($n \geq 4$) decorrelated with the planetary-scale waves. The transports are computed following Equation 2.20 and Equation 2.21, and the decorrelation is performed as described in Equation 2.22 and Equation 2.23. The transports are computed from ERA5 data for the years 1979-2018. . . .	20
2.10	Haar-wavelet decomposition of the annual and zonal mean total northward energy transport. The solid line (tot) is the total energy transport, the dash-dotted line (mc) corresponds to the energy transport by meridional circulation, the dashed line (pw) to planetary-scale eddy energy transport, and the dotted line (sw) to the transport by small-scale eddies. The energy transport is computed from ERA-Interim data for the period 1979-2018.	23
2.11	As in Figure 2.10 but for latent heat transport.	24
2.12	As in Figure 2.10 but for dry-static energy transport.	25
2.13	Example of a classical and residual convolutional block. In an classical convolutional block (a) the input x passes through two convolutional weight layers and one activation before being passed to the final activation function. A residual block (b) works in the same manner as the classical block (a), but with the addition of a skip-connection, where the original input to the residual block is passed directly to the final activation function, together with the output of the last convolutional layer.	28



Introduction

Atmospheric energy transport is an important contributor for the Arctic heat budget, and therefore plays a major role with regards to Arctic climate and weather. The atmosphere transports energy from low latitudes to high latitudes due to the difference in absorbed solar insolation between equatorial and polar regions. The major part of the meridional heat transport into the Arctic is accomplished by the atmosphere, whilst the ocean only contributes a minor part of the total heat transport (Trenberth and Caron 2001).

Variability of the atmospheric energy transport at the Arctic boundary affects the Arctic temperatures (Graversen 2006; Graversen et al. 2008). Hence long-term changes in the atmospheric energy transport at the Arctic boundary are impacting the Arctic climate. The coupling between energy transport and the Arctic climate is understood only to a limited extent. This coupling is complex because different forms of energy will affect the Arctic differently. Transport of sensible heat directly affects Arctic temperatures, whilst moisture transport affects Arctic temperatures both through the direct increase in heat content and by increasing the greenhouse effect. Energy transport may affect the Arctic climate in various ways depending on where in the Arctic the energy is transported. For instance, heat transport over thin sea ice compared to over thick sea-ice may lead to more sea-ice retreat and hereby to increased absorption of solar radiation and thus stronger Arctic warming.

Classically the atmospheric transport is decomposed by form of energy, latent heat or dry-static energy, and by the timescale of the circulation systems, tran-

sient or stationary eddies (Oort and Peixóto 1983; Peixóto and Oort 1992). However, these decompositions does not specifically account for the type of dynamical system that transports the energy. The length-scale of systems transporting energy may have a large impact on how far and where in the Arctic the energy is transported. By applying a Fourier-series-based approach one may decompose the energy transport into contributions by different length scales (Graversen and Burtu 2016). The Fourier approach differs from the classical transient and stationary eddy decomposition as it does not consider the timescale of the systems, only the length scale. The length-scale decomposition splits the meridional energy transport into contributions by planetary scale waves such as Rossby waves, and small-scale waves such as cyclones. In general the planetary component of the meridional energy transport is a larger contributor to Arctic warming than its small-scale counterpart (Baggett and Lee 2015; Graversen and Burtu 2016). Planetary-scale waves have also been shown to impact Arctic sea-ice more strongly than their small-scale counterpart (Hofsteenge et al. 2022). However, the interactions between planetary and small-scale waves also play an important role in Arctic climate change. Constructive or destructive interference of the multi scale waves may lead to completely different energy transports into the Arctic (Messori and Czaja 2014; Messori et al. 2018; Lembo et al. 2019).

The climate is changing, anthropogenic emissions of greenhouse gases, such as CO₂ (Callendar 1938), has led and leads to an increase of the Earth surface temperature (Zhong and Haigh 2013). The Arctic region has warmed at a rate almost twice the rate of the averaged northern hemisphere (Graversen et al. 2008; Serreze and Barry 2011; Cohen et al. 2014). The warming Arctic leads to a diminishing energy gradient between the high and low latitudes, which indicates that the total energy meridional energy transport will decrease. However, when considering the components of the energy transport, both based on type of energy and length-scale, these are not all decreasing (Graversen and Burtu 2016).

Previous studies have argued that the latent heat transport into the Arctic impacts sea-ice, Arctic temperatures and the general Arctic climate (Graversen et al. 2008; Graversen et al. 2011; Kapsch et al. 2013; H.-M. Kim and B.-M. Kim 2017). However, in future climate-change scenarios the energy transport into the Arctic in some models is projected to decrease (Hwang et al. 2011). Although the total meridional energy transport into the Arctic is projected to decrease in a warmer climate, the contributions by the different length-scales may be shifted from one scale to another leading to a compensation of the cooling effect induced by the transport decrease (Graversen and Burtu 2016). Since the transport contributions by different length-scales likely affect the Arctic climate differently the length-scale decompositions are important tools for the evaluation of energy transport change effects on the Arctic climate (Baggett

and Lee 2015; Graversen and Burtu 2016; Heiskanen et al. 2020; Rydsaa et al. 2021; Hofsteenge et al. 2022; Heiskanen et al. 2022a).

The Greenland ice-sheet – one of the largest ice-sheets on the Earth – is found in the Arctic region. Mass loss from the Greenland ice-sheet is one of the main contributors to sea-level rise during the last decades (Rignot et al. 2011; Khan et al. 2014), and the Greenland melting is projected as an important contributor to sea-level rise in a warming climate. During the last decades the Greenland ice-sheet has lost mass at an accelerating rate (Mouginot et al. 2019; Shepherd et al. 2020). The exact processes leading to the increased mass loss is not yet fully understood. However, the atmospheric circulation likely plays an important role in the accelerating mass loss (Bevis et al. 2019; Shepherd et al. 2020; Heiskanen et al. 2022a).

1.1 Outline

This thesis is focused on the evaluation, development and applications of the Fourier-based length-scale decomposition proposed in Graversen and Burtu (2016), and the development of other length-scale decompositions. The remainder of this chapter presents an overview of the general circulation of the atmosphere, whilst Chapter 2 provides the theory of the Fourier-based energy-transport decomposition, other decompositions, and examples of applications of these decompositions. The objectives and scientific questions of this thesis are further described in Chapter 3. Summaries of the included papers are presented in Chapter 4, and the main conclusions and future work in Chapter 5.

1.2 Atmospheric circulation

The general circulation of the atmosphere is driven by imbalances in solar insolation between high and low latitudes. The energy gradients produced by the large amounts of insolation at low latitudes, and small amounts at high latitudes lead to atmospheric motions. The general characteristics of the atmospheric circulation are latitude dependent, where the low latitude circulation is dominated by zonally symmetric circulation and the high latitudes by eddies.

1.2.1 Hadley circulation

The Hadley cell is a major zonally symmetric circulation cell dominating the circulation patterns at the equatorial region. The Hadley cell is a thermally direct circulation cell, where hot air rises at the equator and cold air descends in the subtropics (Hadley 1735). Hadley circulation is induced by the solar insolation at the equator heating the air. Once heated such that the air is unstable with regards to the saturated adiabatic lapse rate the air will rise. This yields the thermally direct Hadley circulation around the equator and the tropics. The Hadley cell stretches from the equator to approximately 25-30° North and South, and is at its strongest in the winter hemisphere where the energy gradient is the largest. In theory it would be possible for the general circulation of the atmosphere to be dominated by Hadley cells from the equator to the poles, if not for the Earth's rotation. Since the Earth is rotating such a wide cell would break down in the mid latitudes, where the Coriolis force becomes significant. In the mid-latitudes there is a wave-forced thermally indirect cell, where cold air rises and hot air descends, known as the Ferrel cell. However, whereas the Hadley cell is driven by vertical convection due to the influx of solar insolation at the equator the Ferrel cell is forced by eddies (Salustri and Stone 1983; Vallis 2017). The Ferrel cell is hence not a similar structure to the Hadley cell, where the flow is mostly zonally symmetric. The zonally symmetric flow breaks down at higher latitudes due to the Earth's rotation, and the main flow pattern is the meandering of the air currents.

1.2.2 Eddies

In the mid to high latitudes Rossby waves are one of the most dominant circulation patterns in the general atmospheric flow. Rossby waves form due to the Earth's rotation, and may develop due to orographic forcing or heating contrasts between e.g. land and sea. Both of these effects result in a meandering of the east-west flow set up by the Earth's rotation, which has a larger impact on the circulation in the mid to high latitudes than at the low latitudes due to the strength of the Coriolis force. In the northern hemisphere the meandering of the jet-stream is a dominant Rossby wave pattern due to the orographic forcing of the multiple mountainous regions. Additionally Rossby waves form due to temperature gradients in the intersection between warm and cold air (Rossby 1939).

Atmospheric eddies may form both due to orographic forcing and instabilities in the atmospheric flow. At high latitudes on the northern hemisphere the atmospheric flow is largely influenced by the large mountain regions. The orographic forcing leads to a meandering of the jet-stream, which is generated by the Earth's rotation. In the extra-tropics eddies are the dominant weather pat-

tern. The extra-tropical eddies also perform most of the atmospheric meridional energy transport at these latitudes.

1.2.3 Energy transport

As discussed earlier the general circulation of the atmosphere is generated due to radiative imbalances between the equator and the poles. The atmospheric circulation transports net energy towards the poles, reducing the differences in temperature between the insolation rich tropics and the polar regions.

Energy in the atmosphere is transported in multiple forms. The energy transport is typically separated into transport of dry-static energy and latent heat. The dry-static energy

$$D = c_p T + \frac{1}{2} v^2 + z g$$

consists of sensible heat $c_p T$, kinetic energy $\frac{1}{2} v^2$ and potential energy $z g$, whilst the latent heat component

$$Q = L q$$

is specific humidity q multiplied by the latent heat of condensation L .

The dry-static energy transport has a direct effect of increasing the temperature of the region wherein it is transported, whereas the latent heat has both a direct effect and an indirect effect. The indirect effect of latent heat is through the increased moisture content in the atmosphere in the regions where the latent heat is transported, which leads to increased downwelling long wave radiation. The latent heat transport also contributes moisture to cloud formation, which may have both a positive and negative effect on the radiative balance on the surface, depending on the localization of the clouds. Clouds have both a warming and cooling effect on the temperatures. The clouds reflect some of the incoming solar insolation, which yields a cooling effect. However, they also absorb and emit some of the longwave radiation from the Earth back towards the Earth's surface, which yields a warming effect. Clouds over bright surfaces, such as sea-ice or ice-sheets typically have a net positive effect on the radiative budget at the surface, since they do not increase the albedo over these regions. Oppositely clouds over darker regions such as ice-free oceans may result in a net decrease of incoming energy at the surface.

The dominating circulation patterns are also typically the main contributors to the poleward energy transport. At low latitudes the zonally symmetric Hadley circulation is the main contributor to poleward energy transport, whilst eddies are the main contributor at the mid to high latitudes.

/2

Energy transport decompositions

In this chapter several energy-transport decomposition methods are described. The classical decomposition into stationary and transient eddies is presented and compared to length-scale based decompositions (Oort and Peixóto 1983; Peixóto and Oort 1992). The Fourier-based decomposition proposed in Graversen and Burtu (2016) is presented in detail, and so is an alternative wavelet-based length-scale decomposition approach (Heiskanen et al. 2020). Additionally, the concept of a machine-learning-based length- decomposition estimator is presented (Heiskanen et al. 2022b).

These length-scale decompositions are presented as alternatives to the decomposition into stationary and transient eddies since the temporal decomposition alone is not enough to capture the transport by different kinds of dynamical systems (Graversen and Burtu 2016). In addition to the technicalities of the length-scale decompositions the importance of these, and how they differ from the classical temporal decomposition, are discussed in this chapter.

2.1 Transient and stationary eddies

The meridional energy transport is classically decomposed by considering the timescales of the dynamical systems transporting energy using a Reynolds decomposition (Palmén and Vuorela 1963; Oort and Peixóto 1983; Peixóto and Oort 1992). Here the timescale decomposition is used to consider zonally averaged fields

$$[A] = \frac{1}{2\pi} \int_0^{2\pi} A \, d\lambda \quad (2.1)$$

where A is an arbitrary atmospheric field and λ is longitude in radians. The decomposition, as presented in Peixóto and Oort (1992), is based on zonal averages (Equation 2.1) and time averages

$$\bar{A} = \frac{1}{T} \int_0^T A \, dt, \quad (2.2)$$

where T is a given timescale. Any given atmospheric field may be defined as a time average (Equation 2.2) or zonal average (Equation 2.1) and perturbations to the averages such that

$$A = [A] + A^*, \quad [A^*] = 0, \quad (2.3)$$

$$A = \bar{A} + A', \quad \bar{A}' = 0. \quad (2.4)$$

The meridional energy transport is based on a product of the meridional winds v and energy field E . Expanding v and E in terms of zonal means and perturbations (Equation 2.3) to the zonal mean, and computing the zonal mean yields;

$$[vE] = [v] [E] + [v^* E^*]. \quad (2.5)$$

Here $[v^* E^*]$ is proportional to the zonal covariance of v and E . The timescale of the systems contributing to the meridional energy transport may be investigated by expressing v and E in Equation 2.5 in terms of the time average and perturbations, and applying the time average operator (Equation 2.2) to the zonal mean (Equation 2.5);

$$\overline{[vE]} = \overline{[v]} \overline{[E]} + \overline{[v^* E^*]} + \overline{[v' E']}. \quad (2.6)$$

The mean meridional energy transport, the left hand side of Equation 2.6, is thus decomposed into three timescale based components. The first component of the right hand side of Equation 2.6 is the mean meridional circulation component, the second component is the stationary eddies, and the third component the transient eddies. Note that the separation of eddy transport into transient and stationary eddies is dependent on the averaging period T used in the time average operator (Equation 2.2). The averaging period is usually a month, implying that the stationary eddies correspond to monthly scale variations

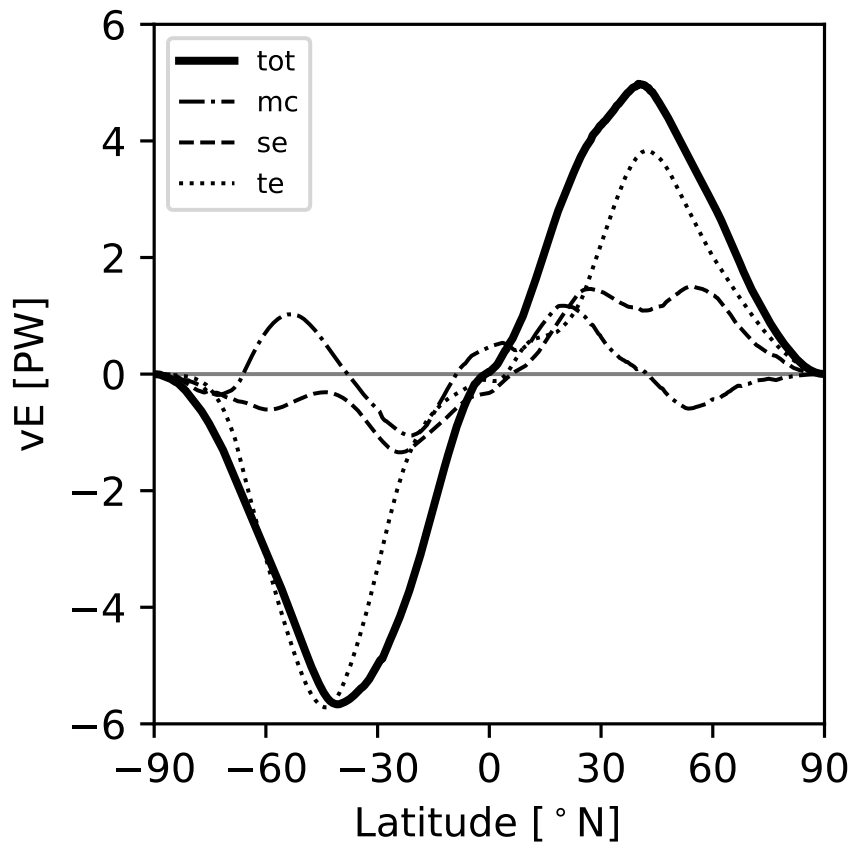


Figure 2.1: Timescale decomposition of the annual and zonal-mean total northward energy transport. The solid line (tot) is the total energy transport, the dash-dotted line (mc) corresponds to the energy transport by meridional circulation, the dashed line (se) to stationary eddy energy transport, and the dotted line (te) to the transport by transient eddies. The energy transport is computed from ERA5 data for the period 1979-2018.

and the transient eddies to faster variations in the energy transport (Oort and Peixóto 1983; Peixóto and Oort 1992).

In terms of annual mean meridional energy transport, the transient eddies dominate the total (Figure 2.1), latent heat (Figure 2.2) and dry-static energy transports (Figure 2.3) in the extra tropics (Oort and Peixóto 1983; Peixóto and Oort 1992; Dufour et al. 2016). Around the equatorial region the meridional circulation is the main contributor to poleward energy transport, where the Hadley cell is the most dominant circulation system. Across several modern reanalysis data sets the transient eddies account for up to 94% of the moisture fluxes across 70° N (Jakobson and Vihma 2010; Dufour et al. 2016). Classically the transient eddies are associated with small-scale perturbations such as

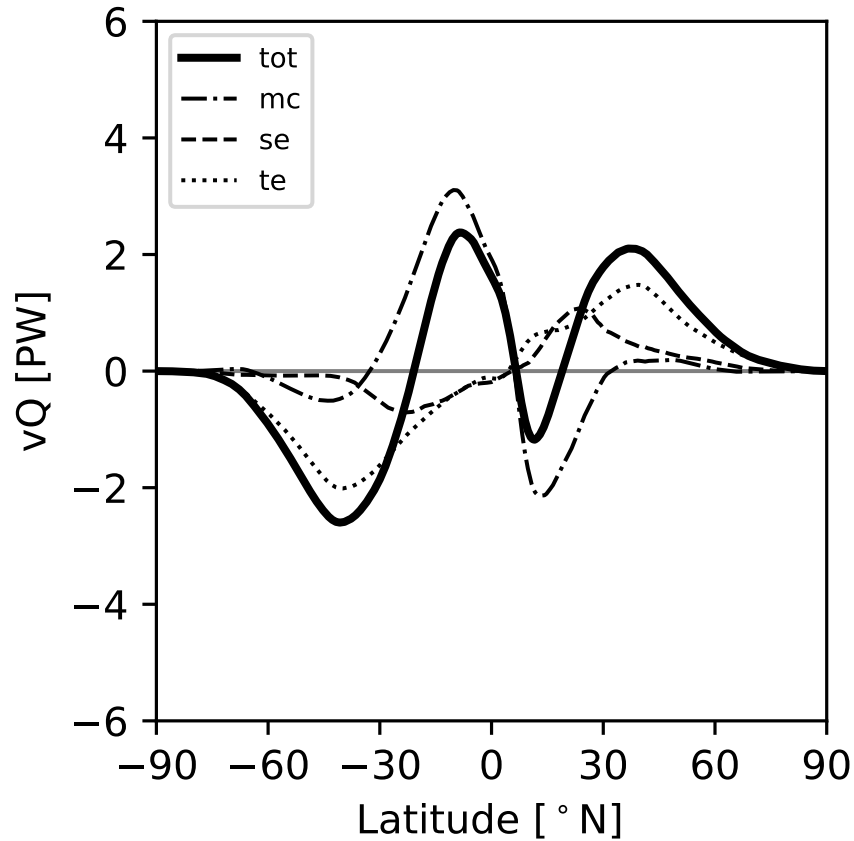


Figure 2.2: As in Figure 2.1 but for latent heat transport.

cyclones, and the stationary eddies with planetary-scale structures such as Rossby waves. However, this is in fact not always the case. Inherently the timescale decomposition (Equation 2.6) does not contain any length scale information of the energy transporting eddies. Cyclones are typically short lived, and thus assumed to yield a signal in the transient eddy energy transport. However, some regions are more prone to cyclone activity. The large cyclone activity in e.g. the Atlantic sector appears as a stationary eddy transport signal, although the individual cyclones are shorter lived than the stationary timescale (Graversen and Burtu 2016).

2.2 Fourier decomposition

An alternative approach to the classical decomposition described in Section 2.1 is a length-scale decomposition based on Fourier series as proposed by Graversen and Burtu (2016). Length-scale decompositions yield direct information

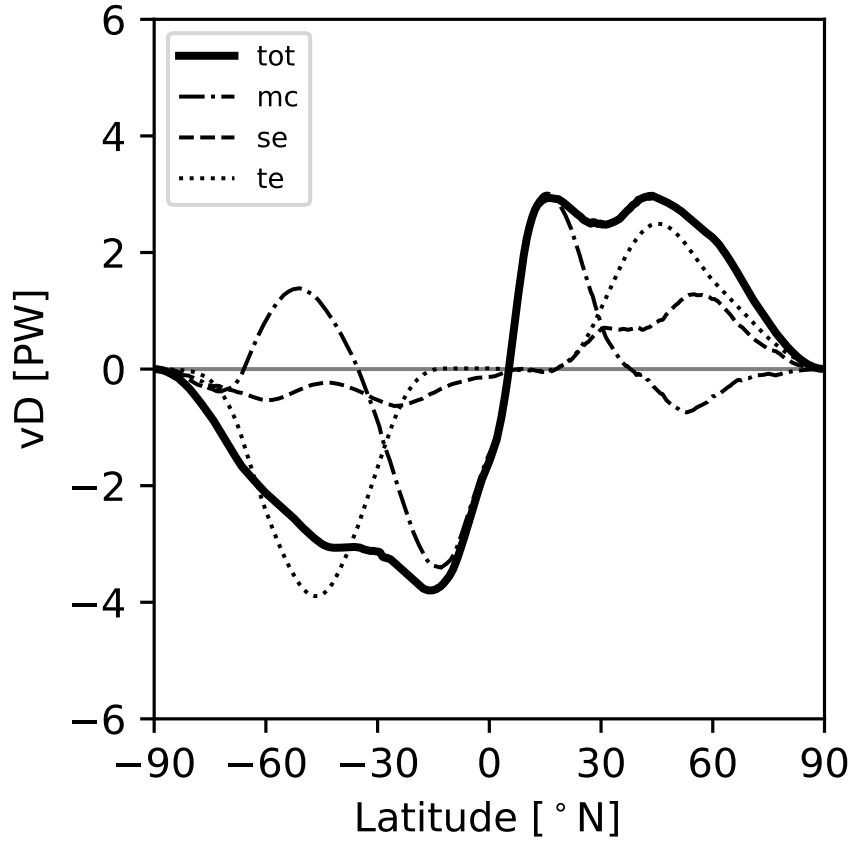


Figure 2.3: As in Figure 2.1 but for dry-static energy transport.

about the spatial extent of the energy transporting eddies. The length-scale decomposition proposed by Graversen and Burtu (2016) is based on a zonal Fourier series expansion of v and E . The zonal Fourier series for a general function is defined as

$$f(x) \sim \frac{a_0}{2} + \sum_{n=1}^{\infty} \left[a_n \cos\left(\frac{2\pi nx}{d}\right) + b_n \sin\left(\frac{2\pi nx}{d}\right) \right], \quad (2.7)$$

$$a_n = \frac{2}{d} \int_0^d f(x) \cos\left(\frac{2\pi nx}{d}\right) dx, \quad (2.8)$$

$$b_n = \frac{2}{d} \int_0^d f(x) \sin\left(\frac{2\pi nx}{d}\right) dx, \quad (2.9)$$

where $f(x)$ is a general function of x , x the coordinate along a latitude circle, $d = 2\pi a \cos(\phi)$ the length around the given latitude circle, n the wavenumber, a_n the Fourier cosine coefficients, and b_n the Fourier sine coefficients. Any periodic function may be approximated using Fourier series. As atmospheric

variables are periodic in the zonal direction the Fourier series expansion (Equation 2.7) is possible for any atmospheric variable.

The meridional energy transport averaged over the vertical column at a given latitude is

$$vE(\phi) = \int_0^{p_s} \oint v(\phi, x, p) E(\phi, x, p) dx \frac{dp}{g}, \quad (2.10)$$

where ϕ is latitude, p pressure, and g the gravitational acceleration. Considering one vertical layer of the atmosphere the meridional mass flux $v \frac{dp}{g}$ and energy field E may be expanded in terms of the Fourier series

$$v^l(\phi, x) \sim \frac{a_0^{v,l}}{2} + \sum_{n=1}^{\infty} \left[a_n^{v,l} \cos\left(\frac{2\pi nx}{d}\right) + b_n^{v,l} \sin\left(\frac{2\pi nx}{d}\right) \right] \quad (2.11)$$

and

$$E^l(\phi, x) \sim \frac{a_0^{E,l}}{2} + \sum_{n=1}^{\infty} \left[a_n^{E,l} \cos\left(\frac{2\pi nx}{d}\right) + b_n^{E,l} \sin\left(\frac{2\pi nx}{d}\right) \right], \quad (2.12)$$

where $a_n^{v,l}$ and $b_n^{v,l}$ are the Fourier coefficients of the meridional mass flux, and $a_n^{E,l}$ and $b_n^{E,l}$ the Fourier coefficients of the energy at the discrete level l in the atmosphere. The Fourier coefficients in equations 2.11 and 2.12 are computed from equations 2.8 and 2.9 by inserting v^l and E^l for $f(x)$ respectively. By inserting v and E from equations 2.11 and 2.12 in Equation 2.10, discretizing the vertical integral, and performing the zonal integral all the cross terms across wavenumbers vanish, and we are left with

$$vE(\phi) = \frac{d}{2} \sum_{l=1}^L \left[\frac{a_0^{v,l} b_0^{v,l}}{2} + \sum_{n=1}^{\infty} \left(a_n^{v,l} a_n^{E,l} + b_n^{v,l} b_n^{E,l} \right) \right]. \quad (2.13)$$

Here L denotes the number of vertical layers in the discretization, which is dependent on the dataset on which the length-scale decomposition is applied. The expression in Equation 2.13 is the full meridional energy transport across a cross section of the atmosphere at latitude ϕ . The Fourier expansion of the meridional energy transport may be decomposed into length-scale contributions by splitting the wavenumber sum in Equation 2.13

$$vE(\phi)_m = \frac{d}{4} \sum_{l=1}^L a_0^{v,l} a_0^{E,l}, \quad (2.14)$$

$$vE(\phi)_p = \frac{d}{2} \sum_{l=1}^L \sum_{n=1}^3 \left(a_n^{v,l} a_n^{E,l} + b_n^{v,l} b_n^{E,l} \right), \quad (2.15)$$

$$vE(\phi)_s = \frac{d}{2} \sum_{l=1}^L \sum_{n \geq 4} \left(a_n^{v,l} a_n^{E,l} + b_n^{v,l} b_n^{E,l} \right). \quad (2.16)$$

Here $vE(\phi)_m$ (Equation 2.14) is the zonally symmetric (meridional) energy transport component, $vE(\phi)_p$ (Equation 2.15) the planetary-scale eddy contribution to the meridional energy transport, and $vE(\phi)_s$ (Equation 2.16) the small-scale eddy contribution to the energy transport. The length scale decomposition is complete, it incorporates the total meridional energy transport, just as the timescale decomposition. However, the separation between the planetary and small-scale systems is somewhat arbitrary. In Graversen and Burtu (2016), the suggested separation is between wavenumbers 5 and 6. However based on comparisons with a wavelet-based length-scale decomposition Heiskanen et al. (2020) suggests that a separation between wavenumbers 3 and 4 is more appropriate.

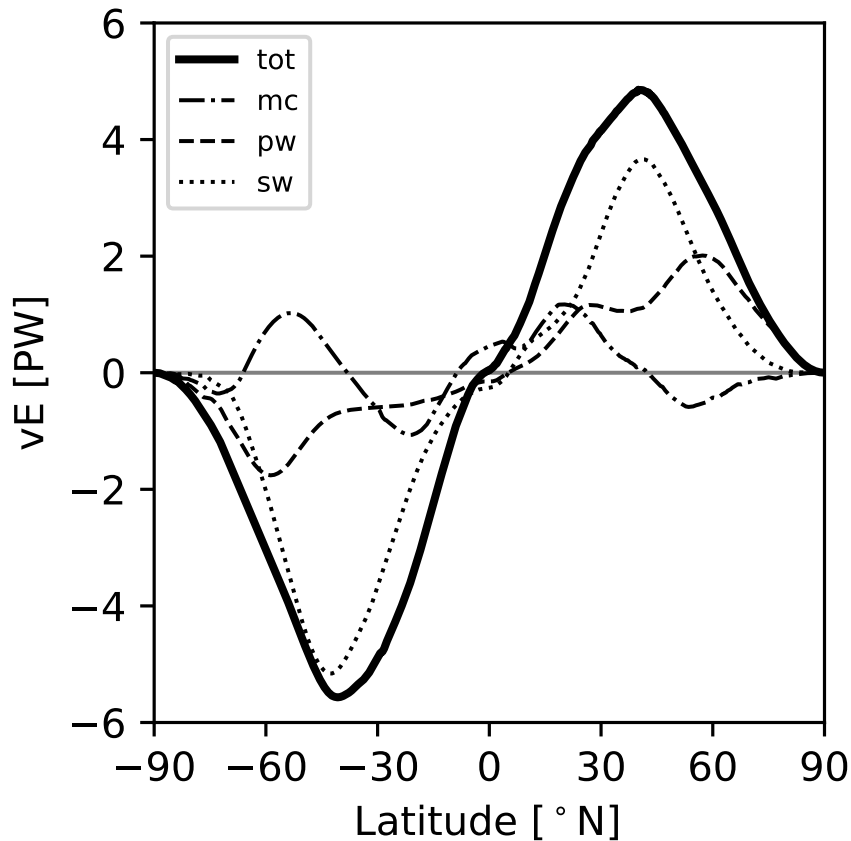


Figure 2.4: Fourier decomposition of the annual and zonal mean total northward energy transport. The solid line (tot) is the total energy transport, the dash-dotted line (mc) corresponds to the energy transport by meridional circulation, the dashed line (pw) to planetary-scale eddy energy transport, and the dotted line (sw) to the transport by small-scale eddies. The energy transport is computed from ERA5 data for the period 1979-2018.

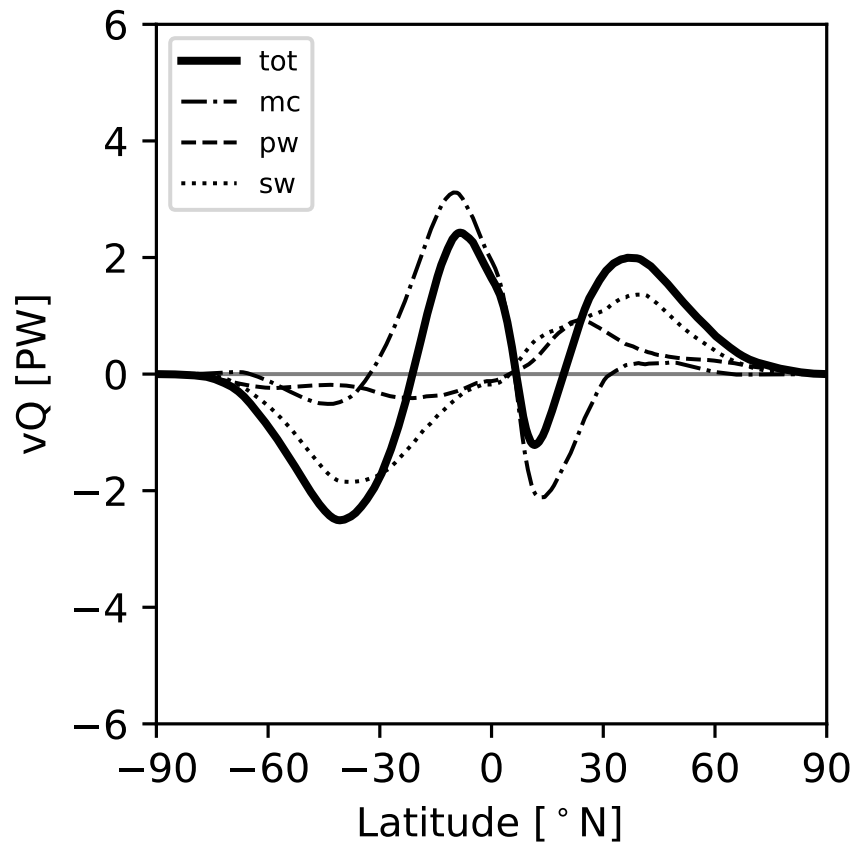


Figure 2.5: As in Figure 2.4 but for latent heat transport.

Figures 2.4-2.6 show the Fourier length-scale decomposition of the total energy transport (Figure 2.4), the latent heat transport (Figure 2.5), and the dry-static energy transport (Figure 2.6) computed from the ERA5 reanalysis (Hersbach et al. 2020). The reanalysis data set suffers from a mass flux inconsistency due to the data assimilation process (Trenberth 1991), hence a mass flux correction is applied to the meridional wind field before computing the energy transports (Graversen 2006).

In most regions the main contribution to the total energy transport is by the small-scale waves (Figure 2.4). The same applies for the latent heat transport (Figure 2.5) and the dry-static energy transport (Figure 2.6). However, at low latitudes the transport is dominated by the meridional circulation, as is the case with the timescale decomposition as well. At high latitudes the planetary-scale contribution becomes as important, or even more important, than the small-scale contributions for all types of transport. Comparing the Fourier-based length-scale decomposition to the timescale decomposition reveals that planetary-scale waves are not equivalent to stationary waves, and that transient

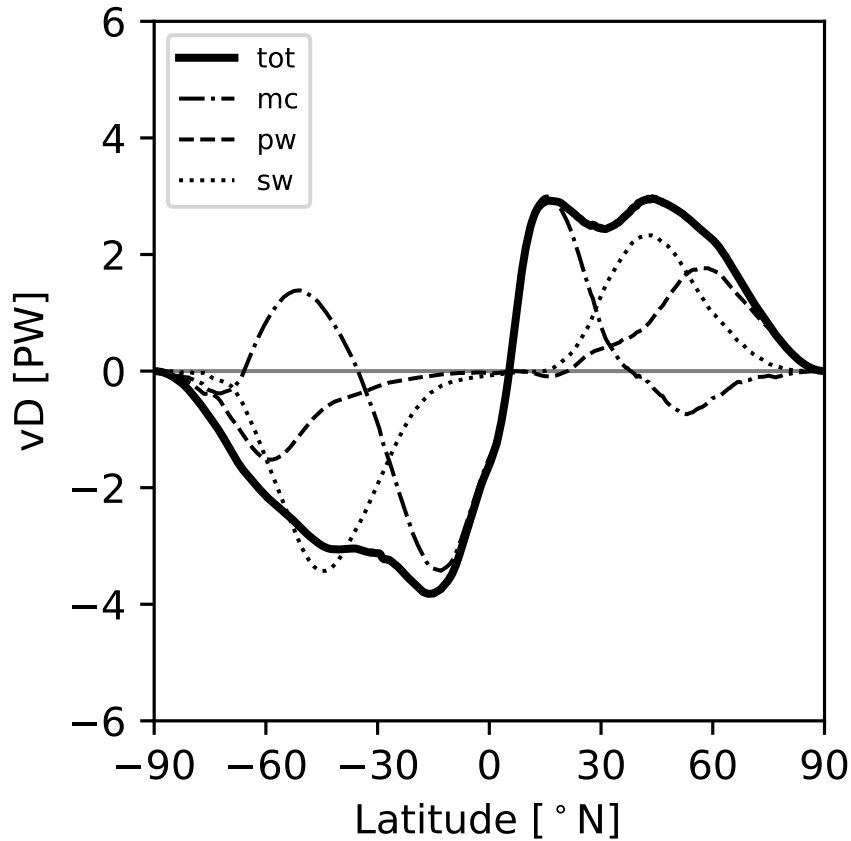


Figure 2.6: As in Figure 2.4 but for dry-static energy transport.

waves are not equivalent to small-scale waves.

Based on the Fourier-based length-scale decomposition it is evident that planetary-scale waves are a major contributor to the meridional energy transport across 70° N (Graversen and Burtu 2016; Heiskanen et al. 2020). This is somewhat contradictory to the notion that transient eddies, and thus synoptic cyclones, are the main contributor to the energy transport at high latitudes (Oort and Peixóto 1983; Jakobson and Vihma 2010; Dufour et al. 2016). However, this is not a contradiction based on the properties of the dynamical systems transporting energy, but a misinterpretation of the decomposition in stationary and transient eddies. As discussed in Section 2.1, planetary-scale waves, and small-scale cyclones as well, may be both transient and stationary. Hence, to establish the transport contributions of dynamical systems at different length scales, the timescale decomposition is insufficient and a length-scale decomposition is required.

Although the cross terms in Equation 2.13 vanish, there is still an interplay

between Rossby waves and small-scale systems, such as cyclones. The Rossby waves set circulation patterns which force the trajectories of cyclones, i.e. storm tracks (Fearon et al. 2021). Thus the transport components are not uncorrelated, which is associated with the multi scale attribute of fluid dynamics, perturbations propagate from small to large scale systems and vice versa.

The Fourier-based decomposition shows that planetary-scale waves affect Arctic temperature more strongly than the small-scale waves (Graversen and Burtu 2016; Heiskanen et al. 2020). However, it is likely that the contribution by small-scale waves is misrepresented in the Fourier-based decomposition. Multiple studies have shown the importance of cyclones in the moisture and thus latent heat transport into the Arctic (e.g. Messori et al. (2018) and Fearon et al. (2021)). A fallacy of the Fourier method when representing atmospheric systems is the non-localization of the basis functions. Small scale systems, such as cyclones, are often generated locally. A non-localized basis such as the Fourier basis is not well suited to represent localized systems correctly, there occurs a leakage of power towards the low wavenumbers (planetary-scales). Hence the validity of the Fourier-based length-scale decomposition should be tested, which is done by comparing it to an independent length-scale decomposition based on wavelets (Heiskanen et al. 2020).

2.2.1 Latitude-longitude-resolved length-scale decomposition

The zonally averaged meridional energy transport is an important quantity when studying the general Arctic climate (Graversen 2006; Graversen et al. 2011; Graversen and Burtu 2016). However, when the impacts of energy transport to specific regions in the Arctic is of interest the zonally averaged energy transport is not necessarily an accurate measure of incoming energy on a regional scale. One of the main concerns with climate change is the effects of the warming temperatures on the Greenland ice-sheet, as the Greenland ice-sheet is projected as one of the main contributors to sea-level rise in the future (Alley et al. 2005; Muntjewerf et al. 2020; Gregory et al. 2020). The ice-sheet is only a small region in the Arctic, which does not span throughout a latitude circle. To establish the effect of energy transport changes on the Greenland ice-sheet a possible pathway is to consider convergence of energy transport over the ice-sheet. To consider the length-scale decomposed energy transport convergence it is insufficient with the length-scale decomposed zonal-mean meridional energy transport. Hence, a length-scale decomposition on a latitude-longitude grid is needed to study the effects of energy transport on the Greenland ice-sheet (Heiskanen et al. 2022a).

The Fourier decomposition is also applicable to energy transport on a lati-

tude longitude grid (Rydsaa et al. 2021). By omitting the zonal integral from Equation 2.10, one may consider the vertically integrated energy transport as a function of latitude and longitude

$$vE(\phi, x) = \int_0^{p_s} v(\phi, x, p) E(\phi, x, p) \frac{dp}{g}. \quad (2.17)$$

The expression in Equation 2.17 is yet not decomposed into length-scale components. This may be done by applying Fourier series (Equation 2.7) on the mass flux field or the energy field. Decomposing both fields is unnecessary in this case, there is no zonal integral leading to vanishing cross-terms. Expanding the mass flux field in terms of its zonal Fourier series and discretizing the vertical integral yields;

$$vE(\phi, x) = \sum_{n=0}^{\infty} \sum_{l=1}^L E^l(\phi, x) \left\{ a_{n,\phi}^{v,l} \cos\left(\frac{2\pi nx}{d}\right) + b_{n,\phi}^{v,l} \sin\left(\frac{2\pi nx}{d}\right) \right\}. \quad (2.18)$$

Splitting the wavenumber sum in Equation 2.18 as in equations 2.14-2.16 yields a length-scale decomposition of the meridional energy transport resolved on a latitude longitude grid. Note that the zonal mean of Equation 2.18 yields the same decomposition as in Equation 2.13. The choice of decomposing the mass flux field or the energy field is somewhat arbitrary. However, the mass-flux field provides information of the dynamics of the circulation systems transporting the energy, and thus appears as the more appropriate field to describe a length-scale decomposition which represent the systems transporting energy.

The latitude longitude resolved decomposition into length scales may be used to investigate the localization of the energy transport by various systems. Hence one may pinpoint where the energy is transported. The main pathways of energy into the Arctic by planetary-scale waves are the Atlantic and Pacific sectors (Figure 2.7a). The small-scale circulation contributions has their main pathways of energy transport into the Arctic over land (Figure 2.7b), outside of the main sectors for the planetary-scale circulation. In the Atlantic and Pacific sectors the small-scale contributions has an opposing effect to the planetary-scale circulation. Unsurprisingly the main pathway for latent heat transport both by planetary-scale (Figure 2.8a) and small-scale perturbations (Figure 2.8b) is over the oceans. The main pathway of extreme latent heat transport into the Arctic both by small-scale and planetary-scale waves is found to be in the Atlantic sector between Greenland and Norway (Rydsaa et al. 2021). Furthermore the latitude longitude resolved length-scale decomposition may be used to determine regions of divergence and convergence of energy transport.

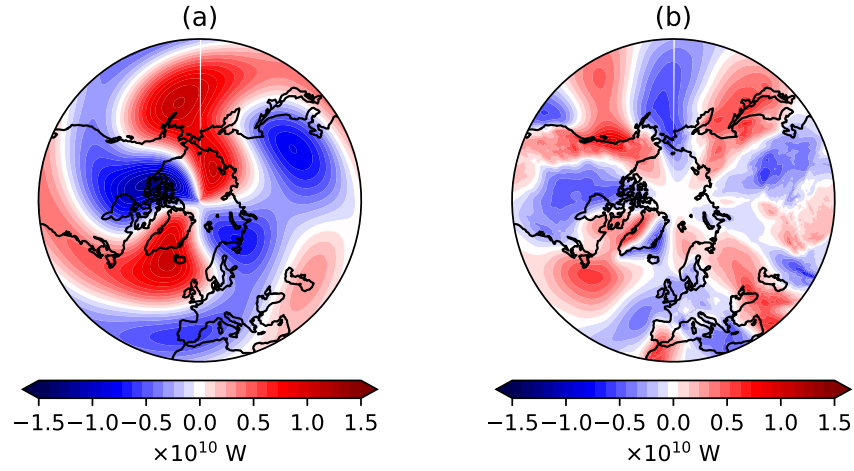


Figure 2.7: Average meridional total energy transport decomposed into length-scale components. The meridional energy transport contributions by (a) planetary-scale waves ($n = 0-3$) and (b) small-scale perturbations ($n \geq 4$). The transports are computed following Equation 2.18, however the zonally symmetric transport contribution is included in the planetary waves component. The transports are computed from ERA5 data for the years 1979-2018.

2.2.2 Convergence of energy transport

The energy transport convergence is defined as

$$E^{\text{conv}} = -\nabla \cdot \mathbf{v}E, \quad (2.19)$$

where $\mathbf{v}E = (uE, vE)$ is the vertically integrated energy transport vector and $\nabla \cdot$ the divergence operator. The convergence of energy transport is separated into length-scales by grouping wavenumbers $n = 0-3$ together as the large scale waves and $n \geq 4$ as the small-scale waves

$$E_p^{\text{conv}} = -\nabla \cdot \mathbf{v}E^{n \leq 3}, \quad (2.20)$$

$$E_s^{\text{conv}} = -\nabla \cdot \mathbf{v}E^{n \geq 4} \quad (2.21)$$

where $\mathbf{v}^{n \leq 3}$ refers to the sum of the Fourier components for wavenumbers less than or equal to three of the zonal and meridional mass-flux fields, and $\mathbf{v}^{n \geq 4}$ the same but for wavenumbers greater than or equal to four. The zonally symmetric component ($n = 0$) is included in the planetary-scale waves since the zonal component is actually of importance in high latitudes, and may be considered a part of the mean Rossby wave flow. For the meridional energy transport this is considered a separate component, however at high latitudes the symmetric meridional component is close to zero (Figure 2.4).

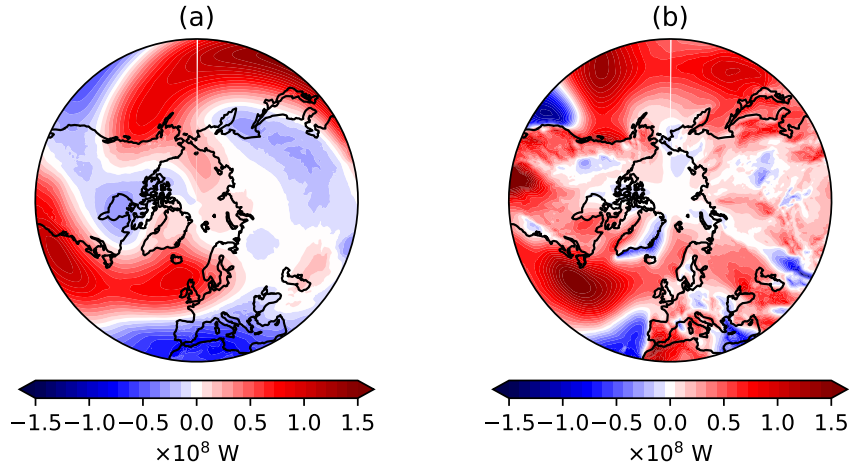


Figure 2.8: As in Figure 2.7 but for latent heat transport.

2.2.3 Decorrelation of length-scale components

Using the latitude longitude resolved length-scale decomposition one has to be aware of the temporal correlation between the components. The planetary-scale waves and small-scale perturbations are not independent in time. The large-scale flow alters the paths of small-scale cyclones, and a collection of cyclones occurring simultaneously may alter the large-scale Rossby waves. Hence, there is a temporal correlation between the planetary-scale and small-scale waves. To separate the effects of energy transport by the relevant scales one may decorrelate the planetary-scale and small-scale transport time series using regressions. By regressing e.g. the small-scale transport on the planetary-scale transport convergence

$$\beta_p^s = \frac{\text{cov}(E_s^{\text{conv}}, E_p^{\text{conv}})}{\text{var}(E_p^{\text{conv}})} \quad (2.22)$$

and subtracting the planetary-scale component multiplied by the regression coefficient (Equation 2.22) from the small-scale transport convergence

$$E_{s||p}^{\text{conv}} = E_s^{\text{conv}} - \beta_p^s E_p^{\text{conv}}, \quad (2.23)$$

the temporal correlation between the components is removed. The importance of the decorrelation between the transport convergence contributions by different scales is demonstrated in Figure 2.9. Figure 2.9a shows the time-average total energy-transport convergence by planetary-scale waves. It is evident that in multiple regions, the contribution by small-scale waves (Figure 2.9b) is directly anti-correlated to the planetary-scale wave contributions (Figure 2.9a). E.g. over Greenland and Norway the convergence pattern of

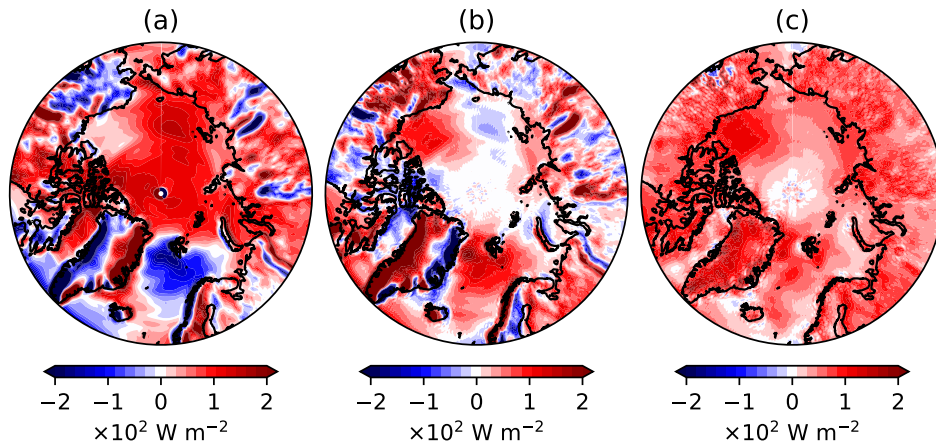


Figure 2.9: Average convergence of total energy transport decomposed into length-scale components. The energy transport convergence contributions by (a) planetary-scale waves ($n = 0-3$), (b) small-scale perturbations ($n \geq 4$), and (c) small-scale perturbations ($n \geq 4$) decorrelated with the planetary-scale waves. The transports are computed following Equation 2.20 and Equation 2.21, and the decorrelation is performed as described in Equation 2.22 and Equation 2.23. The transports are computed from ERA5 data for the years 1979-2018.

small-scale perturbations (Figure 2.9b) has an opposing pattern to the large-scale circulation (Figure 2.9a). However, when the small-scale perturbations are decorrelated from the large-scale circulation a different energy transport convergence pattern occurs (Figure 2.9c); Once the temporal correlation between the large-scale circulation and small-scale perturbations is removed the obvious dipole pattern between the planetary-scale waves (Figure 2.9a) and small-scale perturbations (Figure 2.9b) is removed, and what is left is the contribution by only the small-scale waves to the energy transport convergence (Figure 2.9c).

The decorrelation method is important to uncover the actual effects of energy-transport convergence by small-scale perturbations on the Greenland ice-sheet. If no decorrelation is applied the presumed effect of latent heat transport by small-scale perturbations on the surface-mass balance of Greenland is inconsistent with the increased moisture over the ice-sheet associated with cyclones. However, when the small-scale perturbations are decorrelated with the large-scale circulation the effect on the surface-mass balance makes sense, an increased moisture transport convergence is associated with an increase in the surface mass (Heiskanen et al. 2022a). Similarly the decorrelation method may be applied on other climate variables, e.g. surface-energy balance and precipitation. The surface-energy balance consists of radiative and turbulent

fluxes, where longwave radiative fluxes are associated with clouds and moisture in the atmosphere. Hence longwave radiative flux anomalies are associated with precipitation. When considering the effects of surface-energy balance on e.g. the surface-mass balance of the Greenland ice-sheet the observed effect is altered by the correlation with precipitation (Figure 1 of Heiskanen et al. (2022a)). This is conspicuous from the fact that precipitation over the Greenland ice-sheet is typically snow which has a positive (increase in mass) effect on the surface-mass balance, whilst positive longwave radiation anomalies typically melt the ice. By decorrelating the time-series of surface-energy balance and precipitation these effects may be separated, whereby physical linkages explored by the regression analyses are revealed (Heiskanen et al. 2022a).

2.3 Wavelet decomposition

The length-scale decomposition based on Fourier series has an inherent problem: the Fourier basis is non-localized. Studies based on the Fourier length-scale decomposition have shown the importance of energy transport by planetary-scale systems (e.g. Graversen and Burtu (2016)). However, by this study the importance of small-scale systems such as cyclones is likely underestimated due to the non-localized basis functions (Heiskanen et al. 2020). Cyclones are important contributors to the poleward energy transport, especially when it comes to the transport of latent heat (Messori et al. 2018). An alternative length-scale decomposition based on wavelet series can solve the localization problem.

Wavelets are described as "brief oscillations", they may be considered as localized waves within the defined domain. Wavelets come in multiple shapes, however the defining properties of a wavelet $\psi(x)$ is zero mean,

$$\int_0^d \psi(x) dx = 0, \quad (2.24)$$

and unit energy,

$$\int_0^d |\psi(x)|^2 dx = 1, \quad (2.25)$$

over the domain on which the wavelet is defined. The main properties of wavelets (equations 2.24 and 2.25) are not sufficient to build an orthonormal basis based on wavelets. Such a basis is needed to perform a complete, non-redundant length-scale decomposition of the meridional energy transport. The orthonormal basis is built from a family of wavelets by stretching and translating a given wavelet type (Daubechies 1992). To ensure that the energy of the wavelet

stays at unity through the stretching process, an amplitude scaling,

$$\psi_{j,k}(x) = 2^{j/2} \psi(2^j x - k), \quad j, k \in \mathbb{Z}, \quad (2.26)$$

is introduced. Here j is the scale index and k the translation index. The wavelets in Equation 2.26 are orthogonal given that they have the inner product

$$\langle \psi_{j,k}(x), \psi_{m,n}(x) \rangle = \int_0^d \psi_{j,k}(x) \psi_{m,n}(x) dx = \begin{cases} 1, & j, k = m, n \\ 0, & j, k \neq m, n \end{cases}. \quad (2.27)$$

Using a family of wavelets with an inner product as in Equation 2.27 we may decompose any given function $f(x)$ on the interval $x \in [0, d]$ in terms of a wavelet series

$$f(x) \sim \sum_{j=0}^{\infty} \sum_{k=0}^{2^j} c_{j,k} \psi_{j,k}(x), \quad (2.28)$$

where the coefficients $c_{j,k}$ are defined as

$$c_{j,k} = \langle f(x), \psi_{j,k}(x) \rangle = \int_0^d f(x) \psi_{j,k}(x) dx. \quad (2.29)$$

The similarities between the Fourier series (Equation 2.7) and the wavelet series (Equation 2.28) are evident. Both are complete non-redundant expansions of the original periodic function $f(x)$ on $x \in [0, d]$. The coefficients of both expansions are computed using defined inner products (Equations 2.8, 2.9, and 2.29). However, for a Fourier series we only have one set of sine and cosine basis functions. Whilst for the wavelet series the only imposed requirement on the basis functions is that they are wavelets (equations 2.24 and 2.25). A wavelet-based length-scale decomposition may be defined similarly as the Fourier-based decomposition. Expanding the mass-flux field $v \frac{dp}{g}$ and energy field E in terms of their wavelet series at each height level in the atmosphere, and inserting into the vertically discretized meridional energy transport yields

$$\begin{aligned} vE(\phi) &= \sum_{l=0}^L \overline{vE}_l(\phi) \\ &+ \sum_{l=0}^L \int_0^d \left(\sum_{j=0}^{\infty} \sum_{k=0}^{2^j} c_{j,k}^{v,l} \psi_{j,k}(\phi, x) \right) \left(\sum_{j'=0}^{\infty} \sum_{k'=0}^{2^{j'}} c_{j',k'}^{E,l} \psi_{j',k'}(\phi, x) \right) dx, \end{aligned} \quad (2.30)$$

where $\overline{vE}_l(\phi)$ is the zonally averaged energy transport component at level l , $c_{j,k}^{v,l}$ the wavelet coefficients of the mass-flux field, and $c_{j',k'}^{E,l}$ for the energy field. Due to the orthogonality of the wavelets (Equation 2.27) the cross terms $(j, k) \neq (j', k')$ in Equation 2.30 vanish, such that

$$vE(\phi) = \sum_{l=0}^L \left(\overline{vE}_l(\phi) + \sum_{j=0}^{\infty} \sum_{k=0}^{2^j} c_{j,k}^{v,l} c_{j,k}^{E,l} \right). \quad (2.31)$$

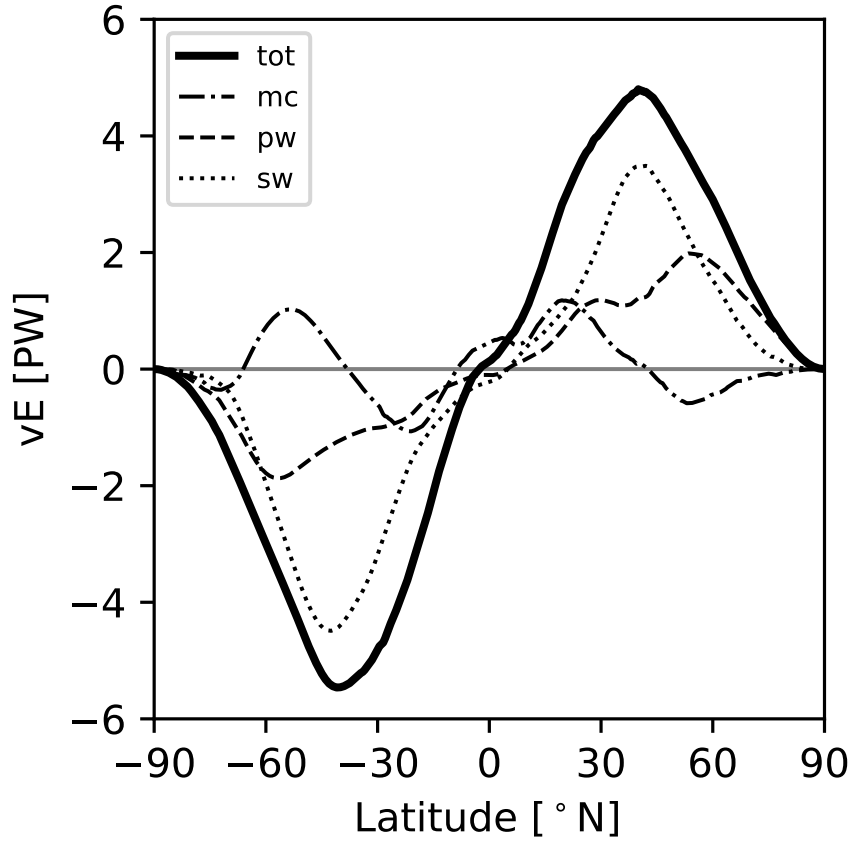


Figure 2.10: Haar-wavelet decomposition of the annual and zonal mean total northward energy transport. The solid line (tot) is the total energy transport, the dash-dotted line (mc) corresponds to the energy transport by meridional circulation, the dashed line (pw) to planetary-scale eddy energy transport, and the dotted line (sw) to the transport by small-scale eddies. The energy transport is computed from ERA-Interim data for the period 1979-2018.

Since the goal is to define a length-scale decomposition the expression in Equation 2.31 may be further simplified by defining

$$vE_j^l = \sum_{k=0}^{2^j} c_{j,k}^{v,l} c_{j,k}^{E,l}$$

such that Equation 2.31 becomes

$$vE(\phi) = \sum_{l=0}^L \left(\overline{vE}_l(\phi) + \sum_{j=0}^{\infty} vE_j^l \right). \quad (2.32)$$

The expression in Equation 2.32 is a general expression for the wavelet-based length-scale decomposition. No specific family of wavelets has been chosen as the basis yet. The constraints on the wavelet family is that the wavelets have to be discrete to form a complete non-redundant basis (Daubechies 1992).

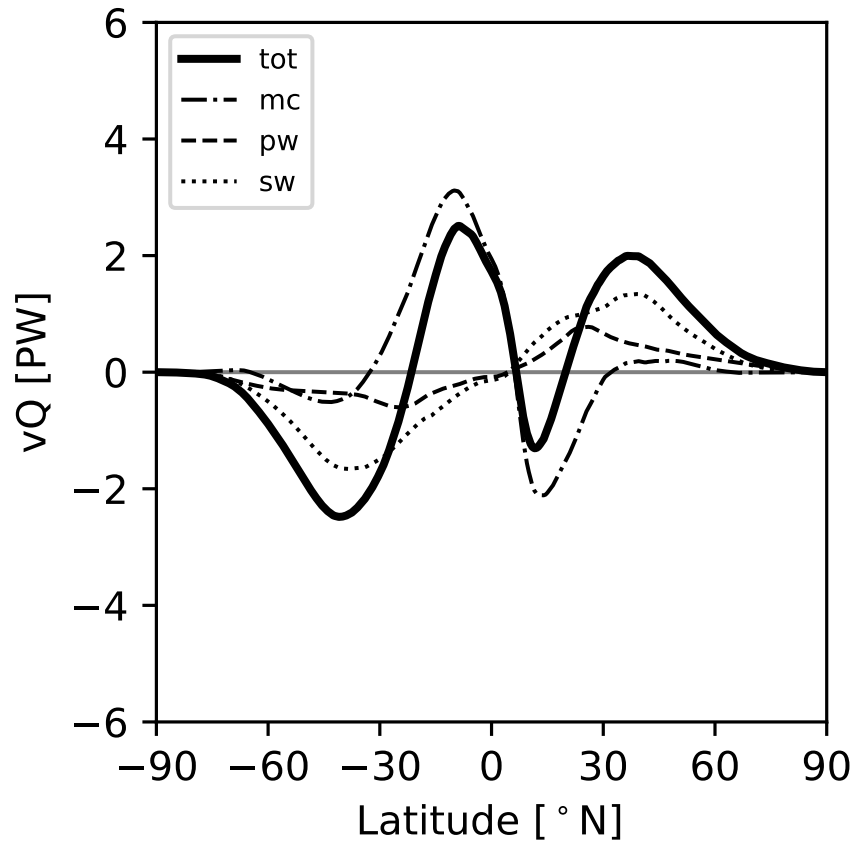


Figure 2.11: As in Figure 2.10 but for latent heat transport.

To compare the wavelet-based length-scale decomposition with the Fourier-based decomposition the Haar family of wavelets was suggested by Heiskanen et al. (2020). The motivation is that the Haar wavelets are simple to convert to length scales, just as is the Fourier basis. The Haar wavelets are essentially step-functions. By performing a wavelet decomposition using the Haar-wavelet decomposition, and splitting between scales $j = 3$ and $j = 4$ which is close to the length scale separation between wavenumbers $n = 3$ and $n = 4$ for the Fourier decomposition, we may decompose the meridional energy transport in a similar way as with the Fourier-based decomposition. The total energy transport (Figure 2.10), latent heat (Figure 2.11), and dry-static energy (Figure 2.12) decompositions are close to the Fourier-based decompositions (figures 2.4-2.6). The comparison of the two length-scale decompositions yields an interesting aspect: the split into planetary-scale and small-scale transport contributions

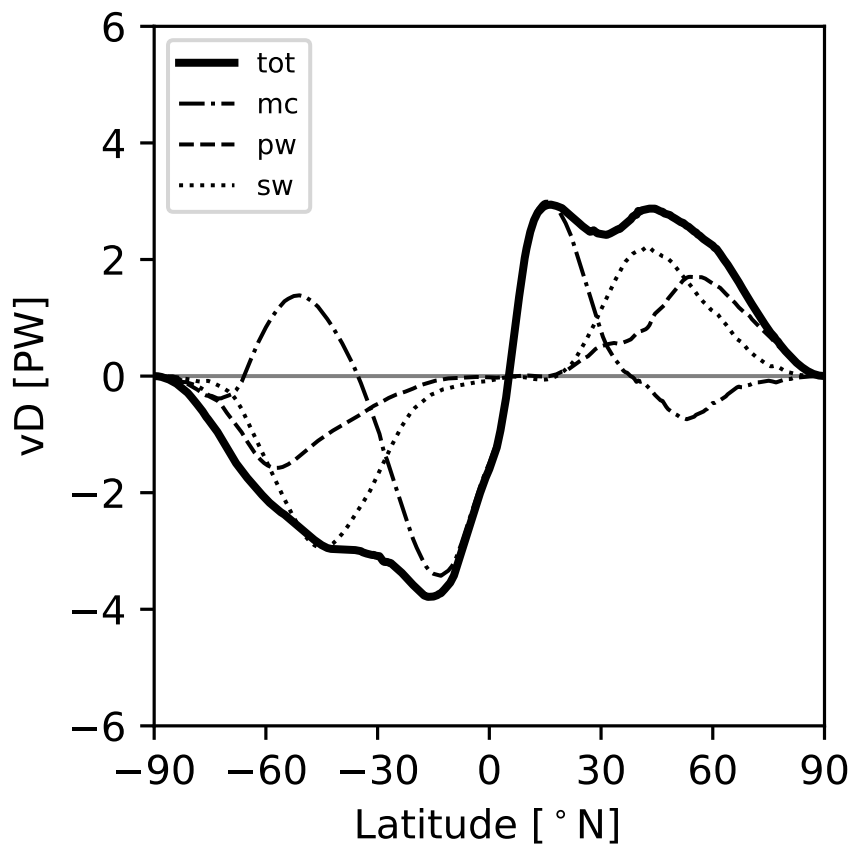


Figure 2.12: As in Figure 2.10 but for dry-static energy transport.

seems to be a property of the atmospheric energy transport, since the split into transport components is similar and achievable by two independent decomposition methods. Hence the transport length-scale decomposition is not only a mathematical construct based on a Fourier decomposition. The wavelets are a completely different kind of basis functions from the non-localized sines and cosines on which the Fourier basis is based. Hence it is remarkable that the decompositions are so similar, which indicates that an energy transport length-scale decomposition using either the Fourier or wavelet-based method is robust. Consequently, the non-localization of the basis functions appears to be only a small problem, and is likely not problematic for the usage of the Fourier-based decomposition (Heiskanen et al. 2020).

The Fourier and wavelet-based decomposition methods have their own advantages and disadvantages. The Fourier-based decomposition yields the possibility to decompose the energy transport directly into contributions of waves by wavenumbers, whereas the direct equivalent of a length-scale decomposition based on wavelets is dependent on the wavelet family. For some wavelets it will

be clear to which length-scale each scaling coefficient corresponds, however for others it will not be as apparent. Hence it is hard to directly translate wavelet scales to wavenumbers. The wavelet decomposition has its advantage in the non-localized basis, which yields a more correct representation of energy transport by small-scale systems than does the Fourier-based decomposition (Heiskanen et al. 2020).

2.4 Machine learning for length-scale decomposition

Machine learning is a rapidly developing field. In general you will find machine learning in many new technological applications and products, from natural language processing in voice assistants to computer vision in self-driving cars. However, applications of machine-learning methods are not limited to technological applications. For instance machine-learning methods have been suggested for weather and climate forecasting (Scher and Messori 2019; Rasp and Thuerey 2021).

Artificial neural networks are one of the main tools in machine learning. These are general function approximators, which are trained to approximate any function mapping from data. Convolutional neural networks are a class of artificial neural networks which rely on sliding convolutional kernels. The convolution stencils are translated across the input images (fields). Convolutional neural networks may have significantly deeper structures than classical artificial neural networks. These structures are typically used to process image data. However, gridded atmospheric data may be interpreted as images, which makes convolutional neural networks attractive structures when designing machine-learning models applied to atmospheric sciences.

Convolutional neural networks have been used and tested for weather forecasting (Scher and Messori 2019; Rasp and Thuerey 2021; Weyn et al. 2021). Classical weather-prediction models are computationally intensive to run. The training procedure of a convolutional neural network is data and time intensive. However, when the model training is finished computing predictions using the trained model is usually immensely efficient. This makes the machine-learning-based approaches good alternatives to the dynamical models.

The Fourier and wavelet-based length-scale decompositions are both computation and storage-wise intensive. The methods require data on a high temporal resolution, typically at least 6-hourly, and throughout the vertical extent of the atmosphere. Hence, the length-scale decompositions are mostly applicable to

reanalysis data or climate-model experiments designed for the computations of the length-scale decompositions. Either the length-scale decomposition has to be computed online during the climate model run, or one has to store the required data on a high temporal resolution (at least 6-hourly) from the experiment. However, the process of computing the length-scale decomposition can be made more effective by applying machine learning. A machine-learning model may be trained to estimate the length-scale decomposition from less data than the exact computations require (Heiskanen et al. 2022b).

2.4.1 Residual networks

Residual networks are a subset of convolutional neural networks which are designed to be even deeper than classical convolutional neural networks (He et al. 2016). The difference between plain convolutional neural networks and residual networks is that the residual networks include a skip-connection (Figure 2.13). The skip-connection routes the original input directly to the output activation function, together with the output from the layer. This diminishes the problem of vanishing gradients in very deep networks, thus making these deep architectures trainable. The residual network structure has been applied with success in earlier studies on weather and climate data (Rasp and Thuerey 2021; Weyn et al. 2021).

2.4.2 Machine-learning-based length-scale decomposition

The Fourier-based energy transport decomposition described in Chapter 2 has been computed from the ERA5 reanalysis data based on several computational efforts. However, it is challenging, and sometimes impossible, to compute the length-scale decomposition from e.g. the models in the CMIP6 archives, due to the lack of data on a high temporal resolution. An alternative approach based on residual networks is suggested in Heiskanen et al. (2022b). By building a function approximator based on the residual network architecture, one may estimate the length-scale decomposed energy transport from considerably less data than typically required. The training process of the network is still a data and computation intensive procedure. However, once the training is complete the decomposition estimate based on the residual network architecture is fairly computationally cheap.

The idea of the machine-learning-based length-scale decomposition is to train a machine learning model ensemble, similar to the approach of Weyn et al. (2021), on the available reanalysis data and use the trained ensemble to estimate the length-scale decomposition from climate model output. By using residual networks with gridded atmospheric data as input, one may estimate the length-

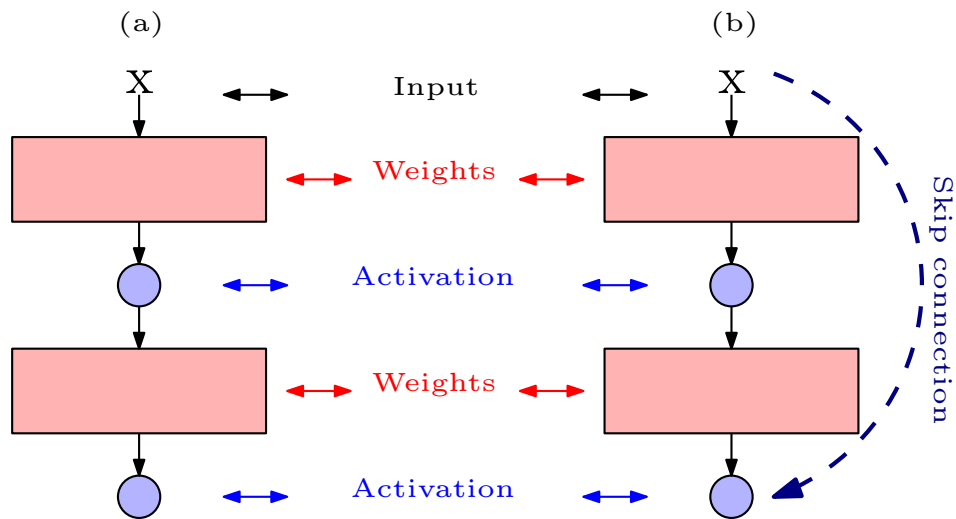


Figure 2.13: Example of a classical and residual convolutional block. In an classical convolutional block (a) the input x passes through two convolutional weight layers and one activation before being passed to the final activation function. A residual block (b) works in the same manner as the classical block (a), but with the addition of a skip-connection, where the original input to the residual block is passed directly to the final activation function, together with the output of the last convolutional layer.

scale decomposed energy transport. The main point of the machine-learning approach is to diminish the data requirements when computing the length-scale decomposition of the meridional energy transport from other datasets. As a proof of concept, a latent heat transport length-scale decomposition with residual networks is trained using the specific humidity and geopotential height fields at 850 hPa, and the Fourier-based length-scale decomposition from ERA5 (Heiskanen et al. 2022b). The machine-learning-based length-scale decomposition approach is extremely efficient when pre-trained. A huge advantage of the machine-learning-based method is that it may be trained on one dataset, e.g. ERA5, and then applied on other datasets, e.g. EC-Earth climate model output (Heiskanen et al. 2022b). The main advantage of the machine-learning-based method is that one may compute the length-scale decomposition from datasets which were out of reach before.

/3

Thesis objectives

The objectives of this thesis are twofold. The first main objective is to test, evaluate and further develop the Fourier-based length-scale decomposition of atmospheric energy transport and propose additional methods. The second objective is to investigate how recent and future climate change has affected the energy transport, and how changes in the energy transport affects the Arctic climate and the mass balance of the Greenland ice-sheet.

3.1 Evaluation and development of length-scale decompositions

The Fourier-based length-scale decomposition proposed by Graversen and Burtu (2016) is an important tool for attribution of meridional energy transport to systems of different length scale. Which systems transport energy into the Arctic is important with regards to the effect on Arctic temperatures, latent heat transport by planetary-scale waves has been shown to be a more important contributor to Arctic temperatures than its small-scale counterpart (Baggett and Lee 2015; Graversen and Burtu 2016). One important part of this thesis is the evaluation of the Fourier-based length-scale decomposition. How well does it represent actual physical systems? What are the fallacies, what are the advantages of this method? These and many other questions were raised at the start of this thesis. The Fourier-based method was developed by Graversen and

Burtu (2016), but never evaluated against other length-scale decompositions. Hence, one of the objectives of this thesis is to evaluate the Fourier-based length-scale decomposition against alternative decompositions.

Changes of the energy transport in a warming climate will be important, as shown in Graversen and Burtu (2016) where an increase in latent heat transport by planetary-scale waves is observed from modelling studies. These model experiments were designed such that enough data were stored to compute the Fourier-based length-scale decomposition. However, this is not typically the case. The computation time and storage requirements of data needed for the Fourier-based length-scale decomposition are such that it is inconvenient or even impossible to compute this decomposition from model archives such as the CMIP6 archives. This limits the amount of usable data sets for investigations of future changes of the energy transport by planetary and small-scale systems. To open up the CMIP6 archives for such studies, a development of an alternative method for the length-scale decomposition is needed.

3.2 Effects of energy transport changes on Arctic climate

The mutual interaction of recent climate change and the energy transport is important to understand. The energy transport changes, e.g. shifts from planetary to small-scale systems, may contribute significantly to the climate change in the Arctic. Additionally, understanding how the atmospheric circulation and the Arctic climate responds to recent climate change may lead to a greater understanding of the processes governing the future climate. Hence assessing how energy transport on various scales affect different regions in the Arctic is one of the main objectives of this thesis. Additionally uncovering the relation between energy transport changes and the melt of the Greenland ice-sheet is important to quantify possible sea-level rise contributions from the Greenland ice-sheet in the future.

/4

Summary of papers

The main contribution of this thesis to the scientific community is the four included papers. These four pieces of work span from method development and testing, to applications of the methods to investigate the Arctic climate and Greenland ice-sheet melt.

4.1 Paper I

Heiskanen, T, Graversen, RG, Rydsaa, JH, Isachsen, PE. Comparing wavelet and Fourier perspectives on the decomposition of meridional energy transport into synoptic and planetary components. *Q J R Meteorol Soc.* 2020; **146**: 2717– 2730. <https://doi.org/10.1002/qj.3813>

The main objective of this paper is to evaluate the performance of the Fourier-based length-scale decomposition. To evaluate the Fourier-based method we need a method to compare it with. Thus, we developed the wavelet-based method, as an alternative approach to a length-scale decomposition of the meridional energy transport. Hence the objective of the paper is twofold:

- Develop and present the wavelet-based length-scale decomposition.
- Evaluate and compare the Fourier and wavelet-based methods for real and synthetic data.

At first we develop the framework for the wavelet based length-scale decomposition, based on the theory of wavelet series expansions (Daubechies 1992). We hypothesized that the Fourier-based length-scale decomposition, denoted FDM in Heiskanen et al. (2020), might have problems resolving the transport by highly localized systems like cyclones correctly. The Fourier and wavelet-based decompositions are tested on both synthetic and reanalysis data. The synthetic data are constructed to challenge the Fourier-based decomposition in terms of highly localized systems, and the wavelet-based method with non-localized systems. Similarly a filtering on ERA-Interim data (Dee et al. 2011) is performed to extract cases with strong and weak localized features, similar to the synthetic data.

From the studies with the synthetic data, it is evident that the Fourier-based method has challenges resolving the localized systems correctly, a large fraction (approximately one third) of the power is attributed to the planetary scales although no waves exist at these scales. However, the wavelet decomposition, denoted WDM in Heiskanen et al. (2020), has some challenges with the planetary-scale waves. If the localization of the initial wavelet is ill-placed with respect to the phase of the planetary-scale waves, the power propagates to smaller length-scales. Considering the filtered ERA-Interim data, we find that the wavelet method is vastly more accurate in the case of circulation patterns dominated by localized cyclones than the Fourier-based equivalent.

In general both the Fourier and wavelet-based length-scale decompositions yield a similar time-averaged energy transport. This is an important finding with regards to the sensibility of performing length-scale decompositions of the meridional energy transport. The fact that the two independent decomposition methods produce similar decompositions provides support for a physically consistent skillful separation between energy transport by large-scale and small-scale waves.

When considering the effects of the decomposed latent heat transport on Arctic temperatures, the Fourier and wavelet-based decompositions have some differences. Figure 8a and 8c of Heiskanen et al. (2020) show the effects of the planetary-scale transport anomaly on temperature based on the Fourier and wavelet methods, respectively. It is evident that the pattern for both methods is similar: the maxima of the regressions occur approximately five days after the transport anomaly, although the strength of the maxima is weaker for the wavelet-based energy transport regressions. However, for the small-scale, or synoptic-scale as denoted in Heiskanen et al. (2020), the overall patterns are different. The small-scale transport as computed by the Fourier decomposition (Figure 8b of Heiskanen et al. (2020)) show mostly the predominant conditions for baroclinic instability (Graversen and Burtu 2016) with cold air north of the transport anomaly and warm air south of the anomaly. The wavelet based small-

scale transport regressions (Figure 8d of Heiskanen et al. (2020)) consistently show the original predominant conditions favorable for baroclinic instability, however they also show a significant warming in the Arctic a couple of days after the transport anomaly which is not apparent based on the Fourier method. Hence the day to day variability of the small-scale waves of the Fourier and wavelet-based methods are not identical.

The main findings of the study is that both the Fourier and wavelet methods appear skillful for providing a length-scale decomposition of meridional energy transport. However one has to be careful when investigating the transport by specific wavenumbers or scales due to the leakage from large-scale circulation to smaller scales for the wavelet method and vice-versa for the Fourier-based method. However, when considering sums of wavenumbers or scales, both methods yield qualitatively similar results. Hence both are solid methods for studies of the length-scale decomposed energy transport.

4.2 Paper II

Rydsaa, JH, Graversen, RG, Heiskanen, TIH, Stoll, PJ. Changes in atmospheric latent energy transport into the Arctic: Planetary versus synoptic scales. *Q J R Meteorol Soc.* 2021; **147**: 2281– 2292. <https://doi.org/10.1002/qj.4022>

This study considers changes in wintertime latent heat transport over the four last decades, and the effects of the changes on Arctic temperatures. The main objective is to identify impacts of latent heat transport length-scale components on Arctic temperatures. Thereafter it is of interest to quantify how these length-scale components have changed during the last decades.

The study is based on the Fourier-based length-scale decomposition proposed in Graversen and Burtu (2016), combined with the extension to a latitude-longitude resolved length-scale decomposition. Additionally the main findings of the work are compared with the wavelet-based length-scale decomposition of Heiskanen et al. (2020). The wavelet-based method produces qualitatively similar results to the Fourier-based method: both for the impacts on Arctic temperatures and trends in the transport components. Here we find that extreme planetary-scale winter transport anomalies are associated with high temperatures all across the Arctic. Extremes are defined as transport exceeding the 90th percentile of the particular season. For small-scale circulation the extremes are mostly associated with the cold Arctic warm extra-tropics pattern, which is favourable for baroclinic instability. This is in agreement with the patterns uncovered in Graversen and Burtu (2016) and Heiskanen et al. (2020), where a small-scale transport anomaly across 70°N is associated with increased

baroclinicity.

We also find that there is a statistically significant increase of wintertime planetary-scale transport extremes, whilst the opposite is observed for the small-scale transport extremes. The decrease in small-scale transport extremes is associated with an observed weakening of wintertime cyclone intensity, found by applying a cyclone tracking algorithm.

The main findings of Rydsaa et al. (2021) is that the extreme planetary-scale latent heat-transport anomalies penetrate deep into the Arctic, and thus lead to a significant warming. There is also an observable positive trend in extreme planetary-scale transport events over the last four decades, which indicates that this circulation change may have contributed to the observed Arctic amplification.

4.3 Paper III

Heiskanen, Tuomas, Rune G. Graversen, Richard Bintanja, and Heiko Goelzer (in review 2022a). “Abrupt increase in Greenland melt enhanced by wind changes.” In: Submitted for review.

The Greenland ice-sheet has undergone unprecedented modern time surface mass loss during the last decades. However, what exactly is driving this mass loss is still uncertain. In Heiskanen et al. (2022a) we try to identify changes of the atmospheric energy transport over the Greenland ice-sheet, and quantify how these changes affect the surface mass balance of the ice-sheet.

By applying the Fourier length-scale decomposition on a latitude-longitude grid we identify convergences of energy transport over the Greenland ice-sheet by planetary small-scale waves. The contributions of energy transport convergence to the surface mass balance are investigated by performing linear regressions. These show that one has to decompose the energy transport into latent heat transport and dry-static energy transport for trends to occur. These trends are strengthened by decomposing the energy-transport convergences into length-scale-based contributions. This indicates that there is no observable trend in the total energy-transport convergence over the Greenland ice-sheet: yet there is a shift between both types of energy and length-scale components, which affects the surface mass balance of the Greenland ice-sheet. It is shown that a Rossby-wave-induced reduction of the westerly flow has led to a decrease in precipitation and an increase in surface warming over the south western parts of the Greenland ice-sheet, thus increasing the Greenland ice-sheet melt in this region.

The study highlights the importance of decomposing the energy transport into latent heat, dry-static energy, and their respective length-scale contributions. Additionally, we show the importance of decorrelating climate variables to uncover their actual effects, e.g. surface energy balance and precipitation, since the correlation between precipitation and surface energy balance leads to unrealistic regressions of the Greenland ice-sheet surface mass balance on the surface energy balance in the interior of the ice-sheet. In general small-scale waves are shown to have a larger effect on the Greenland ice-sheet than their planetary-scale counterparts. This effect is different than for the pan-Arctic studies, which show that planetary-scale transport contributions have the strongest effect on Arctic temperatures (Graversen and Burtu 2016; Heiskanen et al. 2020; Rydsaa et al. 2021). However, this is not inconsistent as we only consider the convergence over the Greenland ice-sheet from a per-grid-point based perspective in this study, which is only a small region of the Arctic where the local effect of small-scale waves can be strong.

In general a convergence of latent heat transport is shown to have a positive impact on the surface mass balance (increase in mass) of the ice-sheet, whereas the opposite is true for convergence of dry-static energy. These effects combined with an observed decrease of latent heat transport convergence and increase in dry-static energy convergence over the ice-sheet lead to a contribution to the observed increase in the surface-mass loss of the Greenland ice-sheet. This effect is especially prominent due to the changes in the Rossby (planetary) wave contributions to the energy-transport convergence.

4.4 Paper IV

Heiskanen, Tuomas, Rune G. Graversen, Richard Bintanja, and Camiel Severijn (in review 2022b). “Length-scale decomposition of energy transport using machine learning techniques.” In: Submitted for review.

The length-scale decompositions proposed in Graversen and Burtu (2016) and Heiskanen et al. (2020) are computational and data intensive. They require information of the atmospheric state throughout the vertical extent of the atmosphere, and on a high (6-hourly or higher) temporal resolution. Hence, they are only applicable to a minor subset of all the available climate datasets. The idea of Heiskanen et al. (2022b) is to present a machine-learning-based estimation technique which extends the subset of dataset from which we may compute the Fourier-based length-scale decomposition of meridional energy transport.

Through application of an ensemble of residual network machine-learning

models we show that one may train a latent heat transport length-scale decomposition approximator based on atmospheric data on 850 hPa and a daily temporal resolution. The training process requires both a previously computed energy transport length-scale decomposition and a significant amount of training time. However, once the network is trained, the network ensemble is significantly more efficient at computing the length-scale decomposition than the exact approach of e.g. Graversen and Burtu (2016). This is the case both with regards to time usage and with regards to data requirements, the required data for the machine-learning estimates are a tiny fraction of the data required for the exact computations.

By testing the machine-learning ensemble trained on ERA5 reanalysis data on climate-model output from the EC-Earth model we show that the trained model is transferable across datasets. The transferability combined with a reduced data requirement opens up for a large portion of the CMIP (Coupled Model Intercomparison Project) archives as potential datasets from which we may compute the length-scale decomposition of energy transport. Thus, the machine-learning-based length-scale decomposition estimator provides a valuable tool for studies of future climate change and intercomparison between climate models. Additionally, the fact that one may train machine-learning models for the computation of energy transport indicates that similar approaches could be used for other climate variables as well.

/5

Main conclusion

Summarized the objectives of this thesis are to

- Evaluate and develop the Fourier-based length-scale decomposition, and alternative length-scale decompositions.
- Investigate the effects of recent climate changes on the energy transport, and how these changes affects the Arctic-climate and the Greenland ice-sheet.

The efforts in Heiskanen et al. (2020) (Paper I) and Heiskanen et al. (2022b) (Paper IV) are mainly focused on the evaluation and development of length-scale decompositions. The Fourier-based length-scale decomposition proposed by (Graversen and Burtu 2016) was not earlier compared with other length-scale decomposition methods. This was the case since there were not any similar methods developed. Hence, we proposed a wavelet-series-based alternative to the Fourier-based method. The wavelet-based method, presented in Heiskanen et al. (2020) (Paper I), is used to make comparisons with the Fourier-based method for artificial data, designed to be challenging for either method, and reanalysis data. From these studies, performed in Heiskanen et al. (2020) (Paper I), it is evident that the Fourier and wavelet-based methods produce qualitatively similar results when comparing the mean meridional energy transport. In general the effect by planetary scale waves on Arctic temperatures is well represented by both methods, suggesting that the planetary scale transports are similar not only in the mean but also in the day-to-day variability.

For the small-scale energy transport, there is some differences between the methods: the wavelet method shows a warming signal in the Arctic which is not present in the Fourier-based transport regressions. However, the main pattern where transport by small-scale waves is preceded by a cold Arctic and warm mid latitudes is present in regressions based on both methods (Heiskanen et al. 2020). The general agreement of the two independent length-scale decomposition methods provide an argument for the capability of actually separating into contributions by different sized dynamical systems of both methods. The fact that the Fourier and wavelet-based methods provide similar decompositions may be interpreted as evidence for the existence of a meaningful length-scale decomposition of meridional energy transport. From this perspective the length-scale decompositions are not only mathematical constructs, they decompose the meridional energy transport into contributions by actual physical systems.

Computing the energy transport length-scale decompositions is a computation and storage intensive process. This limits the applicability of the length-scale decompositions to the reanalysis archives and climate model experiments designed with the length-scale decompositions in mind. One of the main objectives of this thesis was to investigate changes in atmospheric energy transport. Hence it would be extremely useful to be able to compute the length-scale decompositions of energy transport from the CMIP archives. The goal of Heiskanen et al. (2022b) (Paper IV) is to develop a machine learning based energy transport length-scale decomposition estimator, which reduces the computation and data requirements of length-scale decompositions drastically. Based on the results of Heiskanen et al. (2022b) (Paper IV) it is evident that a machine-learning based length-scale-decomposition estimator is a skillful and useful method. The estimator may be trained on reanalysis data, which is still a data and computation intensive process. However, when the machine learning model is trained, it produces estimates of the length-scale-decomposed energy transport from marginal amounts of data and computing time compared to the classical approach. Another important point raised in Heiskanen et al. (2022b) (Paper IV) is the transferability of the trained machine-learning model to other datasets. The machine-learning model trained from ERA5 reanalysis data is capable of estimating the length-scale decomposition from EC-Earth climate model data, this is evident from comparisons with the directly computed length-scale decomposition from EC-Earth data. It is especially encouraging for the applicability of the machine-learning-based model that the model is capable of estimating the energy transport length-scale decomposition not only in the ERA5 period, but also in warmer and colder climates. This indicates that the machine-learning-based energy transport estimator is a strong tool for inter-model comparisons of changing energy transport due to climate change.

Through the contributions of Heiskanen et al. (2020) (Paper I) the validity of the

Fourier-based length-scale decomposition has been emphasized. Although there exist some differences with the wavelet-based decomposition, the Fourier-based length-scale decomposition is a valid approach. Heiskanen et al. (2020) also led to the development of the alternative wavelet based method. For future work the wavelet based method could be further tested by using a different family of wavelets than used in Heiskanen et al. (2020). Additionally, we have only computed the wavelet decomposition from ERA-Interim data. In the future the wavelet decomposition should be computed from the modern ERA5 reanalysis as well. The increased horizontal resolution of ERA5 compared to ERA-Interim would allow us to dive further down the wavelet scales, which would be an interesting test of the robustness of the wavelet method. In addition, it will be convenient for future studies to have both the Fourier and wavelet based length-scale decompositions available. The future pathway following from Heiskanen et al. (2022b) (Paper IV) is evident: the machine learning based energy transport decomposition should be applied to estimate the length-scale decomposition of energy transport from models in the CMIP6 archives.

The climate has changed during the last decades. How this change has affected the contributions of different length-scales to the energy transport is studied in Rydsaa et al. (2021) (Paper II) and Heiskanen et al. (2022b) (Paper III). Additionally, the studies provide new information on how the length-scale components of energy transport affect the Arctic climate in general and the Greenland ice-sheet mass balance. From both studies it is evident that there has been significant changes in the atmospheric circulation during the last few decades. Extreme transport events by planetary-scale waves during winter are shown to have a strong statistically significant effect on Arctic temperatures. Additionally there is an observable and significant positive trend in the extreme transport events. This indicates that the extreme planetary-scale transport events may affect climate change in the Arctic (Rydsaa et al. 2021).

Over the Greenland ice-sheet we observe a significant trend before and after year 2000 in the length-scale components of the convergence of energy. Around the same time period an accelerated mass loss of the Greenland ice-sheet is observed. The trend in the surface-mass balance of the ice-sheet may be linked to the abrupt change in the energy transport components. Hence one of the potential drivers of this non-linear response to climate change of the Greenland ice-sheet mass balance appear to be shifts in the convergence of energy transport from one scale to another (Heiskanen et al. 2022b).

Based on Rydsaa et al. (2021) (Paper II) and Heiskanen et al. (2022b) (Paper III) it is clear that there are observable changes in the length-scale decomposed energy transport during the last decades, which affect the Arctic climate. However, it yet remains a question whether or not the circulation changes are due to climate change or natural variability. An obvious future pathway would be

to investigate this, for example using self organizing maps or empirical orthogonal functions. Additionally it would be of interest to investigate the linkage of circulation changes to dynamical discharge of the Greenland ice-sheet.

The planetary and small-scale energy transport contributions affect the Arctic climate differently. The planetary-scale waves transport energy deep into the Arctic, which has large impacts on Arctic climate. The small-scale transport contributions are especially important over smaller regions of the Arctic, such as the Greenland ice-sheet. In general this thesis provides evidence that there exists a physically meaningful length-scale decomposition of the atmospheric energy transport. The Fourier-based method has been developed further, a wavelet based decomposition has been proposed, and a machine-learning based length-scale decomposition estimator has been designed to overcome the challenges of data availability. We have also studied the effects of the energy transport by the length-scale components on the general Arctic climate, and the Greenland ice-sheet specifically. The studies indicate that the planetary scale transport has an important effect on the Arctic climate in general, and a significant trend in the extreme transport events is observed during the last decades. Whereas for the Greenland ice-sheet a shift between transport components influences the abrupt mass loss observed after year 2000. In an even warmer climate the shifts between energy transport components can have even more severe consequences, the shifts may result in extreme mass loss from Greenland. This is an yet unanswered question, which should be a subject to further studies using climate models and investigating the changes in the energy transport components of these models e.g. by using the techniques presented in this thesis.

Bibliography

- Alley, Richard B., Peter U. Clark, Philippe Huybrechts, and Ian Joughin (2005). "Ice-Sheet and Sea-Level Changes." In: *Science* 310.5747, pp. 456–460. DOI: 10.1126/science.1114613. eprint: <https://www.science.org/doi/pdf/10.1126/science.1114613>. URL: <https://www.science.org/doi/abs/10.1126/science.1114613>.
- Baggett, Cory and Sukyoung Lee (2015). "Arctic Warming Induced by Tropically Forced Tapping of Available Potential Energy and the Role of the Planetary-Scale Waves." In: *Journal of the Atmospheric Sciences* 72.4, pp. 1562–1568. DOI: 10.1175/JAS-D-14-0334.1. URL: <https://journals.ametsoc.org/view/journals/atsc/72/4/jas-d-14-0334.1.xml>.
- Bevis, Michael et al. (2019). "Accelerating changes in ice mass within Greenland, and the ice sheet's sensitivity to atmospheric forcing." In: *Proceedings of the National Academy of Sciences* 116.6, pp. 1934–1939. DOI: 10.1073/pnas.1806562116. eprint: <https://www.pnas.org/doi/pdf/10.1073/pnas.1806562116>. URL: <https://www.pnas.org/doi/abs/10.1073/pnas.1806562116>.
- Callendar, G. S. (1938). "The artificial production of carbon dioxide and its influence on temperature." In: *Quarterly Journal of the Royal Meteorological Society* 64.275, pp. 223–240. DOI: <https://doi.org/10.1002/qj.49706427503>. eprint: <https://rmets.onlinelibrary.wiley.com/doi/pdf/10.1002/qj.49706427503>. URL: <https://rmets.onlinelibrary.wiley.com/doi/abs/10.1002/qj.49706427503>.
- Cohen, Judah et al. (Sept. 2014). "Recent Arctic amplification and extreme mid-latitude weather." In: *Nature Geoscience* 7.9, pp. 627–637. ISSN: 1752-0908. DOI: 10.1038/ngeo2234. URL: <https://doi.org/10.1038/ngeo2234>.
- Daubechies, Ingrid (1992). *Ten lectures on wavelets*. SIAM. URL: <https://doi.org/10.1137/1.9781611970104>.
- Dee, D. P. et al. (2011). "The ERA-Interim reanalysis: configuration and performance of the data assimilation system." In: *Quarterly Journal of the Royal Meteorological Society* 137.656, pp. 553–597. DOI: <https://doi.org/10.1002/qj.828>. eprint: <https://rmets.onlinelibrary.wiley.com/doi/pdf/10.1002/qj.828>. URL: <https://rmets.onlinelibrary.wiley.com/doi/abs/10.1002/qj.828>.

- Dufour, Ambroise, Olga Zolina, and Sergey K. Gulev (2016). “Atmospheric Moisture Transport to the Arctic: Assessment of Reanalyses and Analysis of Transport Components.” In: *Journal of Climate* 29.14, pp. 5061–5081. DOI: 10.1175/JCLI-D-15-0559.1. URL: <https://journals.ametsoc.org/view/journals/clim/29/14/jcli-d-15-0559.1.xml>.
- Fearon, Matthew G., James D. Doyle, David R. Ryglicki, Peter M. Finocchio, and Michael Sprenger (2021). “The Role of Cyclones in Moisture Transport into the Arctic.” In: *Geophysical Research Letters* 48.4. e2020GL090353 2020GL090353, e2020GL090353. DOI: <https://doi.org/10.1029/2020GL090353>. eprint: <https://agupubs.onlinelibrary.wiley.com/doi/pdf/10.1029/2020GL090353>. URL: <https://agupubs.onlinelibrary.wiley.com/doi/abs/10.1029/2020GL090353>.
- Graversen, Rune G. (2006). “Do Changes in the Midlatitude Circulation Have Any Impact on the Arctic Surface Air Temperature Trend?” In: *Journal of Climate* 19.20, pp. 5422–5438. DOI: 10.1175/JCLI3906.1. URL: <https://journals.ametsoc.org/view/journals/clim/19/20/jcli3906.1.xml>.
- Graversen, Rune G. and Mattias Burtu (2016). “Arctic amplification enhanced by latent energy transport of atmospheric planetary waves.” In: *Quarterly Journal of the Royal Meteorological Society* 142.698, pp. 2046–2054. DOI: <https://doi.org/10.1002/qj.2802>. eprint: <https://rmets.onlinelibrary.wiley.com/doi/pdf/10.1002/qj.2802>. URL: <https://rmets.onlinelibrary.wiley.com/doi/abs/10.1002/qj.2802>.
- Graversen, Rune G., Thorsten Mauritsen, Sybren Drijfhout, Michael Tjernström, and Sebastian Mårtensson (June 2011). “Warm winds from the Pacific caused extensive Arctic sea-ice melt in summer 2007.” In: *Climate Dynamics* 36.11, pp. 2103–2112. ISSN: 1432-0894. DOI: 10.1007/s00382-010-0809-z. URL: <https://doi.org/10.1007/s00382-010-0809-z>.
- Graversen, Rune G., Thorsten Mauritsen, Michael Tjernström, Erland Källén, and Gunilla Svensson (2008). “Vertical structure of recent Arctic warming.” In: *Nature* 451.7174, pp. 53–56. ISSN: 1476-4687. DOI: 10.1038/nature06502. URL: <https://doi.org/10.1038/nature06502>.
- Gregory, J. M., S. E. George, and R. S. Smith (2020). “Large and irreversible future decline of the Greenland ice sheet.” In: *The Cryosphere* 14.12, pp. 4299–4322. DOI: 10.5194/tc-14-4299-2020. URL: <https://tc.copernicus.org/articles/14/4299/2020/>.
- Hadley, George (1735). “VI. Concerning the cause of the general trade-winds.” In: *Philosophical Transactions of the Royal Society of London* 39.437, pp. 58–62.
- He, Kaiming, Xiangyu Zhang, Shaoqing Ren, and Jian Sun (June 2016). “Deep Residual Learning for Image Recognition.” In: *Proceedings of the IEEE Conference on Computer Vision and Pattern Recognition (CVPR)*.
- Heiskanen, Tuomas, Rune G. Graversen, Richard Bintanja, and Heiko Goelzer (2022a). “Abrupt increase in Greenland melt enhanced by wind changes.” In: *Submitted for review*.

- Heiskanen, Tuomas, Rune G. Graversen, Richard Bintanja, and Camiel Severijns (2022b). “Length-scale decomposition of energy transport using machine learning techniques.” In: *Submitted for review*.
- Heiskanen, Tuomas, Rune Grand Graversen, Johanne Hope Rydsaa, and Pål Erik Isachsen (2020). “Comparing wavelet and Fourier perspectives on the decomposition of meridional energy transport into synoptic and planetary components.” In: *Quarterly Journal of the Royal Meteorological Society* 146.731, pp. 2717–2730. DOI: <https://doi.org/10.1002/qj.3813>. eprint: <https://rmets.onlinelibrary.wiley.com/doi/pdf/10.1002/qj.3813>. URL: <https://rmets.onlinelibrary.wiley.com/doi/abs/10.1002/qj.3813>.
- Hersbach, Hans et al. (2020). “The ERA5 global reanalysis.” In: *Quarterly Journal of the Royal Meteorological Society* 146.730, pp. 1999–2049. DOI: <https://doi.org/10.1002/qj.3803>. eprint: <https://rmets.onlinelibrary.wiley.com/doi/pdf/10.1002/qj.3803>. URL: <https://rmets.onlinelibrary.wiley.com/doi/abs/10.1002/qj.3803>.
- Hofsteenge, Marte G., Rune G. Graversen, Johanne H. Rydsaa, and Zoé Rey (Jan. 2022). “The impact of atmospheric Rossby waves and cyclones on the Arctic sea ice variability.” In: *Climate Dynamics*. ISSN: 1432-0894. DOI: 10.1007/s00382-022-06145-z. URL: <https://doi.org/10.1007/s00382-022-06145-z>.
- Hwang, Yen-Ting, Dargan M. W. Frierson, and Jennifer E. Kay (2011). “Coupling between Arctic feedbacks and changes in poleward energy transport.” In: *Geophysical Research Letters* 38.17. DOI: <https://doi.org/10.1029/2011GL048546>. eprint: <https://agupubs.onlinelibrary.wiley.com/doi/pdf/10.1029/2011GL048546>. URL: <https://agupubs.onlinelibrary.wiley.com/doi/abs/10.1029/2011GL048546>.
- Jakobson, Erko and Timo Vihma (2010). “Atmospheric moisture budget in the Arctic based on the ERA-40 reanalysis.” In: *International Journal of Climatology* 30.14, pp. 2175–2194. DOI: <https://doi.org/10.1002/joc.2039>. eprint: <https://rmets.onlinelibrary.wiley.com/doi/pdf/10.1002/joc.2039>. URL: <https://rmets.onlinelibrary.wiley.com/doi/abs/10.1002/joc.2039>.
- Kapsch, Marie-Luise, Rune Grand Graversen, and Michael Tjernström (Aug. 2013). “Springtime atmospheric energy transport and the control of Arctic summer sea-ice extent.” In: *Nature Climate Change* 3.8, pp. 744–748. ISSN: 1758-6798. DOI: 10.1038/nclimate1884. URL: <https://doi.org/10.1038/nclimate1884>.
- Khan, Shfaqat A. et al. (Apr. 2014). “Sustained mass loss of the northeast Greenland ice sheet triggered by regional warming.” In: *Nature Climate Change* 4.4, pp. 292–299. ISSN: 1758-6798. DOI: 10.1038/nclimate2161. URL: <https://doi.org/10.1038/nclimate2161>.
- Kim, Hye-Mi and Baek-Min Kim (2017). “Relative Contributions of Atmospheric Energy Transport and Sea Ice Loss to the Recent Warm Arctic Winter.” In: *Journal of Climate* 30.18, pp. 7441–7450. DOI: 10.1175/JCLI-D-17-0157.1.

- URL: <https://journals.ametsoc.org/view/journals/clim/30/18/jcli-d-17-0157.1.xml>.
- Lembo, V., G. Messori, R. Graversen, and V. Lucarini (2019). “Spectral Decomposition and Extremes of Atmospheric Meridional Energy Transport in the Northern Hemisphere Midlatitudes.” In: *Geophysical Research Letters* 46.13, pp. 7602–7613. DOI: <https://doi.org/10.1029/2019GL082105>. eprint: <https://agupubs.onlinelibrary.wiley.com/doi/pdf/10.1029/2019GL082105>. URL: <https://agupubs.onlinelibrary.wiley.com/doi/abs/10.1029/2019GL082105>.
- Messori, G. and A. Czaja (2014). “Some considerations on the spectral features of meridional heat transport by transient eddies.” In: *Quarterly Journal of the Royal Meteorological Society* 140.681, pp. 1377–1386. DOI: <https://doi.org/10.1002/qj.2224>. eprint: <https://rmets.onlinelibrary.wiley.com/doi/pdf/10.1002/qj.2224>. URL: <https://rmets.onlinelibrary.wiley.com/doi/abs/10.1002/qj.2224>.
- Messori, G., Cian Woods, and Rodrigo Caballero (2018). “On the Drivers of Wintertime Temperature Extremes in the High Arctic.” In: *Journal of Climate* 31.4, pp. 1597–1618. DOI: 10.1175/JCLI-D-17-0386.1. URL: <https://journals.ametsoc.org/view/journals/clim/31/4/jcli-d-17-0386.1.xml>.
- Mouginot, Jérémie, Eric Rignot, Anders A. Bjørk, Michiel van den Broeke, Romain Millan, Mathieu Morlighem, Brice Noël, Bernd Scheuchl, and Michael Wood (2019). “Forty-six years of Greenland Ice Sheet mass balance from 1972 to 2018.” In: *Proceedings of the National Academy of Sciences* 116.19, pp. 9239–9244. DOI: 10.1073/pnas.1904242116. eprint: <https://www.pnas.org/doi/pdf/10.1073/pnas.1904242116>. URL: <https://www.pnas.org/doi/abs/10.1073/pnas.1904242116>.
- Muntjewerf, Laura et al. (2020). “Accelerated Greenland Ice Sheet Mass Loss Under High Greenhouse Gas Forcing as Simulated by the Coupled CESM2.1-CISM2.1.” In: *Journal of Advances in Modeling Earth Systems* 12.10. e2019MS002031. DOI: <https://doi.org/10.1029/2019MS002031>. eprint: <https://agupubs.onlinelibrary.wiley.com/doi/pdf/10.1029/2019MS002031>. URL: <https://agupubs.onlinelibrary.wiley.com/doi/abs/10.1029/2019MS002031>.
- Oort, Abraham H. and José P. Peixóto (1983). “Global Angular Momentum and Energy Balance Requirements from Observations.” In: *Theory of Climate*. Ed. by Barry Saltzman. Vol. 25. Advances in Geophysics. Elsevier, pp. 355–490. DOI: [https://doi.org/10.1016/S0065-2687\(08\)60177-6](https://doi.org/10.1016/S0065-2687(08)60177-6). URL: <https://www.sciencedirect.com/science/article/pii/S0065268708601776>.
- Palmén, E. and L. A. Vuorela (1963). “On the mean meridional circulations in the Northern Hemisphere during the winter season.” In: *Quarterly Journal of the Royal Meteorological Society* 89.379, pp. 131–138. DOI: <https://doi.org/10.1002/qj.49708937910>. eprint: <https://rmets.onlinelibrary.wiley.com/doi/pdf/10.1002/qj.49708937910>. URL: <https://rmets.onlinelibrary.wiley.com/doi/abs/10.1002/qj.49708937910>.

- Peixóto, José P. and Abraham H. Oort (1992). *Physics of Climate*. American Inst. of Physics.
- Rasp, Stephan and Nils Thuerey (2021). “Data-Driven Medium-Range Weather Prediction With a Resnet Pretrained on Climate Simulations: A New Model for WeatherBench.” In: *Journal of Advances in Modeling Earth Systems* 13.2. e2020MS002405. DOI: <https://doi.org/10.1029/2020MS002405>. eprint: <https://agupubs.onlinelibrary.wiley.com/doi/pdf/10.1029/2020MS002405>. URL: <https://agupubs.onlinelibrary.wiley.com/doi/abs/10.1029/2020MS002405>.
- Rignot, E., I. Velicogna, M. R. van den Broeke, A. Monaghan, and J. T. M. Lenaerts (2011). “Acceleration of the contribution of the Greenland and Antarctic ice sheets to sea level rise.” In: *Geophysical Research Letters* 38.5. DOI: <https://doi.org/10.1029/2011GL046583>. eprint: <https://agupubs.onlinelibrary.wiley.com/doi/pdf/10.1029/2011GL046583>. URL: <https://agupubs.onlinelibrary.wiley.com/doi/abs/10.1029/2011GL046583>.
- Rosby, Carl-Gustaf (1939). “Relation between variations in the intensity of the zonal circulation of the atmosphere and the displacements of the semi-permanent centers of action.” In: *J. mar. Res.* 2, pp. 38–55.
- Rydsaa, J. H., R. G. Graversen, T. I. H. Heiskanen, and P. J. Stoll (2021). “Changes in atmospheric latent energy transport into the Arctic: Planetary versus synoptic scales.” In: *Quarterly Journal of the Royal Meteorological Society* 147.737, pp. 2281–2292. DOI: <https://doi.org/10.1002/qj.4022>. eprint: <https://rmets.onlinelibrary.wiley.com/doi/pdf/10.1002/qj.4022>. URL: <https://rmets.onlinelibrary.wiley.com/doi/abs/10.1002/qj.4022>.
- Salustri, Giovanna and Peter H. Stone (1983). “A Diagnostic Study of the Forcing of the Ferrel Cell by Eddies, with Latent Heat Effects Included.” In: *Journal of Atmospheric Sciences* 40.5, pp. 1101–1109. DOI: 10.1175/1520-0469(1983)040<1101:ADSOTF>2.0.CO;2. URL: https://journals.ametsoc.org/view/journals/atsc/40/5/1520-0469_1983_040_1101_adsotf_2_0_co_2.xml.
- Scher, S. and G. Messori (2019). “Weather and climate forecasting with neural networks: using general circulation models (GCMs) with different complexity as a study ground.” In: *Geoscientific Model Development* 12.7, pp. 2797–2809. DOI: 10.5194/gmd-12-2797-2019. URL: <https://gmd.copernicus.org/articles/12/2797/2019/>.
- Serreze, Mark C. and Roger G. Barry (2011). “Processes and impacts of Arctic amplification: A research synthesis.” In: *Global and Planetary Change* 77.1, pp. 85–96. ISSN: 0921-8181. DOI: <https://doi.org/10.1016/j.gloplacha.2011.03.004>. URL: <https://www.sciencedirect.com/science/article/pii/S0921818111000397>.
- Shepherd, Andrew et al. (Mar. 2020). “Mass balance of the Greenland Ice Sheet from 1992 to 2018.” In: *Nature* 579.7798, pp. 233–239. ISSN: 1476-4687. DOI: 10.1038/s41586-019-1855-2. URL: <https://doi.org/10.1038/s41586-019-1855-2>.

- Trenberth, Kevin E. (1991). "Climate Diagnostics from Global Analyses: Conservation of Mass in ECMWF Analyses." In: *Journal of Climate* 4.7, pp. 707–722. DOI: 10.1175/1520-0442(1991)004<0707:CDFGAC>2.0.CO;2. URL: https://journals.ametsoc.org/view/journals/clim/4/7/1520-0442_1991_004_0707_cdfgac_2_0_co_2.xml.
- Trenberth, Kevin E. and Julie M. Caron (2001). "Estimates of Meridional Atmosphere and Ocean Heat Transports." In: *Journal of Climate* 14.16, pp. 3433–3443. DOI: 10.1175/1520-0442(2001)014<3433:EOMAAO>2.0.CO;2. URL: https://journals.ametsoc.org/view/journals/clim/14/16/1520-0442_2001_014_3433_eomao_2_0_co_2.xml.
- Vallis, Geoffrey K. (2017). *Atmospheric and Oceanic Fluid Dynamics: Fundamentals and Large-Scale Circulation*. 2nd ed. Cambridge University Press. DOI: 10.1017/9781107588417.
- Weyn, Jonathan A., Dale R. Durran, Rich Caruana, and Nathaniel Cresswell-Clay (2021). "Sub-Seasonal Forecasting With a Large Ensemble of Deep-Learning Weather Prediction Models." In: *Journal of Advances in Modeling Earth Systems* 13.7. e2021MS002502 2021MS002502, e2021MS002502. DOI: <https://doi.org/10.1029/2021MS002502>. eprint: <https://agupubs.onlinelibrary.wiley.com/doi/pdf/10.1029/2021MS002502>. URL: <https://agupubs.onlinelibrary.wiley.com/doi/abs/10.1029/2021MS002502>.
- Zhong, Wenyi and Joanna D. Haigh (2013). "The greenhouse effect and carbon dioxide." In: *Weather* 68.4, pp. 100–105. DOI: <https://doi.org/10.1002/wea.2072>. eprint: <https://rmets.onlinelibrary.wiley.com/doi/pdf/10.1002/wea.2072>. URL: <https://rmets.onlinelibrary.wiley.com/doi/abs/10.1002/wea.2072>.


/6

Paper I

Heiskanen, T, Graversen, RG, Rydsaa, JH, Isachsen, PE. Comparing wavelet and Fourier perspectives on the decomposition of meridional energy transport into synoptic and planetary components. *Q J R Meteorol Soc.* 2020; **146**: 2717– 2730. <https://doi.org/10.1002/qj.3813>

RESEARCH ARTICLE

Comparing wavelet and Fourier perspectives on the decomposition of meridional energy transport into synoptic and planetary components

Tuomas Heiskanen¹  | Rune Grand Graversen^{1,2} | Johanne Hope Rydsaa¹ | Pål Erik Isachsen^{3,4}¹Department of Physics and Technology, University of Tromsø, Tromsø, Norway²Norwegian Meteorological Institute, Tromsø, Norway³Department of Geosciences, University of Oslo, Oslo, Norway⁴Norwegian Meteorological Institute, Oslo, Norway**Correspondence**

T.I.H. Heiskanen, Department of Physics and Technology, University of Tromsø, Postboks 6050, Langnes, 9037 Tromsø, Norway.

Email: tuomas.i.heiskanen@uit.no

Funding information

Research Council of Norway (NFR), Grant/Award Number: 280727

Abstract

The Arctic region shows some of the world's most significant signs of climate change; for instance, a negative trend in summer sea-ice cover of around 15% per decade and Arctic amplified surface-air warming that is three times the global average. The atmospheric energy transport plays an important role in the Arctic climate. Recently a Fourier-based method for studying the atmospheric energy transport contribution by planetary- and synoptic-scale waves has been proposed. Recent studies based on this method show that planetary waves contribute more than synoptic waves to the atmospheric energy transport into the Arctic. However, this Fourier method suffers from being incapable of resolving spatially localized systems such as cyclones. Here an attempt to evaluate this problem is presented by applying the method on synthetic and reanalysis data. In addition, an alternative method based on a wavelet decomposition is proposed and compared with the Fourier-based method. The wavelet method is based on localized basis functions which should be capable of resolving these localized systems. The wavelet method shows an impact of synoptic-scale transport on Arctic temperatures which is not captured by the Fourier method, whilst the planetary-scale effect of both methods appears similar.

KEYWORDS

Arctic amplification, energy transport, latent heat, planetary waves, synoptic waves, wave decomposition, wavelets

1 | INTRODUCTION

The latitudinal variation of incoming solar radiation induces a poleward energy transport in the climate system (Holton and Hakim, 2013). The atmosphere contributes the largest portion of this transport into the Arctic, whilst the ocean contribution is small north of 45°N (Trenberth

and Caron, 2001). At the Arctic boundary (~70°N) the atmospheric contribution is comparable to the incoming solar radiation received by the Arctic (Peixoto and Oort, 1992).

Several atmospheric processes accomplish the meridional energy transport. At low latitudes the Hadley cell is the main contributor, whilst at mid to high latitudes

This is an open access article under the terms of the Creative Commons Attribution License, which permits use, distribution and reproduction in any medium, provided the original work is properly cited.

© 2020 The Authors. *Quarterly Journal of the Royal Meteorological Society* published by John Wiley & Sons Ltd on behalf of the Royal Meteorological Society.

eddies contribute the major part (Vallis, 2017). The eddies include both planetary-scale Rossby waves ($\gtrsim 4,000\text{km}$) and synoptic-scale cyclones ($\lesssim 4,000\text{km}$), both of which induce meridional energy transport. The atmospheric energy transport is traditionally decomposed into latent heat and dry-static components, and into contributions of transient and stationary eddies (Peixoto and Oort, 1992). The decomposition into stationary and transient eddies does not reveal the structure and spatial scale of the eddies transporting energy, since both planetary- and synoptic-scale systems can be either stationary or transient.

Identifying the contributions of planetary- and synoptic-scale systems to the meridional energy transport is important in order to estimate, for example, the interannual variability of the transport and the effects of climate change on the transport, since these types of waves may respond differently to climate change (Graversen and Burtu, 2016; Yoshimori *et al.*, Nov 2017; Naakka *et al.*, 2019). In order to examine the scale dependency of atmospheric energy transport, a Fourier decomposition method (FDM) used to decompose energy transport into contributions from planetary- and synoptic-scale waves was recently proposed by Graversen and Burtu (2016) hereafter referred to as GB16. Based on the FDM it was shown that planetary-scale waves contribute the largest portion of the atmospheric energy transport at the Arctic boundary and hence contribute more to Arctic warming than do synoptic-scale waves. These findings hold for both the latent heat and dry-static energy transports. By applying the FDM to data from the EC-Earth climate model, it was found that changes in the atmospheric circulation patterns may contribute to the Arctic amplification, even if the overall energy transport remains constant or declines. This is because the Arctic cooling due to a projected reduction of total energy transport encountered due to a decline of the dry-static part will be more than compensated for by the warming caused by the increase in planetary latent heat transport (Koenigk *et al.*, 2013; Graversen and Burtu, 2016).

Several recent studies highlight the importance of synoptic-scale systems for the latent heat transport into the Arctic (Boisvert *et al.*, 2016; Woods and Caballero, 2016; Messori *et al.*, 2018). It is intriguing that the synoptic-scale transport appears to show little influence on Arctic temperatures according to the FDM (Graversen and Burtu, 2016), since other studies show that synoptic-scale systems are important for the latent heat transport into the Arctic. Here we speculate that this discrepancy could be partly due to a misrepresentation of synoptic systems by the FDM.

A Fourier decomposition separates fields into a series of sinusoidal waves. However atmospheric fields are of

course seldom composed of pure sinusoidal waves; for example there may exist both sharp zonal gradients and isolated systems simultaneously at one latitude. Such localized systems are not well represented by the FDM, since the Fourier basis is composed of non-localized functions.

This problem can be approached by applying a wavelet decomposition. Wavelets are localized both in space- and length-scale, and are thus capable of representing spatially localized properties of fields. As the basis functions of a wavelet expansion are localized both in length-scale and space, the wavelet method likely represents the spatially localized systems more accurately than the FDM does.

The main objective of this study is to re-evaluate the FDM proposed in GB16 and thus the applicability of Fourier series for zonal wave decomposition of atmospheric fields. The FDM is first evaluated by applying the method on synthetic data where only pure synoptic or pure planetary systems are present. Then the method is applied on filtered fields from the ERA-Interim reanalysis, where the filters are designed to find atmospheric states characterized by isolated cyclones and situations where only planetary waves are present. The same analysis is done using a wavelet decomposition method (WDM) for comparison. Finally both methods are used to assess the effect of latent heat transport on Arctic daily temperatures as in GB16.

The data and methods are presented in Section 2, the results and comparisons in Section 3, and a summary and concluding remarks are provided in Section 4.

2 | DATA AND METHODS

2.1 | Synthetic cyclones

The performance of the FDM and WDM in capturing isolated synoptic-scale systems is first illustrated by applying the methods on synthetic data. The synthetic data are generated to mimic the geopotential height field associated with a longitudinal cross-section through a cyclone centre. The synthetic data are produced with Gaussian functions in the geopotential height field. This approach is applied to ensure that no planetary wave activity is present in the fields used to test the FDM. The winds of the synthetic cyclones are computed assuming geostrophic balance, which is a reasonable assumption in the extratropics (Vallis, 2017).

2.2 | Fourier decomposition method

The FDM approach of GB16 is based on a Fourier series expansion in the zonal direction of the energy field E and

mass transport $v dp/g$, where v is the meridional velocity, p pressure and g is gravitational acceleration. In the present study, only the latent heat transport is considered such that $E = Lq$, where L is the latent heat of evaporation and q is the specific humidity. Here only the final form of the FDM is presented. For the detailed derivation of the FDM the reader is referred to GB16.

A split into wavenumbers by the FDM of the meridional energy transport is given as

$$vE = d \sum_{i=1}^L \left\{ \frac{a_{0,i}^v a_{0,i}^E}{4} + \frac{1}{2} \sum_{n=1}^{\infty} \left(a_{n,i}^v a_{n,i}^E + b_{n,i}^v b_{n,i}^E \right) \right\}, \quad (1)$$

where $d = 2\pi r \cos(\phi)$ is the circumference at latitude ϕ , n the wavenumber, L the number of vertical levels in the dataset, r Earth's radius, ϕ the latitude, and a_n and b_n are the Fourier coefficients of $v dp/g$ and E , with wavenumber n at vertical level i . The meridional energy transport in Equation (1) is further decomposed into contributions from the zonal-mean circulation (the first term) and from planetary- and synoptic-scale waves by splitting the last sum of Equation (1) in terms of wavenumbers. In GB16 the planetary waves correspond to wavenumbers 1–5 and synoptic waves to wavenumbers 6–20. The separation between planetary and synoptic waves between wavenumbers 5 ($\sim 2,700$ km at 70°N) and 6 ($\sim 2,280$ km at 70°N) is somewhat arbitrary. In the present study the wavenumber separation between planetary- and synoptic-scale waves is set to between wavenumbers 3 ($\sim 4,500$ km at 70°N) and 4 ($\sim 3,400$ km at 70°N). This is chosen to better match the actual length-scale of synoptic and planetary systems at 70°N of approximately 4,000 km (Holton and Hakim, 2013).

The data used in the present study are the same as used in GB16 for years 1979–2012, and updated by the same method for years 2013–2017. The present study is based on latent heat transport only, which has been shown to affect the Arctic the most (Graversen and Burtu, 2016). The same evaluation as presented here is also applicable for the dry-static energy transport, and is expected to yield similar results.

2.3 | Wavelet decomposition method

An alternative method to the FDM is a wavelet decomposition method (WDM). The WDM developed here is based on a set of basis functions known as wavelets. The WDM is comparable to the Fourier-based FDM in that both methods decompose the meridional energy (ME) transport into components of different length-scales. However there is a difference in the decompositions: whereas the FDM decomposes the ME transport into contributions based on

wavenumbers, n , the WDM performs a decomposition into spatial scales, j . These are not directly comparable, and the relation between wavenumber n from the FDM and scale j from the WDM is dependent on the chosen wavelet.

A function $\psi(x)$ is a wavelet if it has zero mean (Equation (2)) and unit energy (Equation (3)):

$$\int_0^d \psi(x) dx = 0, \quad (2)$$

$$\int_0^d |\psi(x)|^2 dx = 1, \quad (3)$$

where x is the coordinate along a latitude circle with circuit $d = 2\pi r \cos(\phi)$, as for the FDM. From a wavelet, $\psi(x)$, an orthonormal basis is formed by stretching and translation of the wavelet. Additionally, an amplitude scaling is introduced to ensure unit energy of the wavelets (Daubechies, 1992). The orthonormal basis can be shown to be

$$\psi_{j,k}(x) = 2^{j/2} \psi(2^j x - k), \quad j, k \in \mathbb{Z}, \quad (4)$$

where j is the length-scale and k determines the spatial localization of the wavelet. Both j and k are integers when $x \in [0, 1]$. Hence we choose to normalize x by dividing it by the distance around the latitude circle d . These wavelets constituting this basis are orthonormal with respect to the inner product

$$\begin{aligned} \langle \psi_{j,k}, \psi_{m,n} \rangle &= \int_0^d \psi_{j,k}(x) \psi_{m,n}(x) dx \\ &= \begin{cases} 1, & j, k = m, n, \\ 0, & j, k \neq m, n. \end{cases} \end{aligned} \quad (5)$$

Thus any function, $f(x)$, on the domain $[0, d]$ can be expanded in terms of the orthonormal basis as

$$f(x) = \sum_{j=0}^{\infty} \sum_{k=0}^{2^j} c_{j,k} \psi_{j,k}(x), \quad (6)$$

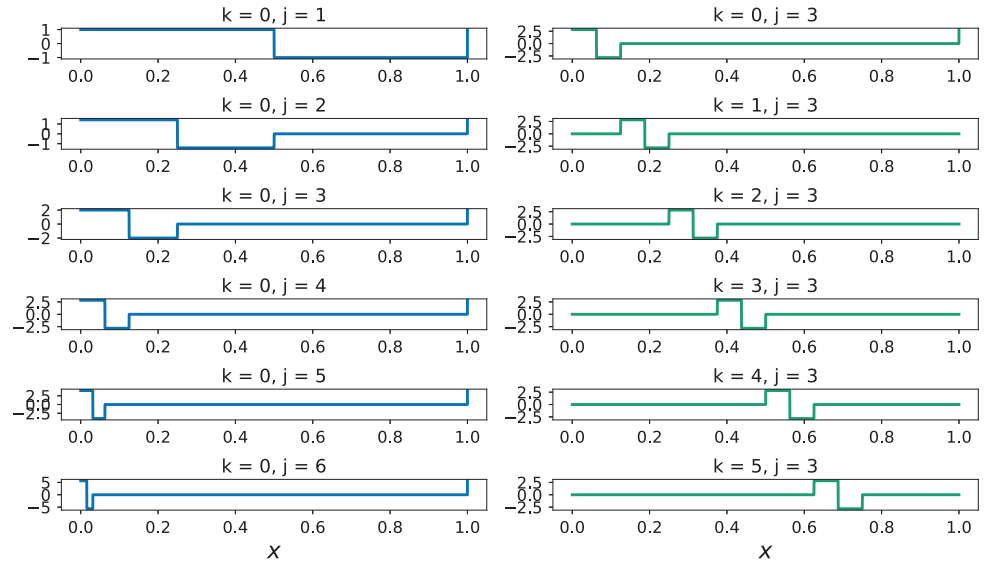
where the coefficients $c_{j,k}$ are given as

$$c_{j,k} = \langle f(x), \psi_{j,k}(x) \rangle = \int_0^d f(x) \psi_{j,k}(x) dx. \quad (7)$$

The imposed orthogonality conditions require basis functions to be discrete wavelets, not continuous wavelets (Daubechies, 1992).

Unlike the Fourier basis, where the basis functions are unique, there exists a variety of wavelet basis functions. Those of the WDM are based on the assumptions in Equations (2) and (3) above, which only require them to be

FIGURE 1 A selection of Haar basis functions. The left column (blue lines) show Haar wavelets with constant k and $j \in [0, 6]$, and the right column (green lines) constant $j = 3$ and $k \in [0, 5]$



wavelets. The WDM used here is based on a Haar wavelet consisting of “box” functions (Figure 1).

Expressing the vdp/g and E fields in terms of a wavelet series yields

$$v \frac{dp}{g} = \sum_{j'=0}^{\infty} \sum_{k'=0}^{2^{j'}} c_{j',k'}^v \psi_{j',k'}(x), \quad c_{j',k'}^v = \int_0^d v \frac{dp}{g} \psi_{j',k'}(x) dx \quad (8)$$

and

$$E = \sum_{j=0}^{\infty} \sum_{k=0}^{2^j} c_{j,k}^E \psi_{j,k}(x), \quad c_{j,k}^E = \int_0^d E \psi_{j,k}(x) dx, \quad (9)$$

respectively. The zonally and vertically integrated meridional energy (ME) transport is given as

$$vE = \int_0^d \int_0^{p_s} Ev \frac{dp}{g} dx. \quad (10)$$

Inserting Equations (8) and (9) into Equation (10) and discretizing the vertical integral yields

$$vE = \sum_{l=0}^L \overline{vE}_l + \int_0^d \sum_{l=0}^L \left(\sum_{j=0}^{\infty} \sum_{k=0}^{2^j} c_{j,k}^{E,l} \psi_{j,k}^l(x) \right) \times \left(\sum_{j'=0}^{\infty} \sum_{k'=0}^{2^{j'}} c_{j',k'}^{v,l} \psi_{j',k'}^l(x) \right) dx, \quad (11)$$

where l denotes the height level in the dataset composed of L levels, and vE_l is the zonal-mean component of the energy transport at level l . When performing the zonal integral of Equation (11), only the terms with $j', k' = j, k$ will remain because of the orthogonality of the wavelets,

whereby

$$vE = \sum_{l=0}^L \left(\overline{vE}_l + \sum_{j=0}^{\infty} \left(\sum_{k=0}^{2^j} c_{j,k}^{E,l} c_{j,k}^{v,l} \right) \right) \quad (12)$$

is obtained. Note that the sum over k is truncated at $k = 2^j$, as higher values of k are localized outside the domain $[0, d]$.

The wavelet split in Equation (12) decomposes the ME transport into components based on length-scale and spatial localization of the systems transporting energy. The j -indices denote the length-scale of the systems, where a larger j denotes a smaller length-scale, and the k -indices denote the localization in the zonal direction. In Equation (12) the sums over l and j are interchangeable, whilst the sum over k is dependent on the sum over j . The expression can thus be rewritten as

$$vE = \overline{vE} + \sum_{j=0}^{\infty} vE_j, \quad (13)$$

where

$$vE_j = \sum_{l=0}^L \sum_{k=0}^{2^j} c_{j,k}^{E,l} c_{j,k}^{v,l}.$$

In the following the decomposition is performed on six scales, in addition to the meridional zonally symmetric flow. The first three scales correspond to length-scales greater than 3,400 km, and the last three to length-scales smaller than that threshold. Hence $j = 3$ and $j = 4$ are chosen as the separation between planetary and synoptic waves, since this is closest to the wavenumber 3–4 separation of the FDM. The Python implementation of the WDM applied for the computations in this project is available

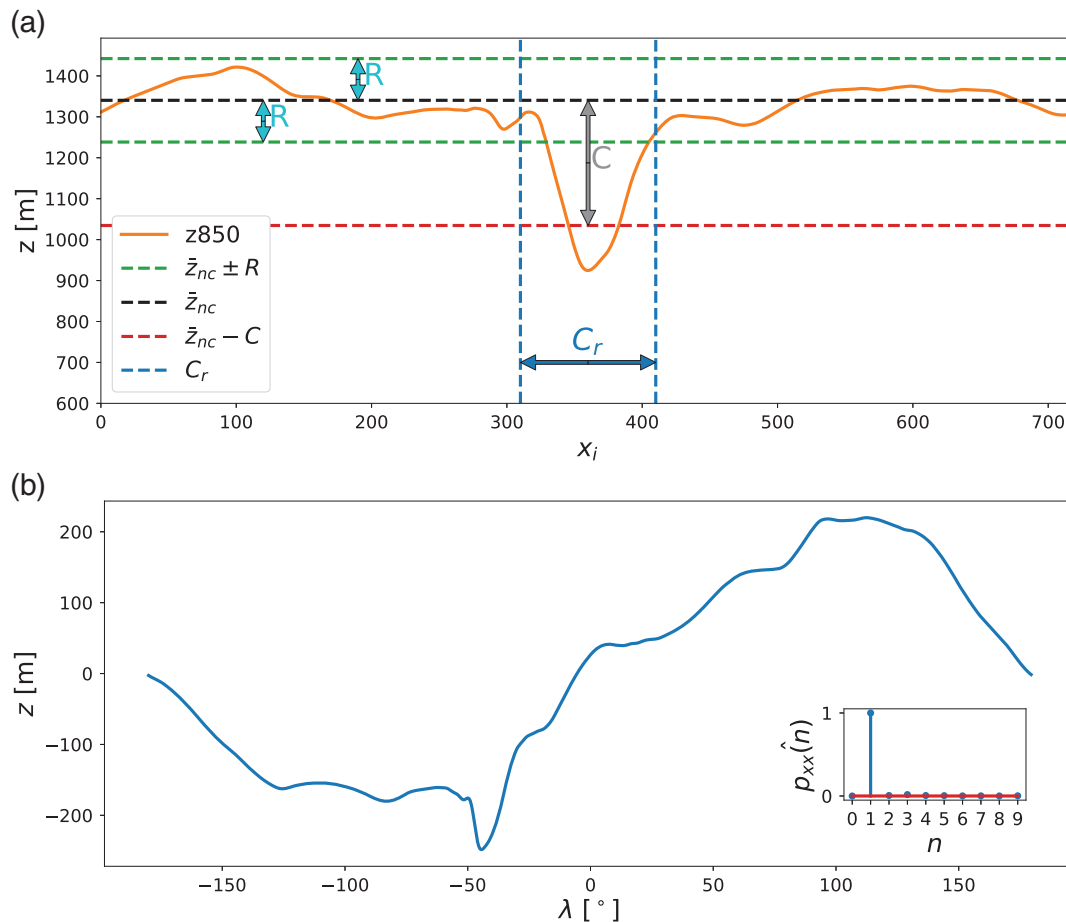


FIGURE 2 (a) is an illustrative example of the conditional filter applied on geopotential height at 850 hPa at 70°N. The shown z_{850} is one of fields marked as a cyclone by the filter, \bar{z}_{nc} is the mean of the z_{850} field outside the cyclone region C_r , R is the maximum z -variation threshold limiting the variability outside C_r , and C is the minimum cyclone threshold defining the depth of the depression in z_{850} relative to \bar{z} . Here x_i denotes the indices of the data points of the rotated field. (b) is an illustrative example of the power spectrum-based filter used for retrieving the planetary waves. One example is shown (blue line) and the associated normalized power spectrum (inset plot) of this field

in a GitHub repository (<https://github.com/tuohei/wdm>; accessed 7 May 2020).

2.4 | Cyclones and planetary waves in ERA-Interim

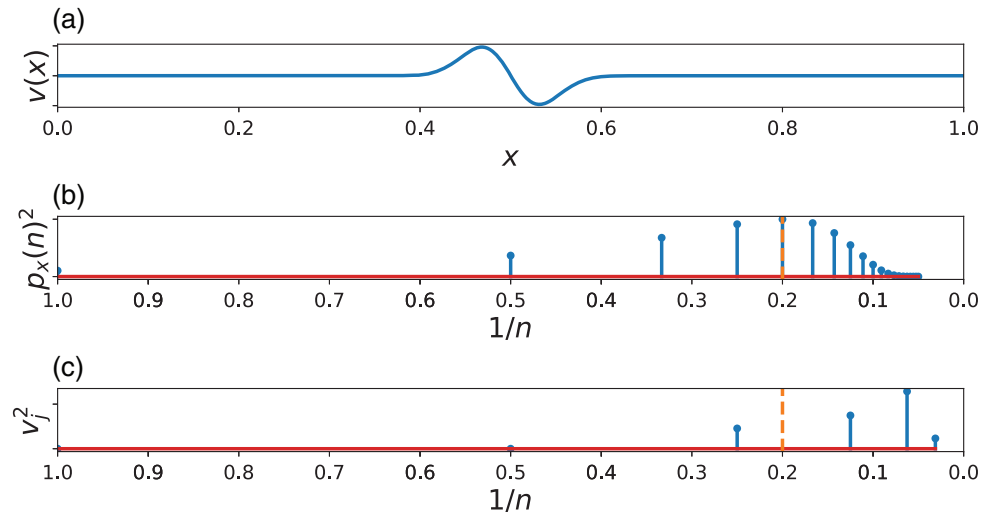
The present study applies the ERA-Interim reanalysis data (Dee *et al.*, 2011) produced by the European Centre for Medium-Range Weather Forecasts (ECMWF). The ERA-Interim reanalysis is used instead of the more state-of-the-art ERA5 reanalysis, since the analysis in GB16 is also based on ERA-Interim, and the main objective of the present study is to re-evaluate the findings based on the FDM presented in that study. Similarly to GB16, the atmospheric fields used in the energy transport are considered with a 0.5° latitude and longitude resolution, and at 60 vertical model levels, and with a 6 hr time resolution.

Time steps where the atmospheric state is characterized by single cyclones but show little influence

by planetary waves are found by applying a conditional filter on the 850 hPa geopotential height field (z_{850}). The longitudinal cross-section of the z_{850} field of a single cyclone is characterized by a sharp negative peak which often resembles a Gaussian function. Constraining the variation of the z_{850} field outside the influence domain of the cyclone hampers the effects of planetary-scale waves, and the field left is thus dominated by the single cyclone.

The conditional filter is constructed by two thresholds: the cyclone threshold, C , providing the strength of the depression in the z_{850} field, and the variation threshold, R , limiting the planetary wave activity. The length-scale, C_r , is defining the cyclone region. This region is the region of influence of the isolated cyclone, defined as a distance of $\sim 1,000$ km at both sides of the maximum depression of the z_{850} field. The length of C_r is chosen such that it is well below the length-scale of synoptic systems at 70°N. The R indicates the upper limit for deviations in the z_{850} field outside C_r from the mean of the outside field (Figure 2).

FIGURE 3 (a) The longitudinal cross-section of the geostrophic winds of the synthetic (Gaussian) cyclone, and (b) is the power spectrum of the geostrophic winds in (a). (c) is the wavelet scale spectrum of the geostrophic winds in (a). The orange dashed line marks the approximate length-scale of the synthetic system. The x -axis of (b) and (c) are set to length-scale $1/n$ for simplicity of comparison, where n is the zonal wavenumber



Planetary waves are found by imposing two conditions on the power spectrum of the $z850$ field. The power of wavenumber $n = 1$ is required to be greater than its climatological mean for the considered period, and additionally the power of the remaining wavenumbers is required to be less than 10% of the power of wave 1. This yields $z850$ fields which are predominantly dominated by a wave 1 pattern. Wave 1 is chosen as the criterion for planetary waves as it is on average found to be the most dominant wave type in the power spectrum of $z850$.

3 | RESULTS

3.1 | Synthetic cyclones

First, as an illustrative example to show the basic concepts, the FDM and WDM are applied on synthetic data. Synthetic data are first generated using a Gaussian function, meant to represent the longitudinal geopotential height of a single cyclone (geostrophic winds in Figure 3a). The Gaussian is a localized function which ensures that no variability on the planetary scale is present in the synthetic data. Essentially the synthetic fields could represent any field, not just the geostrophic winds. These demonstrations are provided to show special cases where both the FDM and WDM may have problems attributing correctly the transport contributions to planetary- and synoptic-scale systems.

The power spectrum of the geostrophic winds associated with the synthetic cyclone (Figure 3b) reveals that approximately one third of the power of the wind field is found in the planetary range (wavenumbers 1–3 placed at the $1/n$ -scale at approximately 0.5, 0.33, and 0.25 respectively). This does not correspond well with the length-scale of the synthetic cyclone, which is a clear

synoptic-scale system; the synthetic cyclone is localized, but has by construction, and what is evident by inspection by eye, a length-scale corresponding to approximately wavenumber 5.

The inaccurate representation by a Fourier decomposition of the synthetic cyclone is due to the localization of the system. This is demonstrated by the application of the WDM on the same geostrophic winds of the synthetic cyclone (Figure 3c). Note that the scale spectrum (Figure 3c) and the power spectrum (Figure 3b) are not directly comparable: the length-scales in the wavelet scale spectrum are decreasing at a higher rate than the length-scales in the power spectrum. Hence the number of j -scales presented is smaller than the number of Fourier wavenumbers n since each j -scale is composed of 2^{j-1} coefficients. For example, j -scale 4 consists of eight coefficients and corresponds to a length-scale of approximately 1,700 km at 70°N , whereas for the WDM wavenumber $n = 4$ corresponds to a length-scale of 3,400 km, given a distance around latitude 70° of $\sim 13,700$ km.

The wavelet decomposition (Figure 3c) appears to resolve these winds in the synthetic case better than does the Fourier decomposition (Figure 3b). With a separation at scales $j = 3$ and $j = 4$ between planetary and synoptic waves, the wavelet method results in a clear majority of power at synoptic scales, whilst the Fourier method yields an even distribution of power between planetary and synoptic scales when a split between wavenumber $n = 3$ and $n = 4$ is applied. Note again that wavenumber $n = 4$, the first wavenumber in the synoptic range, corresponds to a length-scale of approximately 2,200 km at 70°N , which is larger than the first synoptic j -scale ($j = 4$).

The wavelet method is known to be shift variant. The spread of power between the wavelet coefficients will be dependent on the spatial localization of the decomposed

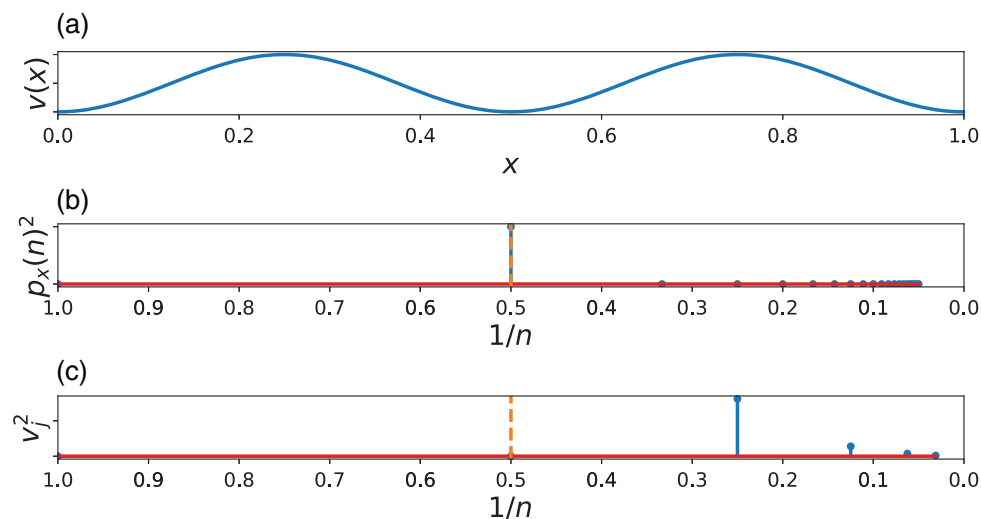


FIGURE 4 (a) Wave 2 structure. (b, c) are as in Figure 3, but for the wave 2 field in (a)

field. However the total power, sum over all coefficients, will remain constant, which is important for the usefulness of the wavelet method for decomposing the energy transport (Daubechies, 1992). This property, combined with the fact that planetary waves are not localized, may limit the accuracy of the wavelet method when it comes to the description of planetary-scale waves. This is demonstrated by applying both methods on a synthetic wave 2 structure.

The wave 2 (Figure 4a) is phase-shifted such that its projection onto the j -scale 2 is zero (Figure 4c), even though it length-scale-wise corresponds to the scale represented by $j = 2$. The sinusoidal wave 2 is a basis function of the Fourier decomposition. This, combined with the fact that the Fourier method is shift invariant, yields that the wave 2 structure will always fall on the corresponding coefficients independent of the spatial localization of the decomposed field, and thus resolves the wave 2 structure perfectly. This example demonstrates that for the WDM, power is shifted to higher scales when the large-scale waves are out of phase with respect to the wavelet basis.

These demonstrations with synthetic data show that the WDM represents localized systems better than the FDM in terms of a separation between planetary- and synoptic-scale contributions. However, since the WDM does not explicitly resolve all wavenumbers, there appears a misrepresentation of systems at the length-scales associated with these unrepresented wavenumbers. In addition, the WDM may have a spread of power from planetary non-localized systems to smaller scales, leading to an misrepresentation of these non-localized system. The spread of power will occur when the phase between the wavelets and the geophysical fields is such that the planetary-scale wavelets are out of phase with the planetary features of the geophysical fields. In comparison, the non-localized waves are well represented with the FDM, since the Fourier basis by nature is non-localized. The synthetic situations

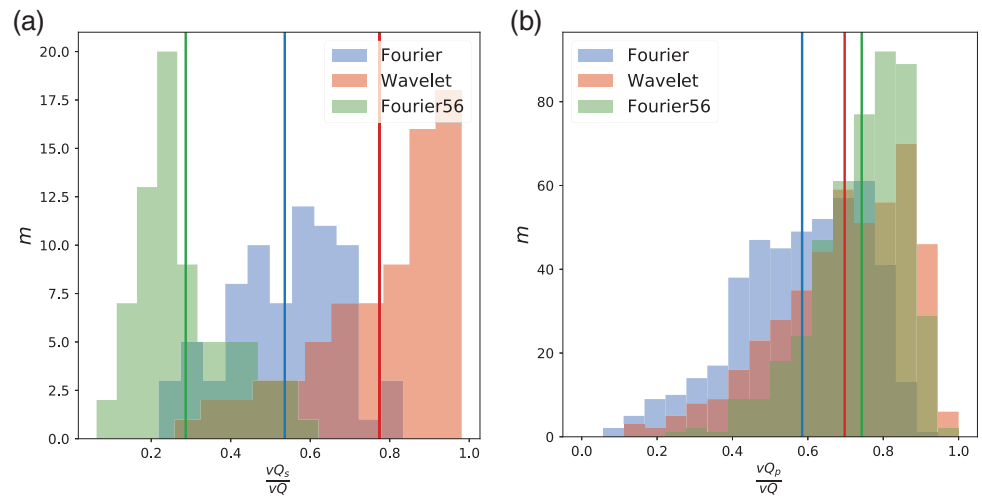
presented here are chosen to show extreme cases for both the FDM and WDM. Hence these are not representative for the general circulation in the atmosphere. These extreme cases are chosen to illustrate the plausible misrepresentations occurring in both methods. However this does not indicate that the WDM generally misrepresents the planetary-scale contribution, and the FDM the contributions by localized synoptic-scale systems.

Both the FDM and WDM are linear methods. This implies that a superpositioned field decomposed by these methods will be the superposition of the decompositions of the individual components of the field. Hence the misrepresentation which might be induced by extreme cases resembling the synthetic ones will be partly hidden in the mean.

3.2 | ERA-Interim cyclones and planetary waves

Should cases similar to the synthetic cyclone exist in the ERA-Interim data, the FDM will have trouble attributing the transport correctly in these situations. A conditional filter, as defined in Section 2.4, is therefore applied on ERA-Interim data in order to reveal such cases in real data. The filter is designed to extract cases with localized cyclones but weak planetary wave activity. Applying the conditional filter on ERA-Interim data, cases which resemble the idealized cyclone are found at 70°N . The filter is applied with several values of thresholds C and R (Figure 2). In total 73 such cases are identified by the conditional filter. For the extracted cases the FDM and WDM are then computed. The fraction of total energy transport in the synoptic range is plotted as a histogram in Figure 5a for the FDM with both a wavenumber separation between $n = 5$ and 6 (FDM56; as in GB16) and $n = 3$

FIGURE 5 Histograms for FDM, FDM56, and WDM based on the cases found by the two filters. (a) synoptic situations identified by the conditional filter; x-axis indicates absolute fraction of transport accomplished by the synoptic scales. (b) planetary situations identified by the power spectrum-based filter; the x-axis is similar to (a) but for planetary scales. Solid vertical lines denote the mean values of the three methods, FDM (blue), FDM56 (yellow) and WDM (red), and m denotes the number of time steps. The darker colours in the histograms indicate overlapping values between the three methods



and 4 (FDM34), as well as for the WDM with a separation at $j = 3$ and 4.

When applied on the filtered cases, the FDM56 attributes on average $\sim 30\%$ of the transport to synoptic waves, whereas both the FDM34 attributes over 50% and the WDM over 75% to these waves (Figure 5a). Hence it is evident that the separation between planetary and synoptic waves between $n = 5$ and $n = 6$ does not capture well the characteristics of the isolated systems at 70°N . The FDM34 resolves the isolated systems better than does FDM56, since some of the planetary coefficients in FDM56 have been transferred to the synoptic range.

As a contrasting method to the filter to extract fields that are composed of isolated cyclones, fields characterized by strong planetary-scale waves are found through conditions imposed on the $z850$ power spectrum. Hence this method can be used to assess the capability of both the FDM and WDM to decompose planetary-scale transport correctly. The fields found by this method have no constraint on their phase, hence the fields may not necessarily correspond to problematic cases for the WDM, as for example that shown in Figure 4. Here the fractions of transport in the planetary range are computed similarly to those computed for the cases found by the conditional filter. In total 461 situations are identified where the wave 1 structure is the dominant pattern of the $z850$ (Figure 5b). For these cases FDM56 attributes on average $\sim 75\%$ of the transport to the planetary scales. The WDM attributes $\sim 70\%$ to the planetary scales, whilst FDM34 attributes $\sim 60\%$ to these scales. For these cases a large fraction of transport in the planetary range is expected; the FDM56 provides on average the largest fraction with the WDM following closely.

The difference between the WDM and FDM34 is not as large as the difference between WDM and FDM56 for the synoptic cases, but it is evident that the WDM yields more average transport in the synoptic range than does the FDM34. For the planetary cases, the FDM56 yields the largest average fraction of the transport in the planetary range, whilst FDM34 yields the smallest fraction. Additionally FDM34 is closer to the WDM when considering both the synoptic and planetary cases found by the two filters. Hence for the rest of the study, the wavenumber separation between $n = 3$ and 4 will be used when referred to the FDM.

For the extreme filtered cases considered in Figure 5, the FDM and WDM attribute differently as regards the planetary and synoptic scales. However, in general the transport appears to be attributed similarly by the two methods. As an example, the time series for one winter season (DJF) is shown in Figure 6, where the planetary and synoptic components of both FDM and WDM are shown. The season shown is the 1985–1986 winter. This winter season has no special statistical characteristics; it is a typical winter season in terms of the attribution of transport to planetary scales, both by the FDM and WDM. Performing a linear regression of the planetary contribution of the FDM on the planetary contribution of the WDM yields $r^2 = 0.82$, which indicates that the two time series are strongly correlated. The mean r^2 for winter seasons is $r^2 = 0.83$. Hence the two methods are describing the planetary- and synoptic-scale transport contributions similarly in the winter season. There is some variation between the transports, which is to be expected since they are based on methods that are fundamentally different, however the large agreement of the transports

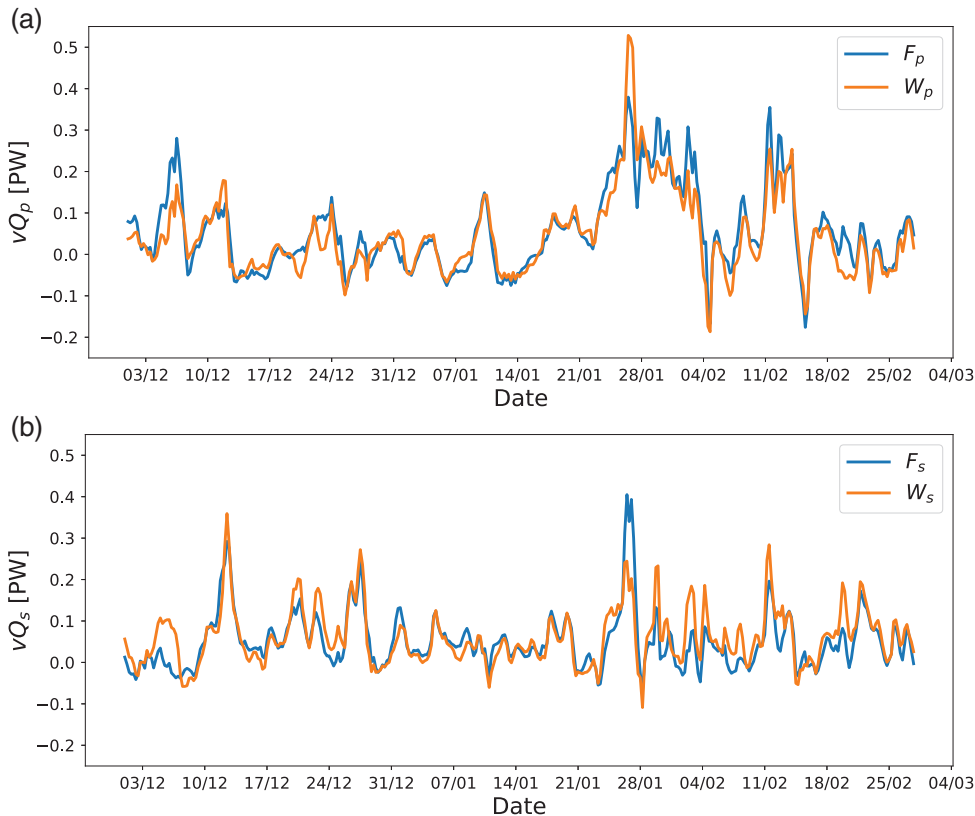


FIGURE 6 Time series of (a) planetary transport vQ_p for both the FDM (F_p) and the WDM (W_p), and (b) synoptic transport vQ_s in the winter season of 1985–1986 across 70°N .

yields a strong argument for the existence of meaningful separation of transport by planetary- and synoptic-scale systems.

Next, FDM and WDM are applied on unfiltered data for latitudes $\phi \geq 60^\circ\text{N}$ and averaged over time (Figure 7). The WDM with a separation of planetary and synoptic waves between scales $j = 3$ and $j = 4$ (Figure 7a) and the FDM with wavenumber separation at $n = 3$ and 4 (Figure 7) yield similar time-averaged latent heat transport for the studied period (1979–2017). The largest differences in the distribution between planetary and synoptic waves are found at low to mid latitudes (not shown), whilst in the high latitudes the differences are small. The fact that the independent methods yield similar time averages strengthens the credibility of both methods to represent the true distribution of transport between planetary- and synoptic-scale waves. But it does not guarantee that the methods actually solve individual time steps equally, as the time average only indicates the mean distribution between transport at planetary and synoptic scales. This difference in individual time steps is evident from the amount of described eddy-transport variance by both methods, presented in Table 1. The WDM yields higher amounts of described eddy-transport variance by both the planetary- and synoptic-scale transport. The transport components of the two methods are also regressed on each other, which shows that the planetary components describe approximately 70% of the variance in the other and the synoptic

component approximately 60% of the variance in the other. This indicates that there are differences between the methods although the time averages are similar. Although similar time-average transports are found using both methods, the difference in described variance may be a contributing factor to the differences in the regressions on Arctic temperatures. Localized systems are still resolved differently, as indicated in Figure 5, which affects the regressions on surface temperatures as shown in the following section.

3.3 | Regressions on Arctic temperatures

The relationship between the latent heat transport across 70°N and the mean 2 m temperature in the Arctic region (above 70°N) can be examined by using a linear regression analysis (e.g., Wu and Straus (2004); Graversen and Burtu (2016)). Here we compute lagged regressions per latitude based on the assumption that a correlation between anomalies in the zonal-mean atmospheric latent heat transport into the Arctic and consecutive anomalies in near-surface temperature inside the Arctic indicates the temperature response to the incoming flux of latent heat. Figure 8 shows the regression of mean 2 m temperature anomalies north of 30°N in response to transport anomalies across 70°N from the FDM and WDM, respectively. The regressions are based on daily data from the time period 1979–2017, at a spatial resolution of 2.5° . Time

FIGURE 7 Meridional latent heat transport and its components as a function of latitude. (a) Wavelet split into meridional circulation ($j = 0$), planetary waves ($j = 1-3$), and synoptic waves ($j = 4-6$). (b) Fourier split into meridional circulation ($n = 0$), planetary waves ($n = 1-3$), and synoptic waves ($n = 4-20$)

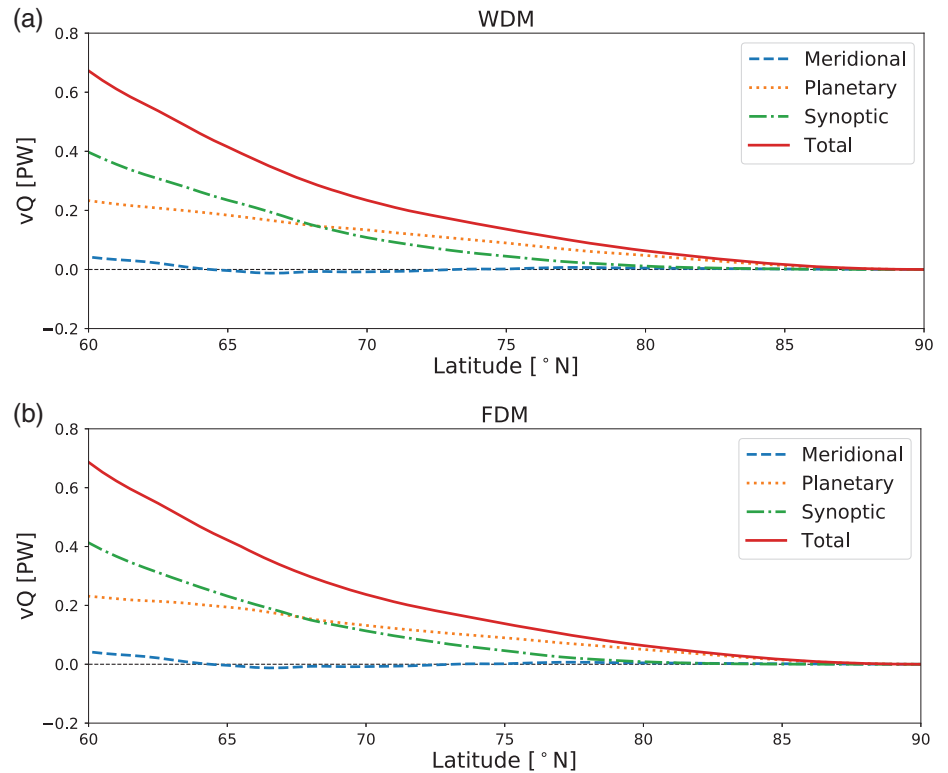


TABLE 1 r^2 coefficients from regressions of both the WDM and FDM total eddy transport on the planetary (p) and synoptic (s) components and from regressions between the components of the two methods

	FDMp	FDMs	Total
WDMp	0.73	0.04	0.64
WDMs	0.07	0.63	0.48
Total	0.60	0.42	1.00

lags up to 20 days are implemented to show the time frame of the temperature response to latent heat transport anomalies. The annual cycle is removed in both the transport data and the temperature data, and a 7-day running mean filter is applied. The black lines indicate areas in the time–latitude plane with statistically significant results based on a Monte-Carlo approach, in which the regression coefficients are compared to 5,000 regressions, where the phases are shifted randomly while keeping the power spectrum time series the same as the original one. A regression is considered statistically significant at the 99% (95%) level if less than 1% (5%) of the synthetic data yield more extreme values in an absolute sense than the original regression coefficient.

The regressions in Figure 8 based on the FDM, are as in GB16 but with a wavenumber separation of planetary and synoptic waves between wavenumbers 3

and 4 relative to the earlier work. This shift of separation yields a larger fraction of time-average transport in the synoptic range at 70°N which is closer to that indicated by the WDM. The FDM suggests that the latent heat transport of planetary waves (Figure 8a) contributes significantly to the subsequent warming of the Arctic. From the regressions on the transport split by the WDM (Figure 8c) it is found that the effect of the planetary wave transport on temperature is weaker than that obtained by the FDM. The weaker effect of planetary transport might be because of an under-representation of planetary waves in the WDM, combined with the fact that localized systems yield an enhanced planetary transport in the FDM.

Regressions of temperature on FDM synoptic transport (Figure 8b) can be interpreted in the light of the predominant enhanced temperature gradient which likely gives rise to increased baroclinic instability and to enhanced activity by synoptic systems: the regressions yield negative temperature anomalies north of 70°N and positive anomalies south of 70°N at the time of the anomaly, indicating an enhanced temperature gradient which sets up favourable conditions for baroclinic instability. The FDM regressions lack signals of warming by synoptic-scale waves in the Arctic. When instead performing the split with the WDM, the synoptic transport pattern shows positive temperature anomalies all over the Arctic for positive time lags (Figure 8d). The signal of an enhanced temperature gradient is present in the WDM regressions as

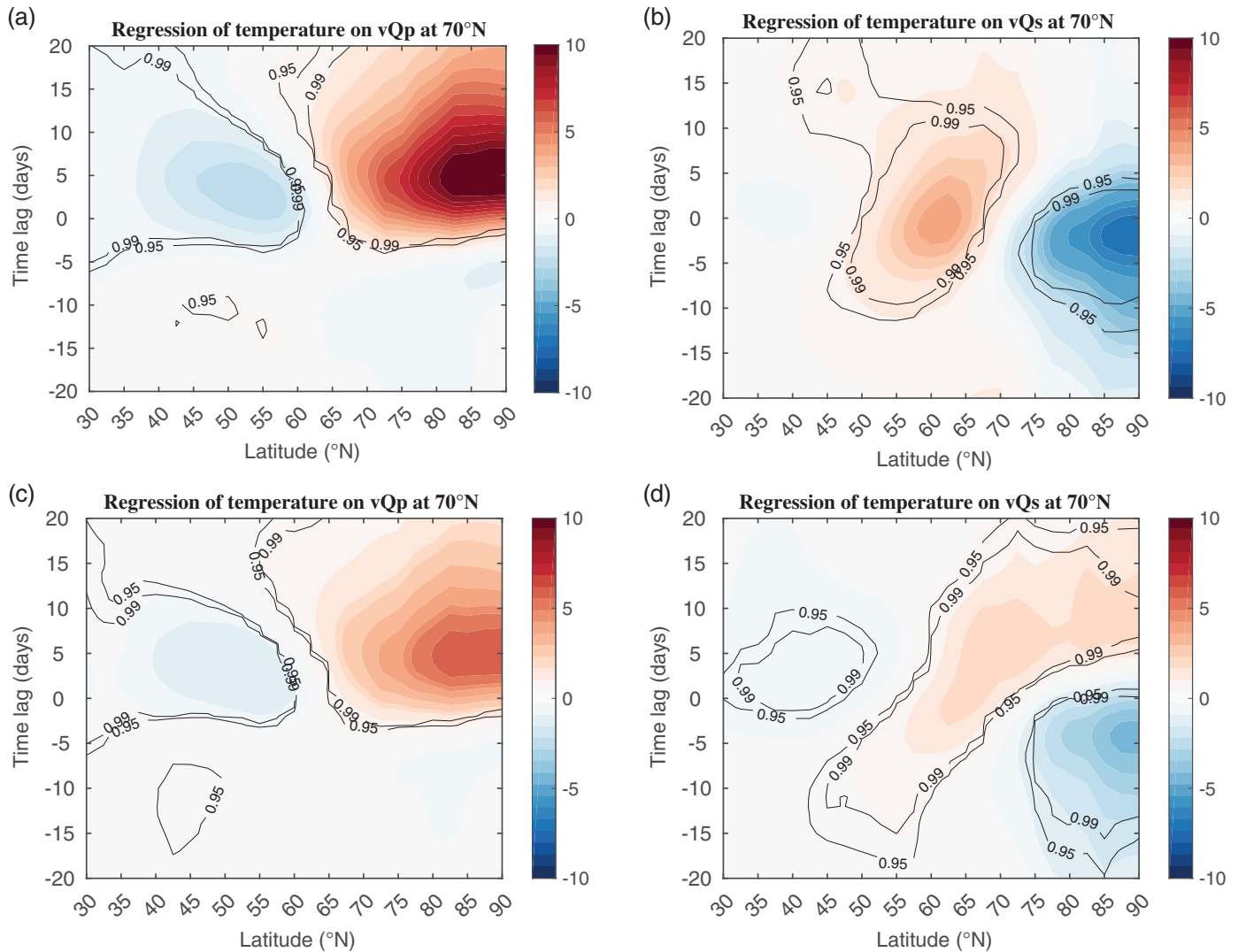


FIGURE 8 Regressions of temperature on (a) the planetary $n = 1 - 3$ and (b) synoptic $n = 4 - 20$ latent heat transport decomposed with the FDM, and (c) planetary $j = 1 - j = 3$ and (d) synoptic $j = 4 - j = 6$ decomposed with the WDM. The colours represent the regressions coefficients in K/PW, and the black contours denote the 0.95 and 0.99 significance levels found by a Monte-Carlo approach

well, but shifted towards negative timelags. This indicates again the presence of increased baroclinic instability associated with large synoptic-scale activity, but the signal of enhanced temperature gradient and Arctic cooling appears before the transport anomaly is at its maximum, in contrast to what is suggested by the FDM. Hence the enhanced baroclinic instability will contribute to the formation of the synoptic-scale systems which transport the energy into the Arctic, to the extent that the Arctic shows positive temperature regressions at positive timelags.

In summary, the difference between the FDM and WDM is especially noticeable for the synoptic part of the transport. From the filtered cases, the FDM is found to represent synoptic systems less accurately than does the WDM, and one effect is shown in the difference between the FDM and WDM synoptic regressions. From

the FDM there is no clear evidence of warming in the Arctic due to the synoptic latent heat transport at 70°N , whereas the regressions on the WDM synoptic transport show an Arctic warming approximately 10 days after the transport anomaly at 70°N . This implies that, according to the WDM, synoptic systems contribute significantly to the subsequent warming of the Arctic, which is in agreement with other previous studies (Woods and Caballero, 2016; Boisvert *et al.*, 2016; Messori *et al.*, 2018).

4 | DISCUSSION AND CONCLUSIONS

Fourier series are widely used to decompose atmospheric fields into processes acting on different scales

(Peixoto and Oort, 1992). The present study highlights the problem of using non-localized basis functions to decompose atmospheric fields. Investigations of synthetic fields and filtered ERA-Interim data demonstrate that the FDM has difficulties attributing the latent heat transport of individual cyclones. This is a fundamental problem of the Fourier series expansion of spiked signals (e.g., Smith 2007). The WDM circumvents this problem by building upon basis functions localized both in space and scale. Hence the split into synoptic and planetary waves in the presence of localized systems appears more appropriate to be represented with the WDM than FDM.

The problem with localized systems is not present in the classical split into stationary and transient eddies (Peixoto and Oort, 1992). However this split is fundamentally different, as it is based on a time-filtering and does not impose any conditions on the spatial scales of the systems; both synoptic- and planetary-scale systems can be stationary or transient. The length-scale split, based on either the FDM or WDM, does not regard the time-scales at which atmospheric systems occur. The length-scale-based methods are used to separate systems based on the dynamical processes leading to their formation. Planetary-scale systems are often forced by orography and land–sea contrasts, whilst the synoptic-scale systems are usually formed by instability processes in the atmosphere. These instabilities are more frequent in some regions (e.g., in the North Atlantic), hence the synoptic-scale systems are not only transient systems but do also have a stationary part. Due to orography and land–sea contrast, the planetary waves too have a stationary component, but these waves are also travelling inducing a transient component. Hence the classical split into stationary and transient eddies is unable to separate between the planetary- and synoptic-scale systems, which is accomplished by the FDM and WDM.

From the inspections of the synthetic cases, the WDM appears as an attractive alternative to the FDM. Also based on isolated systems in ERA-Interim data, it is reasonable to assume that the WDM performs better than the FDM for this type of system. In particular, comparisons of the FDM and WDM for cases found with the conditional filter (Figure 5a) suggests that the WDM outperforms the FDM when it comes to the representation of strongly localized systems.

The WDM resolves synoptic localized systems with little spread of power to planetary scales. However the WDM has some caveats: the wavelet series expansion is shift variant, that is, the wavelet coefficients are dependent on the localization of the atmospheric fields relative to the wavelets. The shift variance affects the planetary waves the most since there are few coefficients representing these

length-scales as compared to the coefficients representing the synoptic scales. In addition, the planetary-scale waves are not localized, which makes the wavelet basis less suitable to attribute these waves. However the WDM has been tested for several different shifts (not shown here), and the results do not change significantly. In addition, the WDM does not attribute the transport into all wavelengths, as demonstrated by the Haar basis (Figure 1). This implies that some of the wavelengths will be represented by different scales than those of these waves. The WDM will also have a dependency on the chosen wavelet, since the values of the wavelet coefficients are dependent on the shape of the wavelet (Daubechies, 1992; Domingues *et al.*, 2005). The WDM in this study is based on the Haar wavelet, which is a box function. It is unlikely to find patterns similar to the Haar wavelet in the atmosphere. However, other discrete wavelet families (Daubechies, 1992) are often not significantly closer to atmospheric states, and are often difficult to relate directly to the length-scales of systems. Thus the Haar wavelet, although its shape is somewhat artificial, serves the purpose of this study as the alternatives are not obviously better.

In GB16 the wavenumber separation between planetary and synoptic waves was chosen between $n = 5$ and $n = 6$. At 70°N wavenumber $n = 5$ represents a length-scale of ~ 2700 km. This is smaller than the threshold of synoptic scales, which is defined as $\sim 4,000$ km (Holton and Hakim, 2013). Shifting the wavenumber separation to between $n = 3$ and $n = 4$ results in more similar decompositions for the FDM and the WDM. The separation of planetary and synoptic waves between $n = 3$ and $n = 4$ is also physically more accurate with respect to the length-scale separation of synoptic and planetary waves at 70°N (Holton and Hakim, 2013). Thus the threshold scale at which the planetary and synoptic scales are separated is not completely arbitrary, and careful consideration of the latitudinal dependence of the length-scale of waves when choosing the threshold is recommended for future studies.

Regressions of temperature on WDM synoptic transport show a positive correlation in the Arctic with a timelag of approximately 10 days (Figure 8d), implying a warming of the Arctic following enhanced energy transport. In contrast, the FDM synoptic transport (Figure 8b) shows no significant warming signal at these latitudes. The fact that the latent heat transport by synoptic systems results in an Arctic warming is consistent with previous studies (Woods *et al.*, 2013; Woods and Caballero, 2016; Messori *et al.*, 2018). It appears as a clear weakness of the FDM that the Arctic warming by synoptic waves is not well captured. Both the warming due to the WDM and FDM planetary latent heat transport show a similar pattern, but the signal is weaker for the WDM case. This weaker signal is


likely due to a misrepresentation of some of the planetary waves by the WDM and the fact that localized systems, likely misrepresented by the FDM, are more correctly represented by the WDM. The truth likely lies somewhere between the results of the WDM and FDM, since the WDM under-represents planetary-scale waves whilst the FDM over-represents these scales. However the importance of latent heat transport by planetary-scale waves is indicated both by the WDM and FDM and the warming effect is stronger than for the synoptic-scale waves, in agreement with GB16.

In summary, spatially localized systems are poorly represented by sine functions, hence a Fourier series approach will misrepresent these systems and should be used with care. The FDM captures the main effect of planetary latent heat transport on Arctic temperatures, but thus fails to accurately represent the synoptic transport effect. The WDM captures the overall effect of planetary as well as the synoptic latent heat transport on Arctic temperatures. A test of the robustness of the WDM results is to perform a similar analysis as in the present study based on a different wavelet basis. The WDM and FDM show a similar effect of planetary latent heat transport on Arctic temperatures. Hence planetary waves play an important role on Arctic temperatures, as uncovered in GB16, and the FDM seems to adequately represent the latent heat transport of planetary-scale systems. In general the FDM will over (under)represent and the WDM under (over)represent planetary (synoptic) transport. Thus it is likely that the true effect of planetary and synoptic transports lies somewhere between the WDM and FDM representations. Hence, when investigating effects of energy transport in the atmosphere at different scales, the FDM and WDM should be used together to form a more complete picture.

ACKNOWLEDGEMENTS

The ERA-Interim data were obtained from the publicly accessible ECMWF data server, and we thank the ERA-Interim development group for providing the data. Data were partially processed at the Stallo supercomputer at the University of Tromsø (UiT) provided by the Norwegian Metacenter for Computational Science (NOTUR), projects NN9345k and NS9063k. The study is funded by The Research Council of Norway (NFR) as part of the project “The role of the atmospheric energy transport in recent Arctic climate change” with project number 280727.

ORCID

Tuomas Heiskanen  <https://orcid.org/0000-0003-0113-0627>

REFERENCES

- Boisvert, L.N., Petty, A.A. and Stroeve, J.C. (2016) The impact of the extreme winter 2015/16 Arctic cyclone on the Barents–Kara Seas. *Monthly Weather Review*, 144(11), 4279–4287. <https://doi.org/10.1175/MWR-D-16-0234.1>
- Daubechies, I. (1992) *Ten Lectures on Wavelets*. Society for Industrial and Applied Mathematics, Philadelphia, PA.
- Dee, D.P., Uppala, S.M., Simmons, A.J., Berrisford, P., Poli, P., Kobayashi, S., Andrae, U., Balmaseda, M.A., Balsamo, G., Bauer, P., Bechtold, P., Beljaars, A.C.M., van de Berg, L., Bidlot, J., Bormann, N., Delsol, C., Dragani, R., Fuentes, M., Geer, A.J., Haimberger, L., Healy, S.B., Hersbach, H., Hólm, E.V., Isaksen, I., Kållberg, P., Köhler, M., Matricardi, M., McNally, A.P., Monge-Sanz, B.M., Morcrette, J.-J., Park, B.-K., Peubey, C., de Rosnay, P., Tavolato, C., Thépaut, J.-N. and Vitart, F. (2011) The ERA-Interim reanalysis: configuration and performance of the data assimilation system. *Quarterly Journal of the Royal Meteorological Society*, 137, 553–597. <https://doi.org/10.1002/qj.828>
- Domingues, M.O., Mendes, O. and da Costa, A.M. (2005) On wavelet techniques in atmospheric sciences. *Advances in Space Research*, 35(5), 831–842. <https://doi.org/10.1016/j.asr.2005.02.097>
- Graversen, R.G. and Burtu, M. (2016) Arctic amplification enhanced by latent energy transport of atmospheric planetary waves. *Quarterly Journal of the Royal Meteorological Society*, 142, 2046–2054. <https://doi.org/10.1002/qj.2802>
- Holton, J.R. and Hakim, G.J. (2013) *An Introduction to Dynamic Meteorology* (5th ed.) Academic Press, Cambridge, MA.
- Koenigk, T., Brodeau, L., Graversen, R.G., Karlsson, J., Svensson, G., Tjernström, M., Willén, U. and Wyser, K. (2013) Arctic climate change in 21st century CMIP5 simulations with EC-Earth. *Climate Dynamics*, 40(11), 2719–2743. <https://doi.org/10.1007/s00382-012-1505-y>
- Messori, G., Woods, C. and Caballero, R. (2018) On the drivers of wintertime temperature extremes in the high Arctic. *Journal of Climate*, 31(4), 1597–1618. <https://doi.org/10.1175/JCLI-D-17-0386.1>
- Naakka, T., Nygård, T., Vihma, T., Sedlar, J. and Graversen, R. (2019) Atmospheric moisture transport between mid-latitudes and the Arctic: Regional, seasonal and vertical distributions. *International Journal of Climatology*, 39(6), 2862–2879. <https://doi.org/10.1002/joc.5988>
- Peixoto, J.P. and Oort, A.H. (1992) *Physics of Climate*. American Institute of Physics, New York, NY.
- Smith, J.O. (2007) *Mathematics of the Discrete Fourier Transform (DFT)* (2nd ed.) Available at: <http://ccrma.stanford.edu/~spi-Sineqddollar>~<spi-Scineqddollar>jos/mdft/>; accessed 7 May 2020.
- Trenberth, K.E. and Caron, J.M. (2001) Estimates of meridional atmosphere and ocean heat transports. *Journal of Climate*, 14(16), 3433–3443. [https://doi.org/10.1175/1520-0442\(2001\)014<3433:EOMAAO>2.0.CO;2](https://doi.org/10.1175/1520-0442(2001)014<3433:EOMAAO>2.0.CO;2)
- Vallis, G.K. (2017) *Atmospheric and Oceanic Fluid Dynamics: Fundamentals and Large-scale Circulation* (2nd ed.) Cambridge University Press, Cambridge, UK.
- Woods, C. and Caballero, R. (2016) The role of moist intrusions in winter Arctic warming and sea ice decline. *Journal of Climate*, 29(12), 4473–4485. <https://doi.org/10.1175/JCLI-D-15-0773.1>
- Woods, C., Caballero, R. and Svensson, G. (2013) Large-scale circulation associated with moisture intrusions into the Arctic during

- winter. *Geophysical Research Letters*, 40(17), 4717–4721. <https://doi.org/10.1002/grl.50912>
- Wu, Q. and Straus, D.M. (2004) AO, COWL, and observed climate trends. *Journal of Climate*, 17(11), 2139–2156. [https://doi.org/10.1175/1520-0442\(2004\)017<2139:ACAOCT>2.0.CO;2](https://doi.org/10.1175/1520-0442(2004)017<2139:ACAOCT>2.0.CO;2)
- Yoshimori, M., Abe-Ouchi, A. and Laine, A. (Nov 2017) The role of atmospheric heat transport and regional feedbacks in the Arctic warming at equilibrium. *Climate Dynamics*, 49(9), 3457–3472. <https://doi.org/10.1007/s00382-017-3523-2>

How to cite this article: Heiskanen T, Graversen RG, Rydsaa JH, Isachsen PE. Comparing wavelet and Fourier perspectives on the decomposition of meridional energy transport into synoptic and planetary components. *Q J R Meteorol Soc.* 2020;146:2717–2730. <https://doi.org/10.1002/qj.3813>






Paper II

Rydsaa, JH, Graversen, RG, Heiskanen, TIH, Stoll, PJ. Changes in atmospheric latent energy transport into the Arctic: Planetary versus synoptic scales. *Q J R Meteorol Soc.* 2021; **147**: 2281– 2292. <https://doi.org/10.1002/qj.4022>

RESEARCH ARTICLE

Changes in atmospheric latent energy transport into the Arctic: Planetary versus synoptic scales

J. H. Rydsaa¹  | R. G. Graversen^{1,2} | T. I. H. Heiskanen¹  | P. J. Stoll¹ 

¹Department of Physics and Technology, UiT The Arctic University of Norway, Tromsø, Norway

²Norwegian Meteorological Institute, Tromsø, Norway

Correspondence

J. H. Rydsaa, Department of Physics and Technology, UiT The Arctic University of Norway, Tromsø 9037, Norway.
Email: johanne.h.rydsaa@uit.no

Funding information

Norges Forskningsråd, Grant/Award Number: 280727; NOTUR Projects, NN3948k, NS9063k

Abstract

Atmospheric meridional energy transport into the Arctic plays an important role in Arctic weather and climate. The transport of latent energy in the form of water vapour strongly influences the Arctic atmosphere. The transport is achieved by circulation mechanisms on various scales and is largely comprised of extreme transport events. Here, we use a Fourier-based method of dividing the latent energy transport into spatial scales and investigate the extent to which extreme events in latent energy transport on planetary and synoptic scales have changed over the past four decades, and how they influence the Arctic winter temperatures. We find that wintertime extreme transport events on planetary scales are associated with warm temperature anomalies across the entire Arctic, while the extreme events on synoptic scales have less impact on the Arctic temperatures. We show that over the past four decades, there has been a significant increase in the wintertime latent energy transport by planetary-scale systems, and a decrease in synoptic-scale transport. This shift may have contributed to the amplified warming observed in the Arctic winter over the past decades.

KEYWORDS

Arctic amplification, Arctic climate, atmospheric circulation, energy transport, Fourier decomposition, planetary waves, wavelet decomposition

1 | INTRODUCTION

The Arctic has warmed at a rate more than twice the global average over the past decades (Serreze and Francis, 2006; Serreze and Barry, 2011), and this Arctic amplification is strongest during the winter season (Bekryaev *et al.*, 2010; Boisvert and Stroeve, 2015). In recent years, the contribution by atmospheric energy transport to Arctic amplification has received increased attention. Energy transport into the Arctic has been shown to greatly alter the Arctic temperatures (Graversen *et al.*, 2008), and plays an important role in the development of Arctic weather and climate

(Graversen and Burtu, 2016; Woods and Caballero, 2016; Ding *et al.*, 2017; Graham *et al.*, 2017a).

The atmospheric transport of energy is commonly divided into dry static energy (DE) and latent energy (LE) parts, where the latter is associated with a flux of water vapour. The transport of LE has been shown to have a stronger effect on near-surface temperatures as compared to that of DE (Koenigk *et al.*, 2013; Graversen and Burtu, 2016). In addition to the LE that is released upon condensation, the water vapour in itself and the condensed cloud water act to increase the local greenhouse effect and thus the long-wave radiation downwards, hereby

This is an open access article under the terms of the Creative Commons Attribution License, which permits use, distribution and reproduction in any medium, provided the original work is properly cited.

© 2021 The Authors. *Quarterly Journal of the Royal Meteorological Society* published by John Wiley & Sons Ltd on behalf of the Royal Meteorological Society.

heating the surface (e.g. Graversen and Burtu, 2016; Gong *et al.*, 2017).

Estimates of future energy transport into the Arctic region indicate that in response to climate change, the transport of LE will increase at the expense of that of DE during the twenty-first century, while the total energy transport remains largely unchanged (Hwang *et al.*, 2011; Bengtsson *et al.*, 2013; Koenigk *et al.*, 2013; Skific and Francis, 2013). It has been suggested that this shift from DE towards LE may result in an increased warming in the Arctic region, due to the larger warming effect of LE transport as compared to that of DE (Graversen and Burtu, 2016; Yoshimori *et al.*, 2017; Graversen and Langen, 2019).

Observations show that the Arctic atmosphere has already become warmer and wetter over the past few decades; observed positive trends of clouds and humidity have been explained by a combination of enhanced evaporation from larger ice-free areas inside the Arctic, and convergence of atmospheric LE transported from lower latitudes (Boisvert and Stroeve, 2015). An examination of seven different reanalysis datasets indicates that the main source of atmospheric moisture (~89–94% at 70°N) in the Arctic is provided by transient eddies, typically entering the Arctic via the storm tracks through the northern North Atlantic, Labrador Sea and subpolar North Pacific (Dufour *et al.*, 2016). In the North Atlantic region, advection of moist, warm air from lower latitudes has contributed to as much as a quarter of the observed winter temperature increase in the past couple of decades (Dahlke and Maturilli, 2017), and nearly half of the winter sea ice decline over the period 1979–2011 (Park *et al.*, 2015). Several studies have focused on the occurrence and effects of intense and extreme weather systems that reach far north into the Arctic (e.g. Woods *et al.*, 2013; Liu and Barnes, 2015). Such extreme events are most often the result of a combination of large-scale circulation mechanisms, and favourable local conditions (Simmonds *et al.*, 2008). To investigate the energy transport caused by the different processes contributing to extreme moisture transport into the Arctic, a decomposition of the total energy transport with respect to spatial scale is useful. Studies have shown that energy transport by systems of different scales impact the Arctic differently, and may respond differently to climate change (Graversen and Burtu, 2016; Yoshimori *et al.*, 2017).

Recently, a method of separating the meridional energy transport using a Fourier decomposition into planetary- and synoptic-scale waves was suggested by Graversen and Burtu (2016). The Fourier method differs from the traditional decomposition method as described by Peixoto and Oort (1992) in that it does not separate the transport into transient and stationary parts. In the Fourier

decomposition, waves on all scales can be transient or stationary, and the separation between waves on planetary and synoptic scales is based on their zonal wavelength. By applying this method to the ERA-Interim reanalysis and investigating the energy transport entering the Arctic at 70°N, Graversen and Burtu (2016) found that the LE part of the meridional energy transported on large, planetary scales causes a stronger and more long-lasting impact on near-surface temperatures in the Arctic region than does energy transported on smaller, synoptic scales. Based on this, they suggest that trends in the different scales of the energy transport can cause changes in the Arctic climate, even while the total transport remains the same.

The Fourier decomposition method was evaluated in Heiskanen *et al.* (2020). They found that as it is based on sinusoidal, non-localized functions, it may not fully capture highly localized transport events, which may in some cases lead to an under-representation of the synoptic-scale transport. In comparison to an alternative decomposition method based on wavelets, Heiskanen *et al.* (2020) found that while the Fourier decomposition method occasionally overestimates the planetary-scale transport at the expense of transport on synoptic scales, the wavelet decomposition method underestimates the planetary-scale transport. They conclude that the true estimate of planetary and synoptic transport is between those provided by the two methods. However, they confirm the dominant role of planetary-scale transport in moisture transport into the Arctic.

In addition to being dependent on scales, the impact of LE transport is also dependent on season. Studies have shown that atmospheric energy transport has a large effect on the Arctic winter atmosphere (e.g. Park *et al.*, 2015). Here, we focus on the winter season LE transport, and investigate how the transports on planetary and synoptic scales impact the Arctic winter temperatures. Investigations have primarily been conducted using the Fourier decomposition method. However, to ensure robust conclusions with respect to the representation of systems on both scales, analyses have also been conducted using the wavelet decomposition method.

Given the increases in atmospheric moisture fluxes observed in the Arctic, we further examine whether there have been changes in the separate scales of the energy transport over the past four decades. A large proportion of the LE transport has been shown to be accounted for by a few extreme events each season (Woods *et al.*, 2013). Here we focus on the extreme events on planetary and synoptic scales separately, and show that there have been significant changes in the wintertime LE transport that may have contributed to the amplified warming observed in the Arctic over the past decades.

2 | METHODS AND DATA

The focus of our investigation is on the latent energy transport, as it has been shown to have the strongest effect on Arctic temperatures. The 70°N latitude defines the Arctic border in this study. As the effects of an LE flux entering the Arctic have been shown to vary between seasons, we focus our investigations on impacts and trends on the wintertime transport.

We use the recently released ERA5 dataset (Hersbach *et al.*, 2020), which is a state-of-the-art reanalysis with a resolution 0.25°. Due to a mass-flux inconsistency in reanalysis data (Trenberth, 1991), a barotropic mass-flux correction has been applied to the wind field at each time step (Graversen, 2006).

We now separate the latent energy into planetary-scale transport and synoptic-scale transport, following the newly developed Fourier-based approach presented by Graversen and Burtu (2016) and evaluated by Heiskanen *et al.* (2020). The meridional latent energy transport can be expressed as

$$\overline{vQ}(\phi) = \oint \int_0^{p_s} vLq \frac{dp}{g} dx, \quad (1)$$

where ϕ is latitude, $\mathbf{v} = (u, v)$ is the zonal and meridional wind components, x is the coordinate in the eastward direction, L the latent heat of condensation, q the specific humidity, p the atmospheric pressure, and g is the gravitational acceleration. By employing a Fourier transformation of the mass flux $v \frac{dp}{g}$ and Lq , one can obtain a decomposition of the latent energy transport planetary- and synoptic-scale waves. For Lq , the transformation yields

$$Lq = \frac{a_0^L}{2} + \sum_{n=1}^{\infty} \left\{ a_n^L \cos\left(\frac{n 2\pi x}{d}\right) + b_n^L \sin\left(\frac{n 2\pi x}{d}\right) \right\}, \quad (2)$$

where

$$a_n^L = \frac{2}{d} \oint Lq \cos\left(\frac{n 2\pi x}{d}\right) dx \quad (3)$$

and

$$b_n^L = \frac{2}{d} \oint Lq \sin\left(\frac{n 2\pi x}{d}\right) dx, \quad (4)$$

where a_n^L and b_n^L are functions of latitude, height and time, and $d = 2\pi R \cos(\phi)$, where R is the Earth's radius. Corresponding coefficients are obtained for $v \frac{dp}{g}$, and by applying the Fourier series of the mass flux and Lq into Equation (1), the meridional transport can be decomposed into wave parts which are defined as representing planetary or synoptic scales. Here, we choose a slightly different definition of planetary and synoptic scales to what was used in Graversen and Burtu (2016): based on the findings in the

evaluating study by Heiskanen *et al.* (2020), we apply a division between planetary and synoptic scales between wave numbers 3 ($\sim 4,500$ km at 70°N) and 4 ($\sim 3,400$ km at 70°N). This yields a planetary-scale transport comprised of waves greater than $\sim 4,000$ km at 70°, which is a good approximation of actual planetary length-scales at 70°N according to Holton and Hakim (2013). The latent transport associated with planetary- and synoptic-scale waves can then be expressed as

$$\overline{vQ_P} = d \sum_{n=1}^3 \left\{ \sum_{k=1}^K \frac{1}{2} (a_n^v a_n^L + b_n^v b_n^L) \right\} \quad (5)$$

and

$$\overline{vQ_S} = d \sum_{n \geq 4} \left\{ \sum_{k=1}^K \frac{1}{2} (a_n^v a_n^L + b_n^v b_n^L) \right\}, \quad (6)$$

respectively, where overbar indicates zonal integrals and index k represents all model hybrid levels from 1 to K . Hence $\overline{vQ_P}$ and $\overline{vQ_S}$ are functions of latitude and time only. By applying the Fourier decomposition on the mass flux, transports as function of longitude in addition to latitude and time can be obtained by

$$\overline{vQ_P} = \sum_{n=1}^3 \left\{ \sum_{k=1}^K \left(a_n^v \cos\left(\frac{n 2\pi x}{d}\right) + b_n^v \sin\left(\frac{n 2\pi x}{d}\right) \right) Lq \right\}, \quad (7)$$

and

$$\overline{vQ_S} = \sum_{n \geq 4} \left\{ \sum_{k=1}^K \left(a_n^v \cos\left(\frac{n 2\pi x}{d}\right) + b_n^v \sin\left(\frac{n 2\pi x}{d}\right) \right) Lq \right\}, \quad (8)$$

respectively. This longitudinal-dependent decomposition could also have been based on a Fourier decomposition of the Lq field rather than the mass flux. However, the mass flux is closely related to the structure of the geopotential height field from which Rossby waves, cyclones and other wave structures are normally revealed. Note that zonal integrals of this longitudinal decomposition of the transport are equal to the components $\overline{vQ_P}$ and $\overline{vQ_S}$ as defined above.

An alternative decomposition method based on wavelets was proposed in Heiskanen *et al.* (2020). The wavelet decomposition method is based on a set of localized functions known as wavelets, and similar to the Fourier method, these functions decompose the energy transport into parts with different length-scales. Hence the method can also be used to decompose the latent energy transport into planetary and synoptic scales. As it is based on localized functions, the method is expected to better represent highly localized synoptic-scale systems. Here, all analyses have also been conducted using the wavelets

method, which is applied to the ERA-Interim dataset. The results from this analysis are largely similar to the Fourier decomposition, and the main conclusions drawn remain the same. More detail of the wavelet decomposition method, along with results of the associated analysis are found in Appendix S1.

The investigations presented here are focused on the latent energy transport and its effects on Arctic temperatures. Several studies have shown that a disproportionately large amount of atmospheric moisture is transported into the Arctic region by the most extreme transport events (e.g. Woods *et al.*, 2013; Liu and Barnes, 2015). Similar to those studies, we focus on the most extreme transport events, which are defined here as days where the zonal-mean transport anomaly at 70°N exceeds the 90th percentile as computed per season on planetary and synoptic scales. Anomalies are deviations from the smoothed seasonal mean, based on the full 40-year time series.

To understand the effect of extreme transport events on Arctic temperatures, we investigate the typical patterns of temperature anomalies arising around the time of such events in the form of composite plots. The composites are computed as averages of the daily-mean locally de-seasonalized temperature anomalies. The temperature anomalies are de-trended locally using a 4th-degree polynomial fit. Statistically significant areas are identified by a Monte Carlo approach; the selection of days is compared to 5,000 random selections of days from the same season, and only the areas that have a larger absolute value of anomalies in less than 5% of the cases are considered significant at the 95% level. For days identified as extreme, the location of the peak of LE transport along 70°N is identified from the longitude-dependent decomposition, which aids in linking the trends identified here to large-scale circulation changes.

3 | RESULTS

3.1 | Locations of extreme events

Figure 1 shows the longitudinal distribution of winter season LE transport across 70°N on days identified as extreme. Each curve shows the daily mean latent energy transport anomaly as a function of longitude on days that exceed the seasonal 90th percentile on the planetary scale (upper panel) and the synoptic scale (lower panel). Areas with highly (weakly) saturated colour indicate several (few) superimposed curves, that is, common (uncommon) longitudes of transport on extreme days. Most curves are dominated by one distinct peak, which indicates one main transport event on the extreme day that

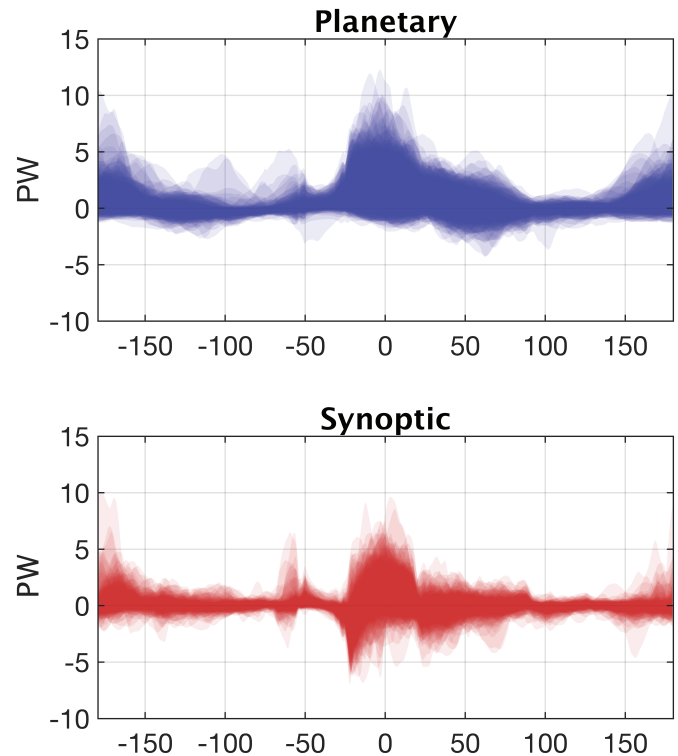


FIGURE 1 Extreme latent transport (PW) as a function of longitude (°E) along 70°N for all winter season extreme cases as curves with transparent shading superimposed on top of each other. Each curve represents the latent energy transport anomalies across 70°N for a day above the 90th percentile level. More saturated colour indicates overlapping curves, i.e. areas with high frequency of transport on extreme days; planetary scale is shown in the upper panel, and synoptic scale in the lower panel

curve represents. In most cases the peaks, that is, the locations of the extreme events, are concentrated above the relatively warm open ocean areas, namely the Atlantic sector and the Bering Strait, on both scales. A similar pattern of extreme transport events being concentrated over the warm ocean basins in winter has also been observed in other studies (Woods *et al.*, 2013; Liu and Barnes, 2015; Woods and Caballero, 2016).

On the synoptic scale the latent energy transport is associated with, for example, cyclones entering the Arctic and bringing water vapour with them. Particularly in the Atlantic sector, the northward component of the cyclonic circulation is clearly shown as positive peaks at the eastern side of the cyclones, and the southward component seen as a sharp negative peak on the western side of it (Figure 1, lower panel).

In general, the planetary-scale events bring more latent energy to the Arctic. Overall, the wintertime latent energy transport on the synoptic and planetary scales accounts for 32% and 68% of the total wintertime transport, respectively (based on the sum of daily means). The extreme winter days on the planetary scale account for 33% of the total

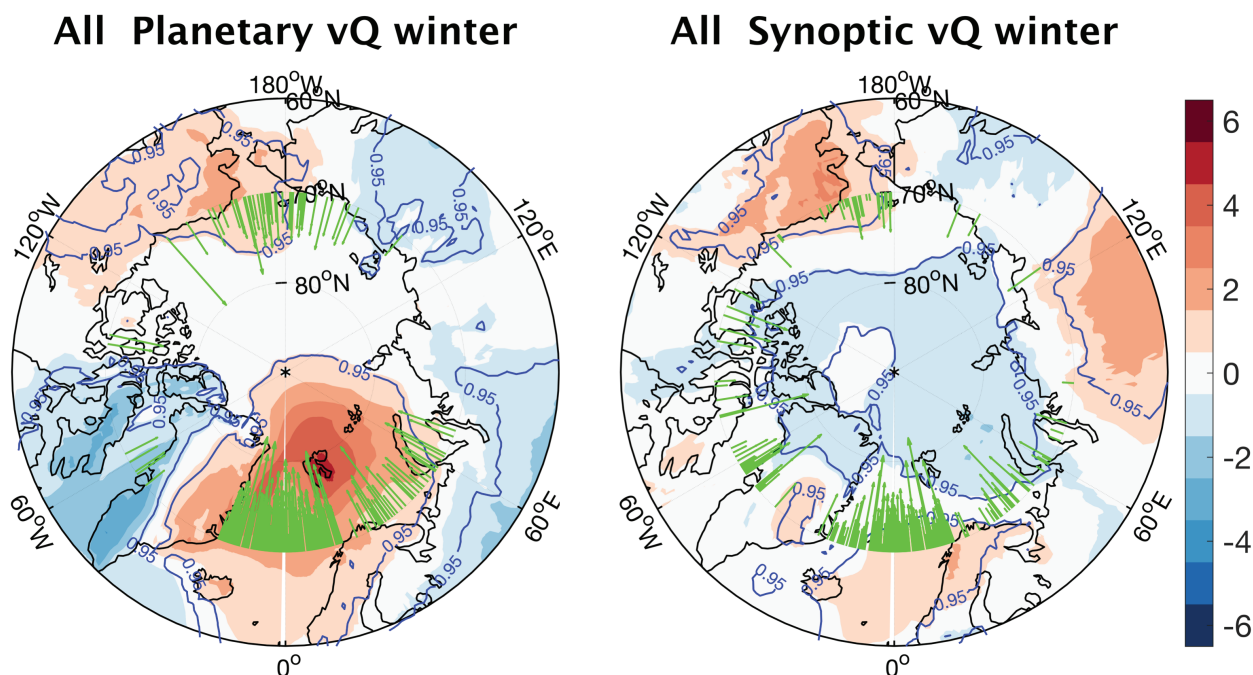


FIGURE 2 Mean temperature anomalies ($^{\circ}\text{C}$) related to extreme (>90th percentile) latent energy transport anomalies across 70°N . Green arrows along 70°N indicate the point of maximum transport anomaly for each extreme day. The length of the arrows is scaled to one-degree latitude per PW latent energy, and as such does not reflect the extent to which the transport reaches into the Arctic area. Blue lines enclose areas with statistically significant results according to a Monte Carlo test for significance with 5,000 simulations

planetary transport, and about 22% of the total transport. The synoptic-scale extreme days account for about 34% of the total synoptic transport, and 11% of the total transport.

The temperature pattern associated with extreme transport events is shown as temperature anomalies as averaged over extreme transport days on both length-scales (Figure 2). An arrow marking the location of the peak transport anomaly each day is added along the 70°N latitude. Note that the arrows are scaled according to the strength of the event and are not indicative of how far into the Arctic the transport reaches.

There are significant temperature anomalies inside the Arctic associated with extreme events on both synoptic and planetary scales; however, they are of opposite signs: planetary-scale events are associated with warm anomalies inside the Arctic (Figure 2, left panel), while synoptic-scale events are associated with cold anomalies (Figure 2, right panel). During planetary-scale extreme events, the warm temperature anomalies are concentrated around the areas where the peak transport most often occurs, and the largest warm anomaly is centred over the Svalbard region and stretches as far as the North Pole. The average temperature anomaly for the Arctic as a whole during planetary events is $+0.63\text{ K}$. The Atlantic sector (defined here as -40° to $+60^{\circ}\text{E}$), contributes with 77% of the wintertime planetary events, and therefore dominates the mean temperature pattern. Accounting only for the

events and temperature anomalies occurring within these longitudes, the average temperature increase in the sector is 2.67 K .

On days with strong synoptic transport (Figure 2, right panel), the Arctic region is on average dominated by anomalously cold temperatures (-0.37 K), while warm areas are found just outside and to the south of the extreme transport events. The temperature patterns seem to be closely associated with an atmospheric situation favourable for synoptic-scale events; a sharp temperature gradient across 70°N with cold air to the north and warm anomalies to the south can act to increase baroclinicity necessary for creating an extreme synoptic event. This temperature profile is similar to findings in Graversen and Burtu (2016), who by performing a regression analysis of near-surface temperatures on synoptic-scale energy transport, found a similar pattern in the zonal average.

The large differences in the mean temperature patterns associated with the two scales reflect the different circulation types responsible for the energy transport on each scale. The fact that the impact of these circulation types are so clearly revealed in the temperature composites suggests that the decomposition of the energy transport into different scales is important, and that the division between planetary and synoptic scales as defined here is capable of capturing typical transport situations on each scale. Also, the pattern for mean temperature anomalies shows very

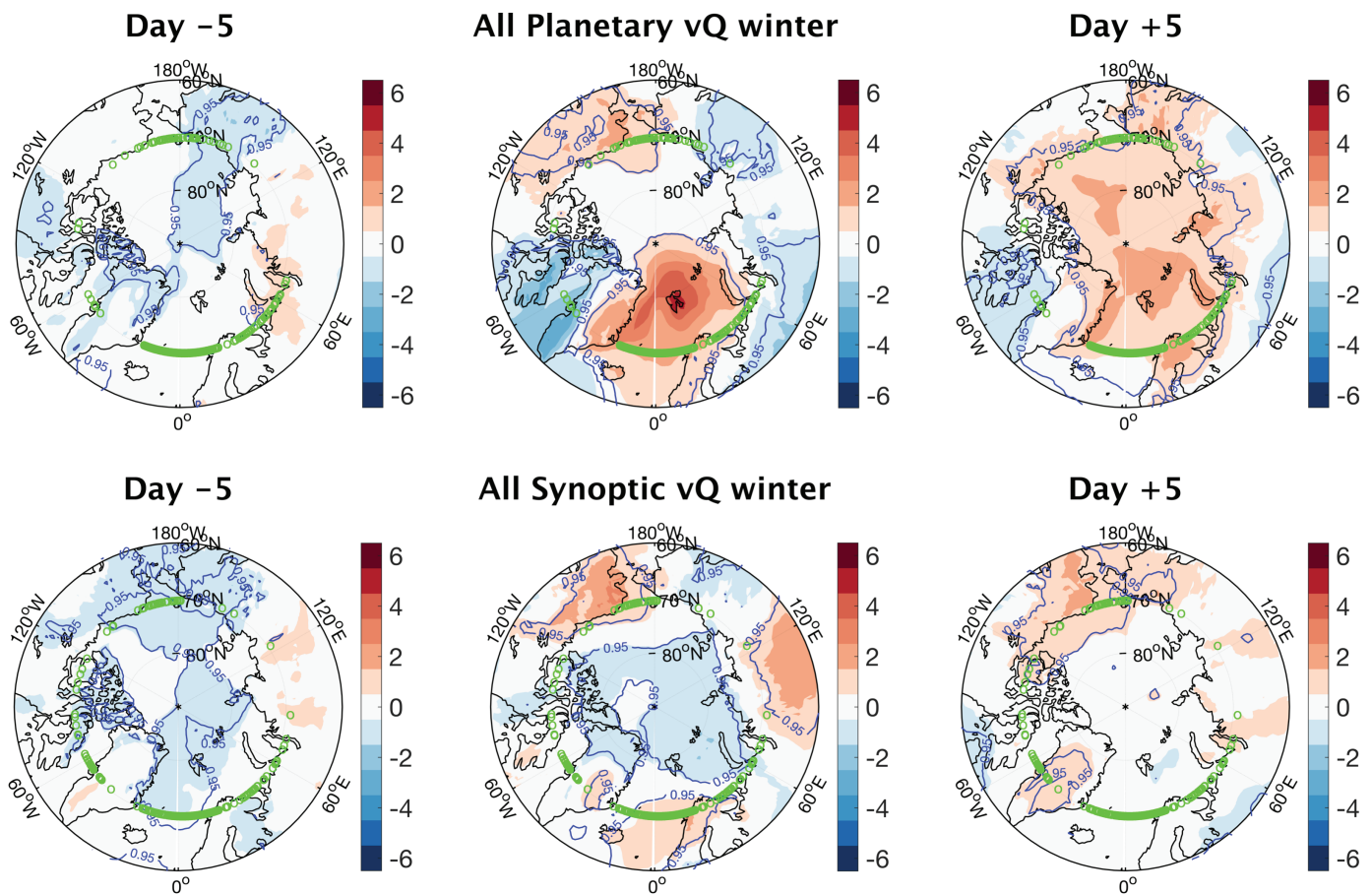


FIGURE 3 Temperature anomalies as averaged over days of extreme transport entering the Arctic (maximum transport locations shown as green dots). Temperature anomalies 5 days ahead of events (left column) on the day of extreme transport events (middle column) and 5 days after events (right column) for planetary-scale events (upper row) and synoptic-scale events (lower row). Blue lines surround areas with statistically significant anomalies

similar results when compared to composites based on the wavelet decomposition method, both with regard to strength and geographical distribution of the temperature anomalies (Figure S1, supplementary material).

The time-development in surface temperature anomalies in response to the extreme events on each wave scale is seen in Figure 3, which shows the mean temperature anomalies before, during and after extreme transport events. On the planetary scale (Figure 3, top row), the warm anomaly appears on the day with extreme transport, and 5 days later it has spread across most of the Arctic basin (Figure 3, top-right panel). Although the largest temperature anomalies are seen locally in the Svalbard region on the day of the extreme transport event, the Arctic area as a whole is most influenced a few days after the planetary-scale event.

On the synoptic scale, anomalously cold temperatures inside the Arctic region before the events and during the events dominate the mean temperature anomaly development (Figure 3, lower row). Five days after the events, the

cold anomalies inside the Arctic region have been broken up, and the anomalous temperature gradient across 70°N is dissolved (Figure 3, lower-right panel), leaving no significant anomalies inside the Arctic region.

It may be inferred from this analysis that the planetary-scale events are closely associated with unusually warm temperatures in the Arctic region, while the synoptic-scale extreme events mainly contribute by dissolving preconditioning temperature gradients with Arctic cold anomalies.

The composite plots show the temperature anomalies associated with extreme events as averaged over several different extreme days; however, they do not show the potential for temperature changes that actually occur during each event, which can be much more dramatic. To illustrate the type of situation that these extreme events represent, we have included a case from the N-ICE2015 measurement campaign (Cohen *et al.*, 2017; Graham *et al.*, 2017b) that took place north of Spitsbergen in January 2015.

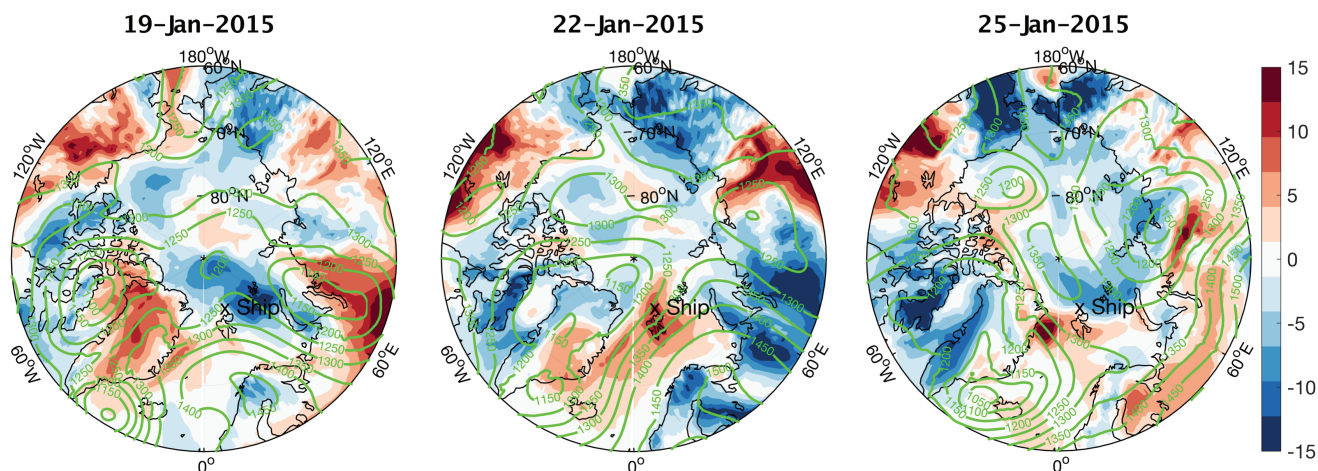


FIGURE 4 Temperature anomalies ($^{\circ}\text{C}$) on 22 January 2015 (middle) and 3 days before (left) and after (right). Green contour lines show the geopotential height at 850 hPa. The ship's approximate position on 22 January is marked north of Svalbard

3.2 | Case: Spitsbergen, 22 January 2015

The Norwegian Young Sea Ice expedition (N-ICE2015) was a ship-based measurement campaign based on in-ice drift in the area north of Svalbard throughout the winter and spring season of 2015. During this campaign, atmospheric measurements of temperature, wind speed and wind direction, air pressure and air humidity were conducted from both the Norwegian Polar Institute's research vessel *Lance* and from measurement towers launched on icefloes.

Based on this campaign, Graham *et al.* (2017b) describe two typical atmospheric states occurring during the winter season; the most common was a “radiatively clear state”, with cold temperatures, mostly clear skies and stable conditions. This was regularly disrupted by storms leading to periods of a “radiative opaque state” with increased cloud cover and atmospheric moisture, and drastic increases in temperature of up to 30 K, from around -30°C to around zero. These storm events would normally last for a few days. Typically, the strong events measured north of Spitsbergen were part of large-scale circulation patterns. Graham *et al.* (2017b) also highlight that the entire winter period of the N-ICE2015 campaign was characterized by an anomalously large meridional component of the jet stream that drove several intense storms into the high Arctic (north of 80°N).

One such episode occurred on 21–22 January 2015. Figure 4 shows the temperature anomalies associated with this event, along with the geopotential height contours at 850 hPa, 3 days ahead of, during, and 3 days after the event. On the day of the event, we see temperature anomalies of up to $+15\text{K}$ centred around the Svalbard region, and geopotential height contours indicate a strong southwesterly geostrophic wind component (Figure 4, middle panel).

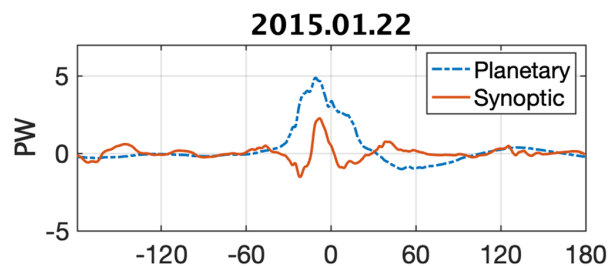


FIGURE 5 Daily mean latent energy transport anomaly (PW) across 70°N on 22 January 2015, as a function of longitude ($^{\circ}\text{E}$). The planetary-scale transport is comprised of waves 1–3, and the synoptic-scale transport of waves 4–21 [Colour figure can be viewed at wileyonlinelibrary.com]

Based on the Fourier decomposition of the transport along 70°N on this particular day (Figure 5), we see that the transport on that day is concentrated just southeast of Spitsbergen, for both the planetary-scale and the synoptic-scale transport. The planetary-scale transport dominates, reflecting the large-scale component of the event.

In the Fourier decomposition, 22 January is recognized as an extreme transport event on the planetary scale, i.e. a day when the planetary-scale transport exceeded the 90th percentile for the 2015 winter season. This corresponds well with the observations of the anomalously large meridional component of the jet stream over this area, as noted by Cohen *et al.* (2017). The energy transport and this particular event is as such described as being a result of atmospheric mechanisms on various scales.

However, one should also note that the synoptic-scale transport is large in this area, even though this anomaly is not large enough to qualify as an extreme case during this season. The local cyclone's contribution to the decomposed transport is captured by the synoptic-scale

TABLE 1 Trends in energy transport components (PW·decade⁻¹). Trends are based on a linear regression of seasonal averages of daily values

	DJF	MAM	JJA	SON
Planetary vQ	0.005 ($p = .07$)	-0.002 ($p = .23$)	-0.001 ($p = .36$)	0.0008 ($p = .41$)
Synoptic vQ	-0.003 ($p = .03$)	0.002 ($p = .14$)	0.0055 ($p = .04$)	-0.0015 ($p = .23$)

Note: Bold numbers indicate trends that are statistically significant at a 90% level, according to a Monte Carlo type test with 5,000 simulations. Three-monthly, starting in December.

waves, but again it does not impact the zonal average transport enough to qualify the daily mean transport anomaly as an extreme event.

The aim with presenting this case-study is to show an example of how energy transport from a particular and well-documented extreme event is represented by the Fourier decomposition method. It illustrates key features of the Fourier decomposition method; by decomposing the transport of this event into different spatial scales, it is able to identify the large-scale transport as the more unusual part of the total event, even though the synoptic-scale transport also played an important role.

However, as previously mentioned, it is important to keep in mind that a highly localized single event may not be fully represented by the Fourier method if it is that this method relies on sinusoidal waves (Heiskanen *et al.*, 2020). In such cases the method may underestimate the transport from the synoptic-scale part of the transport to some degree. However, applying the wavelets decomposition method as proposed by Heiskanen *et al.* (2020), which better represents highly localized systems, confirms that this is not a synoptic-scale extreme transport event (not shown).

3.3 | Changes in transport components

The LE transport on various scales and seasons affects the Arctic in different ways. Changes in the relative magnitude of planetary- and synoptic-scale transport may therefore have contributed to Arctic climate change. Here, we investigate whether such changes can be identified in the four decades of data covered by the ERA5 dataset.

By using a simple least-squares regression analysis on annual mean anomalies for the 40-year period (1979–2018) we find that the LE transport increased slightly over the past 40 years (not statistically significant). By investigating the trends in mean seasonal anomalies across the 40 years, we find significant trends in both the summer (Table 1) and winter seasons (Figure 6).

We find a mean increase in the winter season LE transport by planetary waves across 70°N of 0.005 PW·decade⁻¹ (p -value = .07), and the synoptic transport decrease over

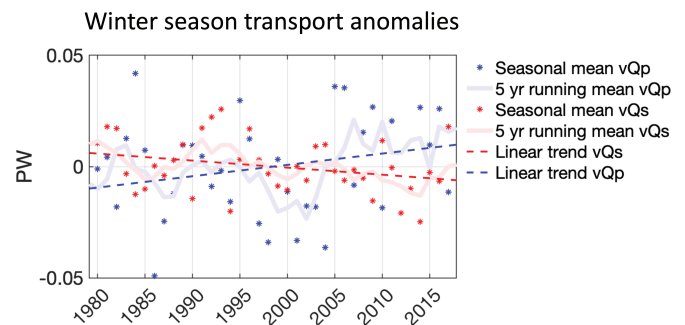


FIGURE 6 Seasonal anomalies in latent energy transport (dots, PW) for planetary-scale transport (blue) and synoptic-scale transport (red), by year. Thick lines show a 5-year moving average, and stippled lines the linear trends based on linear regression. LE transport by planetary waves across 70°N increase 0.005 PW·decade⁻¹ (p -value = .07). The winter season synoptic transport decreases by 0.003 PW·decade⁻¹ (p -value = .03). Statistical significance is based on a Monte Carlo approach with 5,000 simulations

the same period by 0.003 PW·decade⁻¹ (p -value = .03) (Figure 6). Due to the larger temperature effect related to latent energy transport in winter as compared to summer, we focus on the winter season; however, trends for both scales and all seasons are given in Table 1.

3.4 | Changes in the extreme cases

When investigating the upper percentiles of the seasonal trends, we find that the increase in the mean winter-time transport by planetary-scale waves is largely owing to an increase in the uppermost extreme transport events (Figure 7). The increase is larger (as indicated by steeper trend lines) for higher percentile values, indicating that the seasonal level of extreme cases on average increases through the period.

The same pattern is seen in the decrease in transport by synoptic-scale systems, which is also largely owing to a decrease in the upper extreme values (Figure 7, bottom panel). The lower percentiles show no specific trends on either scale (not shown). The explanation for this increase in the level of very strong transport events might

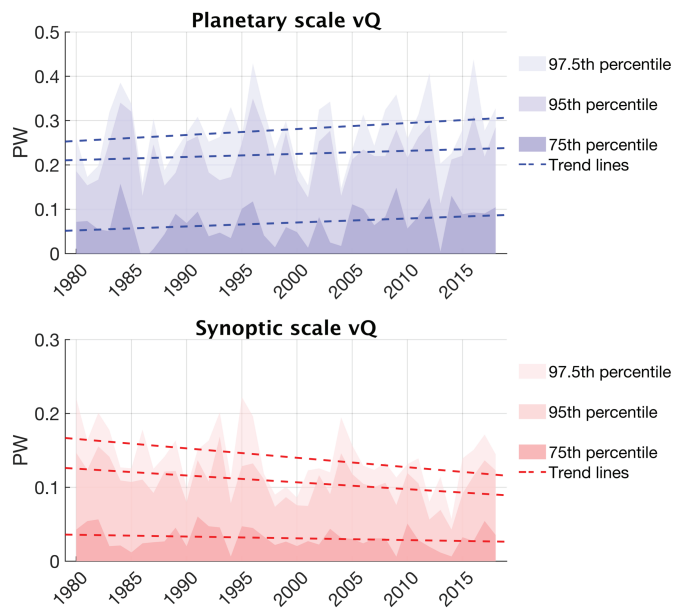


FIGURE 7 Seasonal mean winter (December–February) anomalies in latent energy transport (PW) across 70°N by planetary-scale waves (upper panel) and synoptic-scale waves (lower panel) over the time period 1979–2018. Shading indicates the 75th, 95th and 97.5th percentiles per winter season, from weakly to heavily transparent colours, respectively. Stippled lines indicate the linear trends in the respective percentile values. Note the difference in scale between panels

lie with the general increase in humidity in the atmosphere causing strong transport events to increase, or with circulation changes causing increased winds and transport, or a combination of both. As the former explanation should lead to a general increase of the transport on all levels, this skewed increase might point in the direction of the latter.

The same overall pattern of trends in the wintertime LE transport is found in the ERA-Interim dataset decomposed by the wavelet decomposition method (Figure S2 and S3), which inherently has a negligibly different distribution of planetary- and synoptic-scale events as compared to the Fourier method. This shows that the trends are not sensitive to the method of decomposition, and rather a robust feature of the energy transport.

A decrease in strong cyclones over the past decades is also confirmed in a completely alternative method of identifying synoptic-scale systems. In this method, cyclone track points were identified as in the cyclone tracking algorithm by Hodges (1999). From the 6-hourly ERA-Interim dataset, track points were identified by local maxima exceeding a threshold of $5 \times 10^{-5} \text{ s}^{-1}$ in the relative vorticity spectrally filtered between wave numbers 40 and 100. For the comparison, only cyclone track points within a latitude belt of $70^\circ\text{N} \pm 2^\circ$ were considered. In this dataset we also observe a downward trend in the intensity of the

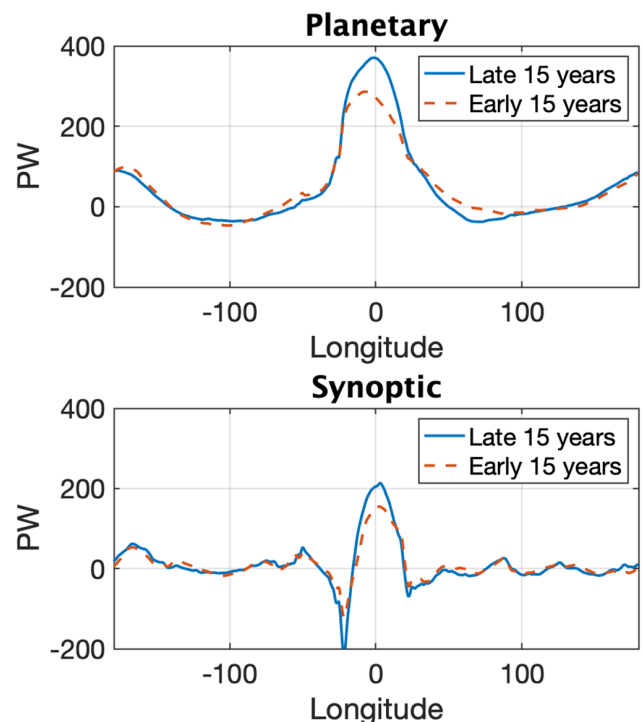


FIGURE 8 Distribution of latent energy transport along 70°N shown as sum of daily mean energy (PW) for days with extreme transport events (exceeding the 90th percentile of each season), by longitude (°E). Stippled lines shows the sum of extreme days over the early 15 winter seasons (1979–1993), while whole lines shows extreme days over the late 15 winter seasons (2004–2018) [Colour figure can be viewed at wileyonlinelibrary.com]

97.5th percentile as computed per season (Figure S4). This is consistent with our findings of a decreasing trend in wintertime strong cyclones passing the 70°N latitude and into the Arctic.

By comparing the first 15 to the last 15 winter seasons of the 40-year time series, we can investigate changes in the placement of extreme transport events. There have been no major shifts in the locations of the planetary- and synoptic-scale systems entering the Arctic region along the 70°N latitude (Figure 8). The main changes are found in the Atlantic sector, where the extreme events in wintertime planetary transport are about 100 PW larger over the last as compared to the early 15 years (Figure 8, top panel). This is consistent with findings showing that this area has experienced an increase in temperatures and downwards longwave radiation (LWD) over recent decades which has been shown to have been driven by an increased atmospheric moisture advection from lower latitudes due to changes in the large-scale atmospheric circulation (Park *et al.*, 2015). On the synoptic scale (Figure 8, lower panel), a smaller increase can be seen in the northward direction, and there is also an increase in the southward direction, west of the northward peak.

4 | DISCUSSION

When we examine the mean LE transport across 70°N over the past 40 years, we find a positive trend in the wintertime LE transport anomalies on the planetary scale, with the steepest increase in the most extreme events. This trend is important as we find that extreme events in wintertime latent energy transport by planetary-scale systems are more closely associated with anomalous warming in the Arctic than extreme transport events by the synoptic-scale systems. The warm anomalies last for several days and spread across the entire Arctic basin. This dependence on wave scale confirms findings by Graversen and Burtu (2016). In our study, a planetary-scale extreme event on average raises the mean temperature by 0.6 K in winter, averaged across the Arctic ($>70^{\circ}\text{N}$). However, the warming as well as the majority of extreme cases are concentrated in the North Atlantic area where the associated area-average warming during extreme events is 2.6 K in winter. Comparing the early 15 to the latest 15 winter seasons, we see that the changes in extreme transport events are also mainly confined to the North Atlantic region. It is likely that the positive trend in planetary-scale extreme events in this area, combined with the strong warming signal associated with such events, have contributed to the increased warming observed in the North Atlantic Arctic area over the past decades. It is also consistent with findings of increased LE flux into this area over the past decades (Park *et al.*, 2015; Woods and Caballero, 2016; Dahlke and Maturilli, 2017; Graham *et al.*, 2017a). Dahlke and Maturilli (2017) also showed an increase in the duration of strong wintertime warming events in the North Atlantic region of the Arctic of $0.45\text{ K}\cdot\text{decade}^{-1}$ over the past decades, which is coherent with an increase in the planetary-scale events, which on average warm the Arctic over several days.

On the synoptic scale, we find that extreme transport events across 70°N have decreased in winter over the past four decades, and that the decrease is largest for the most extreme events. During synoptic-scale events, cold temperature anomalies dominate as averaged over 5 days before and during the events. Temperature anomalies 5 days after synoptic events are small, and the significant anomalies in the temperature gradients appear to have been dissolved.

For the synoptic scale, it seems that the associated temperature patterns are responsible for the synoptic-scale transport events, rather than the response to them. As the synoptic-scale systems are largely driven by local temperature gradients acting to increase the baroclinicity, increased winter temperatures in the Barents and Kara Seas may have contributed to a decrease in extreme transport events across 70°N in the North Atlantic, where also the majority of extreme synoptic events in winter occur.

The Barents and Kara Seas have been identified as the most prominent area for Arctic amplified warming (Park *et al.*, 2015). This warming has been shown to cause shifts in the synoptic-scale activity in the area due to decreased temperature gradient, and may have caused strong cyclone activity to decrease and/or shift paths (Inoue *et al.*, 2012).

The decrease in synoptic-scale transport across 70°N is also confirmed using the wavelet decomposition method, and with a completely alternative method of identifying synoptic-scale events, based on a cyclone tracking algorithm applied to the ERA-Interim reanalysis. The same pattern of strong decrease in intensity of wintertime extreme events is seen in these datasets, although trends are smaller than in the Fourier-based decomposition.

Synoptic-scale storm systems are often closely related to large, planetary-scale circulation systems (Simmonds *et al.*, 2008) and as such, a typical strong storm in high latitudes is often a result of a combination of large-scale circulation systems and favourable local conditions. The combination is responsible for bringing large amounts of latent energy into the Arctic. For example, large blocking systems can act to deflect small synoptic-scale systems northward, as observed by Woods *et al.* (2013), resulting in these synoptic-scale systems reaching further north and deeper into the Arctic. Cohen *et al.* (2017) similarly observed that strong wintertime storm systems in the Svalbard region were steered north by a large-scale hemispheric circulation pattern. In such cases, where the synoptic system is part of a greater circulation pattern, the associated energy transport may contribute to either scale in the Fourier decomposition. Papritz and Dunn-Sigouin (2020) showed that the planetary-scale transport is closely linked to large-scale blocking situations that act to deflect cyclone tracks poleward, thereby causing a strong northward transport in the interaction between the blocking system and upstream cyclones.

Therefore, our finding of increased planetary-scale transport and other findings of increase in extreme synoptic events (e.g. Rinke *et al.*, 2017) is not conflicting, but rather describes different features of the same trends. This is exemplified in the case-study selected here: In the case-study from the N-ICE2015 measurement campaign, a planetary-scale circulation pattern with a particularly strong northward component of the polar jet stream was identified as necessary for the synoptic-scale storm system to reach the measurements site north of Svalbard, as described by Cohen *et al.* (2017). This event was recognized as an extreme transport event on the planetary scale using the Fourier decomposition method. On the synoptic scale, the storm system as experienced from the ship was not recognized as particularly extreme.

This is further exemplified in Heiskanen *et al.* (2020), who evaluated the Fourier method for estimating

planetary- and synoptic-scale transport, and compared it to an alternative method using wavelets. The alternative wavelet method, which is based on localized functions, proved more skilful at resolving synoptic-scale single systems. With regard to the case studied here, the wavelet method confirmed that the event did not qualify as an extreme event on the synoptic scale. However, the wavelet method did not confirm that planetary-scale transport was an extreme event as proposed by the Fourier method, but this could be related to the wavelet method's risk of under-representing planetary-scale events.

In Heiskanen *et al.* (2020), regression analyses using both methods show a strong warming signal inside the Arctic resulting from planetary-scale transport, and a much weaker signal associated with synoptic-scale transport; however, the distribution is more even in the wavelet method as compared to the Fourier method. Here, we have chosen to lower the wave number of the split between planetary and synoptic scales as compared to that in Graversen and Burtu (2016), as suggested in Heiskanen *et al.* (2020), to better represent the wavelengths of planetary- and synoptic-scale systems in high latitudes. By performing the same type of analysis of the extreme events on each scale while using the wavelet decomposition method, we find that the same wintertime trends and general pattern of temperature anomalies associated with extreme events as in the Fourier decomposition dataset. This shows that the conclusions drawn here are not sensitive to the decomposition method, but rather robust features of synoptic- and planetary-scale energy transport.

5 | CONCLUDING REMARKS


We find a mean decrease in wintertime synoptic-scale transport and an increase in planetary-scale transport over the past 40 years. We show that this shift has the potential to both increase the amount of latent energy that reaches deep into the high Arctic, and to contribute to increased winter season warming, even if the total annual mean energy transport stays the same. The effect of LE transport on Arctic climate has been documented thoroughly; however, to our knowledge, this is the first study to quantify the seasonal trends of the planetary- and synoptic-scale components of the transient meridional energy transport separately. These findings contribute to explaining the increase in LE fluxes and warm winter periods observed in the Arctic over the past decades. Lastly, these results raise questions about mechanisms responsible for the identified trends in planetary- and synoptic-scale LE transport in winter, and to future impact of these changes on the Arctic climate.

ACKNOWLEDGEMENTS

This work was funded by the Norwegian Research Council (NFR) under the project “The role of the atmospheric energy transport in recent Arctic climate change” (project no. 280727), and the NOTUR projects NN3948k and NS9063k. We would like to thank the ERA5 group and the ERA-Interim team for providing the datasets for these analyses.

ORCID

J. H. Rydsaa  <https://orcid.org/0000-0002-0538-0714>

T. I. H. Heiskanen  <https://orcid.org/0000-0003-0113-0627>

P. J. Stoll  <https://orcid.org/0000-0003-1120-2049>

REFERENCES

- Bekryaev, R.V., Polyakov, I.V. and Alexeev, V.A. (2010) Role of polar amplification in long-term surface air temperature variations and modern Arctic warming. *Journal of Climate*, 23, 3888–3906.
- Bengtsson, L., Hodges, K.I., Koumoutsaris, S., Zahn, M. and Berrisford, P. (2013) The changing energy balance of the polar regions in a warmer climate. *Journal of Climate*, 26, 3112–3129.
- Boisvert, L.N. and Stroeve, J.C. (2015) The Arctic is becoming warmer and wetter as revealed by the atmospheric infrared sounder. *Geophysical Research Letters*, 42, 4439–4446.
- Cohen, L., Hudson, S.R., Walden, V.P., Graham, R.M. and Granskog, M.A. (2017) Meteorological conditions in a thinner Arctic sea ice regime from winter to summer during the Norwegian Young Sea Ice expedition (N-ICE2015). *Journal of Geophysical Research: Atmospheres*, 122, 7235–7259.
- Dahlke, S. and Maturilli, M. (2017) Contribution of atmospheric advection to the amplified winter warming in the Arctic North Atlantic region. *Advances in Meteorology*, 2017, 4928620. <https://doi.org/10.1155/2017/4928620>.
- Dee, D.P., Uppala, S.M., Simmons, A.J., Berrisford, P., Poli, P., Kobayashi, S., Andrae, U., Balmaseda, M.A., Balsamo, G., Bauer, P., Bechtold, P., Beljaars, A.C.M., van de Berg, L., Bidlot, J., Bormann, N., Delsol, C., Dragani, R., Fuentes, M., Geer, A.J., Haimberger, L., Healy, S.B., Hersbach, H., Hólm, E.V., Isaksen, I., Kållberg, P., Köhler, M., Matricardi, M., McNally, A.P., Monge-Sanz, B.M., Morcrette, J.J., Park, B.-K., Peubey, C., De Rosnay, P., Tavolato, C., Thépaut, J.-N. and Vitart, F. (2011) The ERA-Interim reanalysis: configuration and performance of the data assimilation system. *Quarterly Journal of the Royal Meteorological Society*, 137(656), 553–597.
- Ding, Q.H., Schweiger, A., L'Heureux, M., Battisti, D.S., Po-Chedley, S., Johnson, N.C., Blanchard-Wrigglesworth, E., Harnos, K., Zhang, Q., Eastman, R. and Steig, E.J. (2017) Influence of high-latitude atmospheric circulation changes on summertime Arctic sea ice. *Nature Climate Change*, 7, 289–295.
- Dufour, A., Zolina, O. and Gulev, S.K. (2016) Atmospheric moisture transport to the Arctic: assessment of reanalyses and analysis of transport components. *Journal of Climate*, 29, 5061–5081.
- Gong, T.T., Feldstein, S. and Lee, S. (2017) The role of downward infrared radiation in the recent Arctic winter warming trend. *Journal of Climate*, 30, 4937–4949.

- Graham, R.M., Cohen, L., Petty, A.A., Boisvert, L.N., Rinke, A., Hudson, S.R., Nicolaus, M. and Granskog, M.A. (2017a) Increasing frequency and duration of Arctic winter warming events. *Geophysical Research Letters*, 44, 6974–6983.
- Graham, R.M., Rinke, A., Cohen, L., Hudson, S.R., Walden, V.P., Granskog, M.A., Dorn, W., Kayser, M. and Maturilli, M. (2017b) A comparison of the two Arctic atmospheric winter states observed during N-ICE2015 and SHEBA. *Journal of Geophysical Research: Atmospheres*, 122, 5716–5737.
- Graversen, R.G. (2006) Do changes in the midlatitude circulation have any impact on the Arctic surface air temperature trend? *Journal of Climate*, 19, 5422–5438.
- Graversen, R.G. and Burtu, M. (2016) Arctic amplification enhanced by latent energy transport of atmospheric planetary waves. *Quarterly Journal of the Royal Meteorological Society*, 142(698), 2046–2054.
- Graversen, R.G. and Langen, P.L. (2019) On the role of the atmospheric energy transport in $2 \times \text{CO}_2$ -induced polar amplification in CESM1. *Journal of Climate*, 32, 3941–3956.
- Graversen, R.G., Mauritsen, T., Tjernström, M., Källén, E. and Svensson, G. (2008) Vertical structure of recent Arctic warming. *Nature*, 451, 53–56.
- Heiskanen, T., Graversen, R.G., Rydsaa, J.H. and Isachsen, P.E. (2020) Comparing wavelet and Fourier perspectives on the decomposition of meridional energy transport into synoptic and planetary components. *Quarterly Journal of the Royal Meteorological Society*, 146(731), 2717–2730.
- Hersbach, H., Bell, B., Berrisford, P., Hirahara, S., Horányi, A., Muñoz-Sabater, J., Nicolas, J., Peubey, C., Radu, R., Schepers, D., Simmons, A., Soci, C., Abdalla, S., Abellan, X., Balsamo, G., Bechtold, P., Biavati, G., Bidlot, J., Bonavita, M., De Chiara, G., Dahlgren, P., Dee, D.P., Diamantakis, M., Dragani, R., Flemming, J., Forbes, R., Fuentes, M., Geer, A., Haimberger, L., Healy, S., Hogan, R.J., Hólm, E., Janisková, M., Keeley, S., Laloyaux, P., Lopez, P., Lupu, C., Radnoti, G., de Rosnay, P., Rozum, I., Vamborg, F., Villaume, S. and Thépaut, J.-N. (2020) The ERA5 global reanalysis. *Quarterly Journal of the Royal Meteorological Society*, 146(730), 1999–2049.
- Hodges, K.I. (1999) Adaptive constraints for feature tracking. *Monthly Weather Review*, 127, 1362–1373.
- Holton, J.R. and Hakim, G.J. (2013) An introduction to dynamic meteorology. 5 ed. Vol. 88, 552 pp.
- Hwang, Y.-T., Frierson, D.M.W. and Kay, J.E. (2011) Coupling between Arctic feedbacks and changes in poleward energy transport. *Geophysical Research Letters*, 38(17). <https://doi.org/10.1029/2011GL048546>.
- Inoue, J., Hori, M.E. and Takaya, K. (2012) The role of Barents Sea ice in the wintertime cyclone track and emergence of a warm-Arctic cold-Siberian anomaly. *Journal of Climate*, 25, 2561–2568.
- Koenigk, T., Brodeau, L., Graversen, R.G., Karlsson, J., Svensson, G., Tjernström, M., Willén, U. and Wyser, K. (2013) Arctic climate change in 21st century CMIP5 simulations with EC-Earth. *Climate Dynamics*, 40, 2719–2743.
- Liu, C.J. and Barnes, E.A. (2015) Extreme moisture transport into the Arctic linked to Rossby wave breaking. *Journal of Geophysical Research: Atmospheres*, 120, 3774–3788.
- Papritz, L. and Dunn-Sigouin, E. (2020) What configuration of the atmospheric circulation drives extreme net and total moisture transport into the Arctic. *Geophysical Research Letters*, 47(17), e2020GL089769.
- Park, D.S.R., Lee, S. and Feldstein, S.B. (2015) Attribution of the recent winter sea ice decline over the Atlantic sector of the Arctic Ocean. *Journal of Climate*, 28, 4027–4033.
- Peixoto, J.P. and Oort, A.H. (1992) *Physics of Climate*. New York, NY: American Institute of Physics.
- Rinke, A., Maturilli, M., Graham, R.M., Matthes, H., Handorf, D., Cohen, L., Hudson, S.R. and Moore, J.C. (2017) Extreme cyclone events in the Arctic: wintertime variability and trends. *Environmental Research Letters*, 12, 094006.
- Serreze, M.C. and Barry, R.G. (2011) Processes and impacts of Arctic amplification: a research synthesis. *Global and Planetary Change*, 77, 85–96.
- Serreze, M.C. and Francis, J.A. (2006) The Arctic amplification debate. *Climatic Change*, 76, 241–264.
- Simmonds, I., Burke, C. and Keay, K. (2008) Arctic climate change as manifest in cyclone behavior. *Journal of Climate*, 21, 5777–5796.
- Skific, N. and Francis, J.A. (2013) Drivers of projected change in Arctic moist static energy transport. *Journal of Geophysical Research: Atmospheres*, 118, 2748–2761.
- Trenberth, K.E. (1991) Climate diagnostics from global analyses: conservation of mass in ECMWF analyses. *Journal of Climate*, 4, 707–722.
- Woods, C. and Caballero, R. (2016) The role of moist intrusions in winter Arctic warming and sea ice decline. *Journal of Climate*, 29, 4473–4485.
- Woods, C., Caballero, R. and Svensson, G. (2013) Large-scale circulation associated with moisture intrusions into the Arctic during winter. *Geophysical Research Letters*, 40, 4717–4721.
- Yoshimori, M., Abe-Ouchi, A. and Laine, A. (2017) The role of atmospheric heat transport and regional feedbacks in the Arctic warming at equilibrium. *Climate Dynamics*, 49, 3457–3472.

SUPPORTING INFORMATION

Additional supporting information may be found online in the Supporting Information section at the end of this article.

How to cite this article: Rydsaa JH, Graversen RG, Heiskanen TIH, Stoll PJ. Changes in atmospheric latent energy transport into the Arctic: Planetary versus synoptic scales. *QJR Meteorol Soc.* 2021;147:2281–2292. <https://doi.org/10.1002/qj.4022>



Paper III

Heiskanen, Tuomas, Rune G. Graversen, Richard Bintanja, and Heiko Goelzer (in review 2022a). "Abrupt increase in Greenland melt enhanced by wind changes." In: Submitted for review.

Abrupt increase in Greenland melt enhanced by wind changes

Tuomas Heiskanen¹, Rune G. Graversen^{1,2}, Richard Bintanja³, and Heiko Goelzer⁴

Abstract:

Greenland ice-sheet melt constitutes an alarming contribution to global sea-level rise. Observations indicate that the ice sheet was in approximate balance until the late 1990s, after which strong melting occurred. The reason for this sudden change has not been understood; it cannot be attributed linearly to climate change as this occurs gradually. Here we show that the abrupt shift to a strong melting state is associated with changes of the atmospheric circulation over Greenland. This is evident from applying a newly-developed methodology effectively decomposing atmospheric flow patterns into parts associated with Rossby waves and smaller perturbations. A Rossby-wave-induced reduction of the westerly flow, which is consistent with anthropogenic Arctic warming, led to a decrease in precipitation and an increase in surface warming, contributing to ice-sheet mass loss, in particular over the southwestern regions. Hence the Greenland ice-sheet melt is an example of a climate response non-linearly coupled to global warming.

Sea-level rise constitutes one of the major climate-change threads to humanity. Recent melting of the Greenland ice sheet is unprecedented since the mid-Holocene (for about 8 thousands years ago)¹, and implies a critical contribution to the rising of sea levels. The Greenland ice sheet has since the late 1990s encountered a substantial mass loss²⁻⁵, which has severe implications for ongoing and future global sea-level rise, should the melting pace continue⁶. Additionally, the melting has led to a increase in release of methane from the ice-sheet bed⁷, contributing to further greenhouse-gas-induced global warming. The ice-sheet mass loss is most severe along the margins of the ice sheet – in particular in the southwestern part of Greenland^{3,5}. The mass loss is mainly due to a negative surface-mass balance^{3,8} (SMB, precipitation minus melting), although increase of discharge of outlet glaciers in fjords by calving and submarine melting (D, dynamical discharge) also provides a significant contribution^{5,9,10}.

It has been argued that atmospheric processes play an important role in this strong recent mass loss^{4,11-15}. Melting occurs when energy convergence of various energy fluxes raises the temperature to the melting point which predominantly occurs close to the atmosphere-ice interface, and is therefore associated with the surface energy balance. If runoff from melting is not balanced by increase in precipitation, a negative SMB is induced¹⁶.

The surface energy balance at the atmosphere–ice-sheet interphase includes net solar ra-

¹Department of Physics and Technology, UiT The Arctic University of Norway, Tromsø, Norway

²Norwegian Meteorological Institute, Tromsø, Norway

³Royal Netherlands Meteorological Institute (KNMI), De Bilt, Netherlands

⁴NORCE Norwegian Research Centre, Bjerknes Centre for Climate Research, Bergen, Norway

diation (downward minus reflected), net longwave radiation (downward minus upward) and net turbulent heat and moisture fluxes where the latter is a latent heat flux associated with sublimation and icing – depositional frost and frozen dew. The surface energy balance can provide a net energy input from above into the ice sheet when temperatures are below the freezing point, and energy for melting when temperatures are at this freezing point. Turbulent heat fluxes of both the sensible and latent type can be important drivers of extreme melt events of the Greenland ice sheet¹⁸. For example during the extreme melt event of summer 2012¹⁹, the turbulent heat fluxes were as important as the radiative effects²⁰. Also clouds, humidity, and temperature over the ice sheet strongly control downwelling short and longwave radiation as well as the turbulent fluxes at the ice-atmosphere interface, and are hence important for the ice melt. For instance clouds have a net heating effect over ice sheets^{15,18,21}, although clouds can cause cooling in case the albedo of the ice is low. In addition atmospheric processes may affect dynamical discharge, as melt water induced by atmospheric forcing can penetrate to the bottom of the ice sheet where it causes increased lubrication and affects speed of outlet glaciers. However the process is complex and it is unclear whether the net effect is a speed-up or a slow-down of the outlet streams²².

Surface energy balance

A negative SMB is associated with melting and hence with net convergence of energy by the ice sheet, especially in the surface-near layer just below the atmosphere-ice interface. Convergence of energy in this layer is mostly given by surface energy balance (see Methods) since energy flux from below and lateral energy fluxes within the ice are small. Consistently, regressions of the surface energy balance on the SMB (see Methods) show a positive energy balance implying a negative SMB at the western and northern ice-sheet margins, but a positive SMB in the interior and eastern margins (Fig. 1a). The latter pattern is due to a strong correlation between surface-energy balance and precipitation that appears since cloudy weather leading to precipitation is also causing positive energy-flux anomalies at the surface. When removing the part of the surface energy balance that is temporally correlated with the precipitation, by applying a decorrelation method (see Methods), the correlation coefficients show mostly negative or little SMB impact along the margins, and little response in the interior where temperatures are mainly negative, even during positive surface-energy-balance anomalies (Fig. 1b). Hence a positive energy balance causes melting and a negative SMB in areas where the temperature can easily be raised to the melting point. Predominantly negative temperatures are also prevailing at high altitudes in the mountains in the south-east where accordingly less negative SMB impact of the surface energy balance is encountered as compared to other parts of the ice-sheet margins. Precipitation, all though not decorrelated with the surface energy balance, provides a positive SMB over the ice sheet everywhere, but mainly at the ice-sheet margins where altitude gradients are the largest (Fig. 1c). Hence as expected, the regressions reveal that both the surface energy balance and precipitation play an important role for the SMB.

The surface energy balance is controlled by atmospheric conditions such as clouds, hu-

midity and temperature. These quantities are strongly impacted by advection due to the atmospheric circulation. Hence as a consequence of this chain of processes, it can be hypothesised that the atmospheric circulation provides a strong control of the SMB. Several studies have indicated a change in the atmospheric circulation over Greenland, which is suggested to have had an impact on the SMB^{25,26}. It has been noted that a general increase in moistening of the Arctic atmosphere is associated with changes in northward latent heat transport²³. It has also been argued that blocking events over Greenland lead to transport of warm and moist air over the ice sheet^{17,24}, affecting both the surface energy balance and precipitation, and hence the SMB of the ice sheet. Strong moisture advection events - known as atmospheric rivers - are associated with increase in clouds, temperature, and winds which lead to a positive surface energy balance especially due to the turbulent sensible heat flux¹⁸. In addition, temperatures at coastal stations are correlated with atmospheric circulation indices such as the North-Atlantic Oscillation (NAO)^{12,13,19}.

Atmospheric circulation transports both sensible heat (dry-static) and moisture, and the convergence of these transport components over Greenland will affect both surface energy balance and precipitation, which mostly have opposite impacts on the SMB (Fig. 1). Hence, in order to estimate the linkage between atmospheric energy advection and the SMB, it is important to decompose the transport by the atmospheric circulation into parts.

Atmospheric energy advection over Greenland

The energy transport by the atmospheric circulation can be decomposed into a dry-static and a latent component, where the former is associated with the advection of sensible heat and the latter with the transport of moisture (see Methods). Convergence of these two components leads to an increase of energy transfer to the surface²⁷. The latent component affects the surface energy balance considerably more than its dry-static counterpart²⁷, due to the enhancement of the local greenhouse effect associated with increase in water-vapour and clouds resulting from latent transport convergence. In addition, the latent transport convergence increases precipitation. Since the dry-static and latent transport have different impacts on the surface-energy balance and precipitation, the two types of transport affect the Greenland ice-sheet in different ways.

Moreover, the type of circulation pattern plays a role: atmospheric advection is accomplished by *e.g.* large-scale planetary waves – also known as Rossby waves, synoptic-scale waves such as cyclones, and smaller perturbations. The atmospheric waves impact Arctic weather and climate²⁸, and the planetary-scale waves have a much larger potential to cause warming over the Arctic than smaller waves including cyclones, since the Rossby waves as compared to cyclones can affect a much larger area by simultaneous energy convergence^{27,29}. Hence in the following the atmospheric energy transport is decomposed into dry-static and latent components and further into Rossby and small-scale waves, where the latter is associated with synoptic-scale and meso-scale disturbances. In order to estimate a linear statistical linkage between transport components and the SMB, regressions of the SMB on the transport components are investigated. As for the surface

energy balance, the various transport components are first decorrelated with each other before regressions are performed (see Methods).

When it comes to the impact of dry-static transport on the Greenland surface-mass balance, both Rossby and smaller-scale waves cause melting over Greenland, but in contrast to the pan-Arctic studies^{27,28} this impact is larger for the waves at the smaller scales than for the Rossby waves (Fig. 2a-b). For the smaller-scale-wave type, the melting is the largest at the ice-sheet margins, likely due to the proximity to the sea and hence to a heat source for the smaller-scale disturbances (Fig. 2b). In the southeast where the melting is the largest the adjacent sea is normally ice free – even in winter – implying a strong heat source and temperature gradients important for baroclinic and convective development of smaller-scale disturbances. In contrast, the latent transport induces a positive SMB indicating that advection of moisture into Greenland is associated with increase in precipitation, and that this precipitation effect of the latent transport is exceeding its melting effect due to increased energy transfer to the surface associated with increase in humidity and cloud water (Fig. 2c-d). As for the dry-static component, the impact appears larger for the synoptic-scale wave than for the Rossby-wave types. This is supporting earlier findings that cyclones are important for both melting and precipitation over the ice sheet¹⁴. The regression coefficients being larger for the smaller-scale waves than for the Rossby waves may appear surprising in light of earlier studies revealing a much stronger impact on the Arctic weather and climate by Rossby waves than cyclones^{27,28}, but this apparent contradiction is partly related to differences in method between the two sets of studies (see Methods).

Trend in surface-mass balance

The Greenland ice-sheet SMB has been in almost balance at least from the 1960s to 1990s^{3,5,30}, after which a negative trend emerged (Fig. 3b-c). Hence, the melt of the Greenland ice sheet shows a non-linear development relative to the ongoing, fairly steady global warming. Given the strong impact of atmospheric circulation on the Greenland SMB, such a non-linear coupling between the ongoing climate change and the Greenland ice-sheet melt can emerge if the atmospheric circulation responds irregularly to global warming. An indication that atmospheric circulation plays an important role for decadal variability of the Greenland SMB is provided by a change in the zonal (west-erly) atmospheric mass flux over Greenland (Fig. 3a-b). The mass flux shows a clear and significant change between decades after and before 2000. The mass flux brings energy and water vapour in over Greenland and a change of the mass flux will therefore affect the Greenland SMB.

The difference of Greenland SMB between the period of trend (1999-2018) and the period of stability (1979-1999) shows that in recent decades, melt has occurred predominantly in the south-western part of Greenland³ (Fig. 3b-c). Also in this region a clear shift in both SMB and atmospheric mass flux are found at about year 2000 (Fig. 3b). In general, a negative SMB trend is encountered along the margins of the ice-sheet except in the mountain areas in the south-eastern part.

Circulation changes causing ice melt

A shift in both Rossby waves and small-scale waves have in general increased convergence of dry-static energy transport over Greenland, although a decrease is found mainly in the mountains in the southeast, and for the Rossby wave part, at the central-western ice-sheet margin (Fig. 4a-b). The increase is the largest in the southwest region and associated with the Rossby waves. A combination of regressions and trends (see Methods) indicates that the shift in the Rossby wave transport of dry-static energy has induced melting in the south-western part, whereas the transport by smaller-scale waves has caused melting at the central-western ice-sheet margin (Fig. 5a-b). In addition, a decrease in convergence of dry-static energy in the mountain areas in the southeast has contributed to a positive SMB there.

A shift in Rossby waves has brought less water vapour into the southwestern part, but more to the mountains in the southeast (Fig. 4c). In contrast, about the opposite pattern is the case for the small-scale waves (Fig. 4d). The shift in the latent transport by Rossby waves has contributed to a negative SMB in the southwest Greenland, which is partly compensated by a positive trend induced by a change of the latent transport by small-scale waves over this area (Fig. 5c-d). Therefore in sum, over the southwest Greenland changes of the Rossby waves have led to ice loss both due to enhanced melting from an increased transport of heat, and due to less accumulation due to a reduced transport of water vapour. Hence both dry-static and latent transport by Rossby waves have induced a negative change in SMB in this area, which is partly counteracted by an increase in precipitation associated with the enhanced transport of water vapour by small-scale waves.

For the shift in Rossby-waves energy transport, an opposite pattern between the dry-static and the latent components is found in the southern part of Greenland. The time-mean mass flow over Greenland is from west to east. The dry-static part shows convergence increase at the upstream western side and decrease at the downstream eastern side, and the opposite is the case for the latent transport (Fig. 4a,c). This is consistent with a decrease of the westerly time-mean flow (Fig. 3a). This westerly flow decrease causes less transport of water vapour into the western part inducing a decrease in orographic precipitation here, and allows for an increased frequency of eastward transport events into the mountains at the eastern side increasing precipitation there. In addition, also associated with a reduced time-mean zonal flow, air masses have more time to cool when advected over the western part and are colder when arriving at the eastern part of Greenland, which induces increase in heating at the western part and cooling in the mountains in the east. The decrease in the time-mean flow is a general tendency of weather systems becoming more stationary^{32,33}.

The general increase in convergence over Greenland of both dry-static and latent energy by small-scale waves is consistent with an increase in divergence in particular over the Baffin Bay and Labrador Sea (Fig. 4b,d). This dipole pattern indicates an increase in cyclone activity in the Greenland area where cyclones take up energy and water vapour over the oceans and advect it inland. The pattern is consistent with projected changes

of an increase in cyclones propagating over Greenland³¹.

The sum of the contribution to the Greenland SMB change from the four transport components shows a similar pattern as the total SMB change although some differences are also apparent (Fig. 3c-d). Especially in the south-western part, where the strongest Greenland ice melt is encountered, changes in the atmospheric circulation have caused a negative SMB (Fig. 3b). As for the total SMB and the atmospheric mass flux, circulation-induced SMB shows a shift towards negative values beginning around year 2000. However, the circulation-induced SMB change appears smaller than the actual change, but comparison of actual magnitudes should be done with care due to the regression-based methods applied here for estimating the circulation-induced SMB. The circulation impact is based on regressions on the time scales of days to about a week. For longer lasting circulation anomalies such as circulation trends, the impact has more time to develop, for instance through positive feedbacks such as reduction of the surface albedo due to the melt. Hence when data are filtered to suppress variability on time scales below 90 days and 180 days, the circulation impact on the trend appears stronger (Fig. 3b).

According to ERA5, at the shore in the mountainous southeastern part of Greenland, the circulation has induced an overall positive SMB, whereas little total SMB change is found by the RACMO model. Hence positive SMB caused by the circulation changes may be compensated for by melting processes unrelated to the circulation. The circulation causes precipitation close to the shore and often at low elevation. Because of low elevation and the vicinity to the sea in a region where sea ice seldom forms, temperatures stay close to zero and the snow succeedingly melts. Hence the melting occurs due to local conditions that are independent of the atmospheric circulation.

The split of the energy transport by the atmospheric circulation into parts is important since these parts affect the SMB in different ways. If no separation into Rossby and cyclone waves is performed, the circulation impact on the SMB in southwestern Greenland would be less apparent (Fig. 3b,e), and if also the decomposition into dry-static and latent parts is disregarded, the SMB impact signal is essentially removed (Fig. 3b,f).

In summary, a shift in atmospheric heat and moisture transport over Greenland has significantly affected the Greenland ice-sheet melt. The Greenland ice-sheet surface-mass balance changed from a state of being in approximate balance into a state of melt at about year 2000, and therefore the melting appears not linearly coupled to global warming. However, the eastward atmospheric mass flux over Greenland, and the component of the SMB that is linearly linked to circulation changes based on regressions, both show a similar development as that of the Greenland surface-mass balance. It is likely that circulation changes are coupled to global warming^{32,33} although this is still under debate³⁴⁻³⁶. A decrease in eastward mass flow over southern Greenland is consistent with a general reduction in the Northern-Hemisphere meridional temperature gradient, weakening the thermal wind and hence the mid-latitude westerlies. The meridional temperature reduction is a well-established climate-change signal of Arctic temperature

amplification – the Arctic warming pace being larger than that of the rest of the hemisphere. It has been argued that the circulation changes may amplify extreme events and hereby increase severity of climate change^{32,33,37}. The results presented here, regarding circulation impact on the Greenland ice-sheet melt, provide an additional example that circulation changes can have large regional and global consequences, in this case as they lead to global sea-level rise.

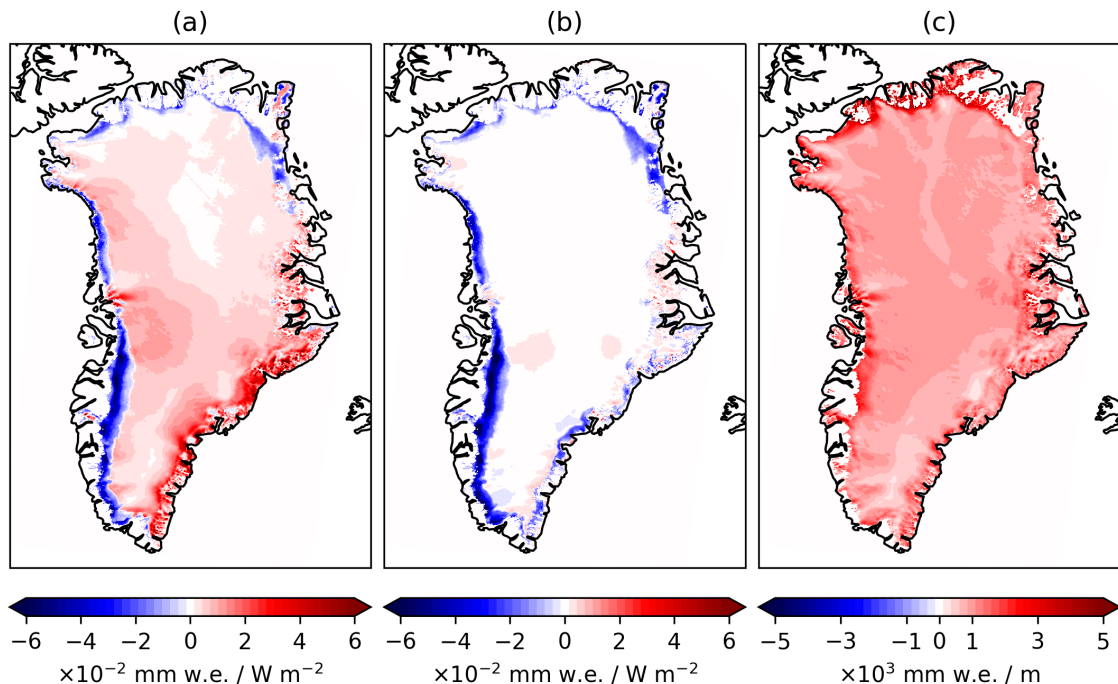


Figure 1: **Impact of the surface energy balance and precipitation on the surface-mass balance.** Regressions on SMB of the surface energy balance (a), the part of the surface energy balance shown is orthogonal to (decorrelated with) precipitation (b), and precipitation (c).

Methods

Atmosphere and wave decomposition

The atmospheric data are based on the ERA5 reanalysis³⁸. Classically the atmospheric energy transport may be decomposed into components of dry-static, $E = c_p T + gz + 1/2 \mathbf{v}^2$, and latent heat, $Q = Lq$, transports³⁹, where c_p is the heat capacity at constant pressure, T temperature, g gravitational acceleration, z geopotential heights, and $\mathbf{v} = (u, v)$ is the zonal and meridional velocity components. The dry-static part includes sensible heat, potential energy and – due to tradition – kinetic energy, whilst the latent part is associated with transport of moisture. Reanalysis data such as the ERA5 provide a mass-flux inconsistency⁴⁰, hence a mass-flux correction is applied at each time step to the wind fields⁴¹. The atmospheric heat transport may be further divided into waves through a Fourier decomposition^{27,42}. The transport is hereby split into synoptic and

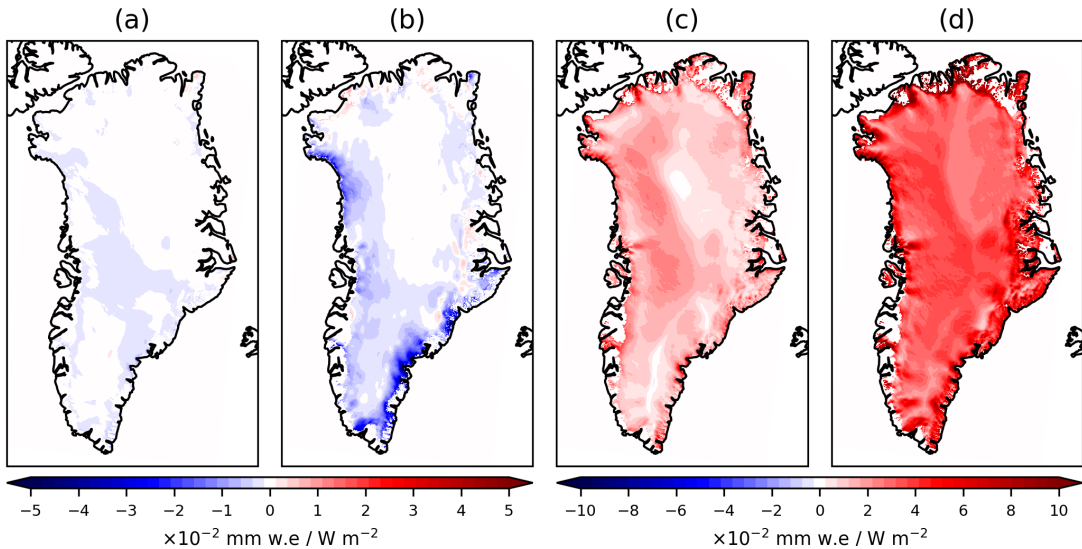


Figure 2: **Regression coefficients of surface mass balance regressed on energy transport convergence.** Regression coefficients are shown for the planetary scale dry-static transport (a), synoptic scale dry-static transport (b), planetary scale latent heat transport (c), and synoptic scale latent heat transport (d).

planetary scale contributions based on wavenumbers in the mass flux field²⁸. Planetary and synoptic scale systems are associated with different dynamical processes in the atmosphere. Planetary scale systems are typically Rossby waves, whilst synoptic systems include cyclones and meso-scale and other disturbances. For the dry-static component, the meridional transport decomposition into the two length scales yields:

$$vE_p(\phi, \lambda) = \int_0^{p_s} \left(\frac{a_0(\phi)}{2} + \sum_{n=1}^3 (a_n(\phi) \cos(2\pi n\lambda) + b_n(\phi) \sin(2\pi n\lambda)) \right) E \frac{dp}{g} \quad (1)$$

and

$$vE_s(\phi, \lambda) = \int_0^{p_s} \left(\sum_{n \geq 4} (a_n(\phi) \cos(2\pi n\lambda) + b_n(\phi) \sin(2\pi n\lambda)) \right) E \frac{dp}{g}, \quad (2)$$

respectively, where, ϕ and λ are latitude and longitude coordinates (in radians), p is pressure, and p_s is surface pressure. The factors $a_n(\phi)$ and $b_n(\phi)$ are the Fourier coefficients of the meridional winds. Similarly the zonal energy transport, $uE(\phi, \lambda)$, is decomposed using a Fourier decomposition of the zonal mass flux field. The latent energy transport is decomposed in a similar way. Based on previous studies⁴² the separation between large- and small-scale circulation is set between wavenumbers $n = 3$ and $n = 4$. In this study the zonal-mean flow given the wavenumber $n = 0$ component is considered together with large-scale components $n = 1-3$. In previous studies^{27,42} where only the meridional component of the energy transport is considered, the contribution of $n = 0$ is

small at high latitudes. However, when the zonal component is taken into account, as is done in this study, this component cannot be neglected. The convergences of dry-static and latent energy transport by Rossby waves yields:

$$E_p^{\text{conv}} = -\nabla \cdot (uE_p(\phi, \lambda), vE_p(\phi, \lambda)) \quad (3)$$

and

$$Q_p^{\text{conv}} = -\nabla \cdot (uQ_p(\phi, \lambda), vQ_p(\phi, \lambda),) \quad (4)$$

respectively, where E_p^{conv} is the dry-static energy convergence and Q_p^{conv} the latent heat convergence of Rossby waves. These are computed from the decomposed ERA5 energy transport fields on a 0.25° spatial and 6-hourly temporal resolution. The energy transport convergence fields are spatially smoothed to reduce noise.

Decorrelation

Large and small-scale circulation decomposed using the Fourier method Eq. 1 and 2 are temporally correlated. For instance, the large-scale circulation patterns may advect the flow patterns of small-scale systems. In this study the effect of the individual components of the convergence of energy transport on the SMB is examined, therefore it is necessary to remove the correlated parts of the transport components. The effect of large-scale and small-scale circulation is separated by decorrelating large-scale and small-scale circulation. The decorrelation is done by performing a linear regression of the small-scale circulation on the large-scale circulation. The regression corresponds to the part of the small-scale circulation that contributes to or "explain" the energy transport by the large-scale circulation:

$$\beta_p^s = \frac{\text{cov}(E_s^{\text{conv}}, E_p^{\text{conv}})}{\text{var}(E_p^{\text{conv}})}, \quad (5)$$

where β_p^s is the regression of small-scale convergence on large-scale convergence, E_s^{conv} the small-scale convergence, and E_p^{conv} is the large-scale convergence. The contribution of the large-scale convergence on the the small-scale is removed from the small-scale convergences by multiplying the regression coefficient (Eq. 5) with the large-scale convergences and subtracting from the small-scale:

$$E_{s||p}^{\text{conv}} = E_s^{\text{conv}} - \beta_p^s E_p^{\text{conv}}. \quad (6)$$

The decorrelations are performed similarly between dry-static energy and latent heat, and between surface energy and precipitation.

Surface mass balance

The surface mass balance fields in this study are output from the polar version of the Regional Atmospheric Climate Model (RACMO2)¹⁶. RACMO2 is run on a 5.5km spatial grid-resolution, and the output is statistically down-scaled to a 1km grid. RACMO2 is forced with ERA-Interim on the boundaries, and the surface mass balance is computed using a multi-layer snow module⁴³. The surface mass balance is defined as

$$SMB = PR - SU - EW - RU, \quad (7)$$

where PR is precipitation, SU sublimation, EW wind erosion, and RU is runoff. Liquid water mass from melt or rainfall may percolate through the firn layer, where it may be retained either through refreezing or capillary forces. The remaining part of the liquid water is runoff. The runoff, RU , consists of the melt water, ME , and rainfall, RA , from which the irreducible water, RZ , and refrozen water, CR , is subtracted:

$$RU = ME + RA - RZ - CR. \quad (8)$$

The runoff RU is equivalent to melting mentioned earlier in the paper. The total melt water available is dependent on the energy balance of the surface layer (SEB):

$$SEB = SW_{\text{net}} + LW_{\text{net}} + SHF + LHF + G_s, \quad (9)$$

where SW_{net} is the net shortwave radiation at the surface, LW_{net} the net longwave radiation at the surface, SHF the sensible heat flux, LHF latent heat flux, and G_s the sub-surface heat flux. The SEB and precipitation used in the regressions is computed from ERA5 as in Eq. 9, but without the subsurface heat fluxes, as they are small.

Regressions

Regressions of surface mass balance on components of energy transport convergence, surface-energy balance and precipitation are performed with daily data on the RACMO2 grid. Hence the transport convergences and other ERA5 fields are first regridded from the 0.25° ERA5 grid to the RACMO2 grid, using conservative remapping which conserve the fluxes of the remapped fields. The regression coefficients are computed similarly to the regressions used in the decorrelation process (Eq. 5).

Surface mass balance, energy transport convergence, and precipitation anomalies are all computed with respect to a climatology derived from the period 1979-2018. The climatologies are computed from detrended data, where, due to the non-linearity of the SMB trend, two linear trends for the periods before and after year 2000 are subtracted from the data. The climatologies are smoothed using a periodic 10-day running-mean filter to remove noise from the data.

Trends

The trends and circulation shifts are computed by subtracting the mean state of the period before year 2000 from that after. The division between periods is chosen at year 2000 due to the accelerating mass loss starting approximately in 2000. The impact of atmospheric circulation change on SMB is achieved by multiplying trends in a transport convergence component with the associated regression coefficient. Hereby the the part of the SMB trend "explained" by a given energy transport component is obtained. For the dry-static planetary component the SMB trend yields:

$$\delta SMB^{E_p^{\text{conv}}} = \beta_{E_p^{\text{conv}}}^{SMB} \delta E_p^{\text{conv}}. \quad (10)$$

The statistical significance of the trends is tested by performing a Monte-Carlo sampling test. The statistical significance of the mass-flux trend is computed using a 4000-iteration

two-sided test, and the energy transport convergence trends using 2000-iteration two-sided test. To account for the auto-correlation of the time-series the random sampling is performed by making random permutations of the years. The time evolution of the surface mass balance, zonal mass flux, and the energy transport convergence in the south-west Greenland (Fig. 3b) are computed by applying a 10-year running mean filter on data summed over this region.

Small-scale versus Rossby regressions

Figure 2 shows in general larger regressions for small-scale waves than for Rossby waves, which appears in contrast to earlier studies providing the effect of the two types of waves on the entire Arctic^{27,28}. However in the latter studies, the transport components at 70° N are regressed on Arctic fields such as temperature and radiation as a function of latitude and longitude. In the Greenland study presented here, regressions are based on point-to-point regressions where transport components and SMB are regressed at each latitude and longitude grid point. Hence for the Arctic studies regressions indicate simultaneous effect over the Arctic, whereas for the Greenland study, it is the direct effect of cyclones on a given grid point that is captured by the regressions. Is the SMB regressed on transport convergences averaged over Greenland (not shown), the simultaneous effect on SMB over Greenland of Rossby wave compared to small-scale waves is larger for the dry-static part, but the opposite is the case for the latent part although the difference in regression between small-scale waves and Rossby waves is smaller than that based on point-to-point regressions shown in Fig. 2c-d.

Acknowledgments

We are grateful to Brice Noël for providing the SMB data from RACMO2, and the ERA5 group for providing the reanalysis data. The work was funded by the Norwegian Research Council under the project "The role of the atmospheric energy transport in recent Arctic climate change" (280727). We are also grateful for the computational resource provided by NOTUR under the projects NS9063k and NN3948k.

References

- ¹ Yang H, Krebs-Kanzow U, Kleiner T, Sidorenko D, Rodehacke CB, Shi X, et al. (2022) Impact of paleoclimate on present and future evolution of the Greenland Ice Sheet. *PLoS ONE* **17**(1): e0259816. <https://doi.org/10.1371/journal.pone.0259816>
- ² Katsman et al. Exploring high-end scenarios for local sea level rise to develop flood protection strategies for a low-lying delta—the Netherlands as an example *Climate Change*, **109** 617–645 (2011). <https://doi.org/10.1007/s10584-011-0037-5>
- ³ Mouginit, J. et al. Forty-six years of Greenland Ice Sheet mass balance from 1972 to 2018. *Proceedings of the National Academy of Sciences* **116**, 9239-9244 (2019). <https://doi.org/10.1073/pnas.1904242116>

- ⁴ Bevis, M. et al. Accelerating changes in ice mass within Greenland, and the ice sheet’s sensitivity to atmospheric forcing. *Proceedings of the National Academy of Sciences* **116**, 1934–1939 (2019). <https://doi.org/10.1073/pnas.1806562116>
- ⁵ The IMBIE Team. Mass balance of the Greenland Ice Sheet from 1992 to 2018. *Nature* **579**, 233–239 (2020). <https://doi.org/10.1038/s41586-019-1855-2>
- ⁶ IPCC, 2021: Climate Change 2021: The Physical Science Basis. Contribution of Working Group I to the Sixth Assessment Report of the Intergovernmental Panel on Climate Change [Masson-Delmotte, V., P. Zhai, A. Pirani, S.L. Connors, C. Péan, S. Berger, N. Caud, Y. Chen, L. Goldfarb, M.I. Gomis, M. Huang, K. Leitzell, E. Lonnoy, J.B.R. Matthews, T.K. Maycock, T. Waterfield, O. Yelekçi, R. Yu, and B. Zhou (eds.)]. Cambridge University Press. In Press.
- ⁷ Lamarche-Gagnon, G., et al. Greenland melt drives continuous export of methane from the ice-sheet bed. *Nature* **565**, 73–77 (2019). <https://doi.org/10.1038/s41586-018-0800-0>
- ⁸ van Kampenhout, L., et al. Present-day Greenland ice sheet climate and surface mass balance in CESM2. *Journal of Geophysical Research; Earth Surface*, **125**, e2019JF005318 (2020). <https://doi.org/10.1029/2019JF005318>.
- ⁹ King et al. Dynamic ice loss from the Greenland Ice Sheet driven by sustained glacier retreat *Commun. Earth and Environ.*, **1** (2020). <https://doi.org/10.1038/s43247-020-0001-2>
- ¹⁰ Choi, Y., et al. Ice dynamics will remain a primary driver of Greenland ice sheet mass loss over the next century. *Commun Earth Environ* **2**, 26 (2021). <https://doi.org/10.1038/s43247-021-00092-z>.
- ¹¹ Hanna, E., Navarro, F., Pattyn, F. et al. Ice-sheet mass balance and climate-change. *Nature* **498**, 51–59 (2013). <https://doi.org/10.1038/nature12238>
- ¹² Hanna, E., et al. Mass balance of the ice sheets and glaciers - Progress since AR5 and challenges. *Earth-Science Reviews*, **201** 102976 (2020). <https://doi.org/10.1016/j.earscirev.2019.102976>.
- ¹³ Hanna, E., et al. Greenland surface air temperature changes from 1981 to 2019 and implications for ice-sheet melt and mass-balance change. *Int J Climatol.*, **41** (Suppl. 1) E1336– E1352 (2021). <https://doi.org/10.1002/joc.6771>.
- ¹⁴ Oltmanns, M., Straneo, F., and Tedesco, M.: Increased Greenland melt triggered by large-scale, year-round cyclonic moisture intrusions, *The Cryosphere*, **13**, 815–825, (2019). <https://doi.org/10.5194/tc-13-815-2019>
- ¹⁵ Izeboud, M., et al. The spatiotemporal variability of cloud radiative effects on the Greenland ice sheet surface-mass balance. *Geophysical Research Letters*, **47**, e2020GL087315 (2020). <https://doi.org/10.1029/2020GL087315>

- ¹⁶ Noël, B. et al. Modelling the climate and surface-mass balance of polar ice sheets using RACMO2 - Part 1: Greenland (1958–2016) *The Cryosphere* **12**, 811–831 (2018). <https://doi.org/10.5194/tc-12-811-2018>
- ¹⁷ Barrett, BS, Henderson, GR, McDonnell, E, Henry, M, Mote, T. Extreme Greenland blocking and high-latitude moisture transport. *Atmos Sci Lett*, **e1002** (2020). <https://doi.org/10.1002/asl.1002>
- ¹⁸ Mattingly, K. S., et al. Strong Summer Atmospheric Rivers Trigger Greenland Ice Sheet Melt through Spatially Varying Surface Energy Balance and Cloud Regimes. *J. Climate*, **33**, 6809–6832 (2020). <https://doi.org/10.1175/JCLI-D-19-0835.1>
- ¹⁹ Hanna, E., et al. Atmospheric and oceanic climate forcing of the exceptional Greenland ice sheet surface melt in summer 2012. *Int. J. Climatol.*, **34**, 1022-1037 (2014). <https://doi.org/10.1002/joc.3743>.
- ²⁰ Fausto, R. S., et al. The implication of nonradiative energy fluxes dominating Greenland ice sheet exceptional ablation area surface melt in 2012, *Geophys. Res. Lett.*, **43**, 2649–2658 (2016). <https://doi.org/10.1002/2016GL067720>
- ²¹ Mattingly, K. S., Mote, T., Fettweis, X. Atmospheric River impacts on Greenland ice sheet surface mass balance. *Journal of Geophysical research*, **123**, 8538–8560 (2018). <https://doi.org/10.1029/2018JD028714>.
- ²² Sundal, A., Shepherd, A., Nienow, P. et al. Melt-induced speed-up of Greenland ice sheet offset by efficient subglacial drainage. *Nature* **469**, 521–524 (2011). <https://doi.org/10.1038/nature09740>
- ²³ Nygård, Tiina, Tuomas Naakka, and Timo Vihma. Horizontal Moisture Transport Dominates the Regional Moistening Patterns in the Arctic. *Journal of Climate* **33.16**, 6793-6807 (2020). <https://doi.org/10.1175/JCLI-D-19-0891.1>.
- ²⁴ Sherman, P., et al. Historical and future roles of internal atmospheric variability in modulating summertime Greenland ice sheet melt. *Geophysical Research Letters*, **47**, e2019GL086913 (2020). <https://doi.org/10.1029/2019GL086913>.
- ²⁵ Fettweis, X., et al. Brief communication "Important role of the mid-tropospheric atmospheric circulation in the recent surface melt increase over the Greenland ice sheet". *The Cryosphere*, **7**, 241–248 (2013). <https://doi.org/10.5194/tc-7-241-2013>.
- ²⁶ van den Broeke, M., et al. Greenland Ice Sheet Surface Mass Loss: Recent Developments in Observation and Modeling. *Curr Clim Change Rep* **3**, 345–356 (2017). <https://doi.org/10.1007/s40641-017-0084-8>.
- ²⁷ Graverson, R.G. and Burtu, M. Arctic amplification enhanced by latent energy transport of atmospheric planetary waves. *Q.J.R. Meteorol. Soc.*, **142** 2046-2054 (2016). <https://doi.org/10.1002/qj.2802>

- ²⁸ Rydsaa, JH, Graversen, RG, Heiskanen, TIH, Stoll, PJ. Changes in atmospheric latent energy transport into the Arctic: Planetary versus synoptic scales. *Q J R Meteorol Soc.* **147**: 2281– 2292 (2021). <https://doi.org/10.1002/qj.4022>
- ²⁹ Baggett, C., & Lee, S. Arctic Warming Induced by Tropically Forced Tapping of Available Potential Energy and the Role of the Planetary-Scale Waves, *Journal of the Atmospheric Sciences*, **72**(4), 1562-1568. (2015) Retrieved Feb 11, 2022, from <https://journals.ametsoc.org/view/journals/atsc/72/4/jas-d-14-0334.1.xml>
- ³⁰ Graversen, R.G., Mauritsen, T., Drijfhout, S. et al. Warm winds from the Pacific caused extensive Arctic sea-ice melt in summer 2007. *Clim Dyn* **36**, 2103–2112 (2011). <https://doi.org/10.1007/s00382-010-0809-z>
- ³¹ Schuenemann, K. C., and Cassano, J.J. Changes in synoptic weather patterns and Greenland precipitation in the 20th and 21st centuries: 2. Analysis of 21st century atmospheric changes using self-organizing maps. *J. Geophys. Res.*, **115**, D05108 (2010). <https://doi.org/10.1029/2009JD011706U>
- ³² Francis, J. A., and Vavrus, S. J., Evidence linking Arctic amplification to extreme weather in mid-latitudes, *Geophys. Res. Lett.*, **39**, L06801, (2012). <https://doi.org/10.1029/2012GL051000>.
- ³³ Kornhuber, K., & Tamarin-Brodsky, T. Future changes in Northern Hemisphere summer weather persistence linked to projected Arctic warming. *Geophysical Research Letters*, **48**, e2020GL091603 (2021). <https://doi.org/10.1029/2020GL091603>
- ³⁴ Barnes, E. A., & Screen, J. A. The impact of Arctic warming on the midlatitude jet-stream: Can it? Has it? Will it?. *Wiley Interdisciplinary Reviews: Climate Change*, **6**(3), 277-286 (2015). <https://doi.org/10.1002/wcc.337>
- ³⁵ Huguenin, M. F., Fischer, E. M., Kotlarski, S., Scherrer, S. C., Schwierz, C., & Knutti, R. Lack of change in the projected frequency and persistence of atmospheric circulation types over Central Europe. *Geophysical Research Letters*, **47** (2020). <https://doi.org/10.1029/2019GL086132>
- ³⁶ Cohen, J., Pfeiffer, K. & Francis, J.A. Warm Arctic episodes linked with increased frequency of extreme winter weather in the United States. *Nat Commun* **9**, 869 (2018). <https://doi.org/10.1038/s41467-018-02992-9>
- ³⁷ White, R. H., Kornhuber, K., Martius, O., & Wirth, V. From Atmospheric Waves to Heatwaves: A Waveguide Perspective for Understanding and Predicting Concurrent, Persistent and Extreme Extratropical Weather, *Bulletin of the American Meteorological Society* (2021) (published online ahead of print 2021). Retrieved Feb 25, 2022, from <https://journals.ametsoc.org/view/journals/bams/aop/BAMS-D-21-0170.1/BAMS-D-21-0170.1.xml>
- ³⁸ Hersbach, H, Bell, B, Berrisford, P, et al. The ERA5 global reanalysis. *Q J R Meteorol Soc.*, **146** 1999– 2049 (2020). <https://doi.org/10.1002/qj.3803>

- ³⁹ Oort AH, Peixóto JP. Global Angular Momentum and Energy Balance Requirements from Observations, *Advances in Geophysics* **25**. Academic Press: Cambridge, MA (1983). [https://doi.org/10.1016/S0065-2687\(08\)60177-6](https://doi.org/10.1016/S0065-2687(08)60177-6)
- ⁴⁰ Trenberth, K. E. Climate Diagnostics from Global Analyses: Conservation of Mass in ECMWF Analyses, *Journal of Climate*, **4**(7), 707-722 (1991). [https://doi.org/10.1175/1520-0442\(1991\)004%3C0:707:CDGAC%3E2.0.CO;2](https://doi.org/10.1175/1520-0442(1991)004%3C0:707:CDGAC%3E2.0.CO;2)
- ⁴¹ Graverson, R., Mauritsen, T., Tjernström, M. et al. Vertical structure of recent Arctic warming. *Nature* **451**, 53–56 (2008). <https://doi.org/10.1038/nature06502>
- ⁴² Heiskanen, T, Graverson, RG, Rydsaa, JH, Isachsen, PE. Comparing wavelet and Fourier perspectives on the decomposition of meridional energy transport into synoptic and planetary components. *Q J R Meteorol Soc.*, **146** 2717– 2730 (2020). <https://doi.org/10.1002/qj.3813>
- ⁴³ Ettrema, J., van den Broeke, M. R., van Meijgaard, E., van de Berg, W. J., Box, J. E., and Steffen, K.: Climate of the Greenland ice sheet using a high-resolution climate model – Part 1: Evaluation, *The Cryosphere*, **4**, 511–527, (2010). <https://doi.org/10.5194/tc-4-511-2010>

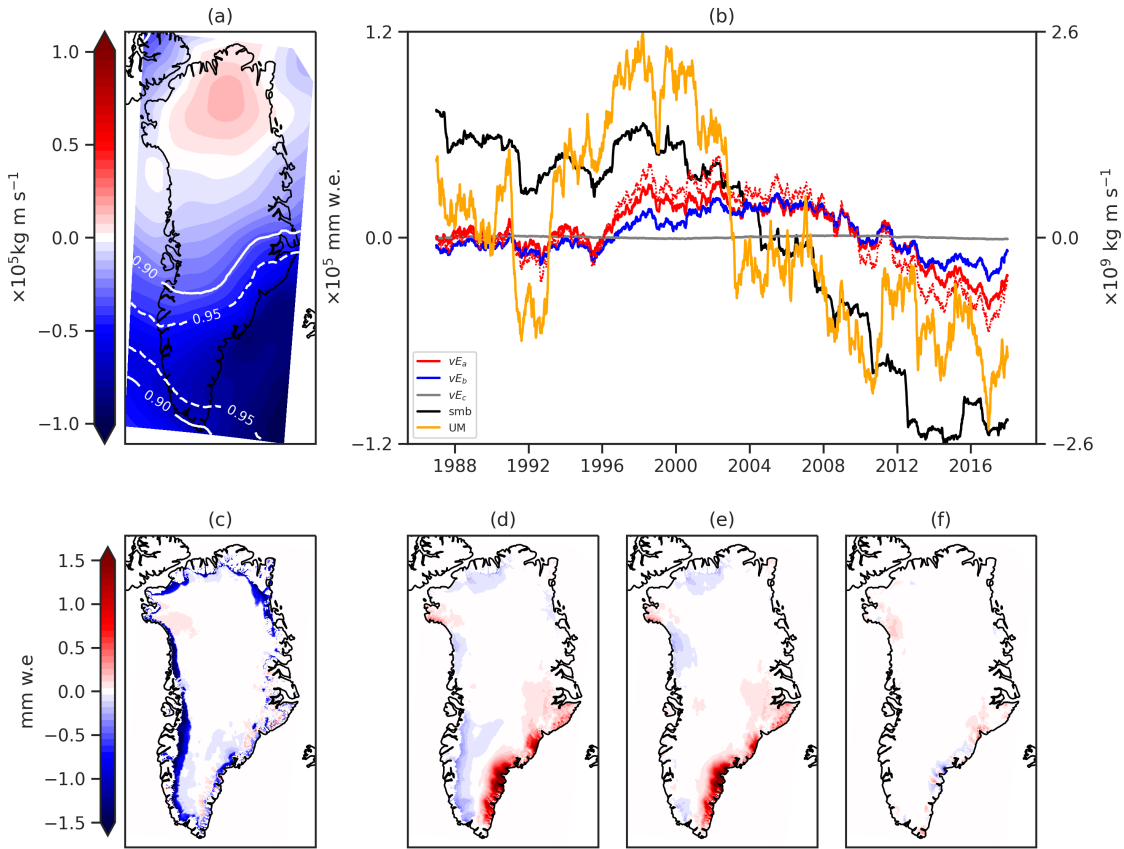


Figure 3: **Trends of surface mass balance, zonal mass flux, and energy transport components converted to surface mass balance.** Panel (a) shows the trend in zonal mass flux as the difference between the mean over the years 2000-2018 and 1979-2000. The contour lines denote the statistical significance of the trend. The line-plots (b) show time-series anomalies, relative to a climatology, of surface-mass balance, zonal mass flux, and surface mass balance due to energy transport convergence components in the south west region of Greenland. UM denotes the zonal mass flux, smb surface mass balance, vE_a the energy transport convergence converted to surface mass balance based of a decomposition into dry-static, latent heat, and length scales, vE_b the energy transport converted to surface mass balance based of only a decomposition into dry-static and latent heat, and vE_c the energy transport component converted to surface mass balance based of the total energy transport. Panel (c) shows the trend of surface-mass balance as the difference between the mean over the years 2000-2018 and 1979-2000. Panels (d)-(f) show the energy transport trends converted to surface mass balance for the total energy transport (f), the energy transport decomposed into latent heat and dry-static energy (e), and the energy transport decomposed both into latent heat and dry-static energy and length scales (d).

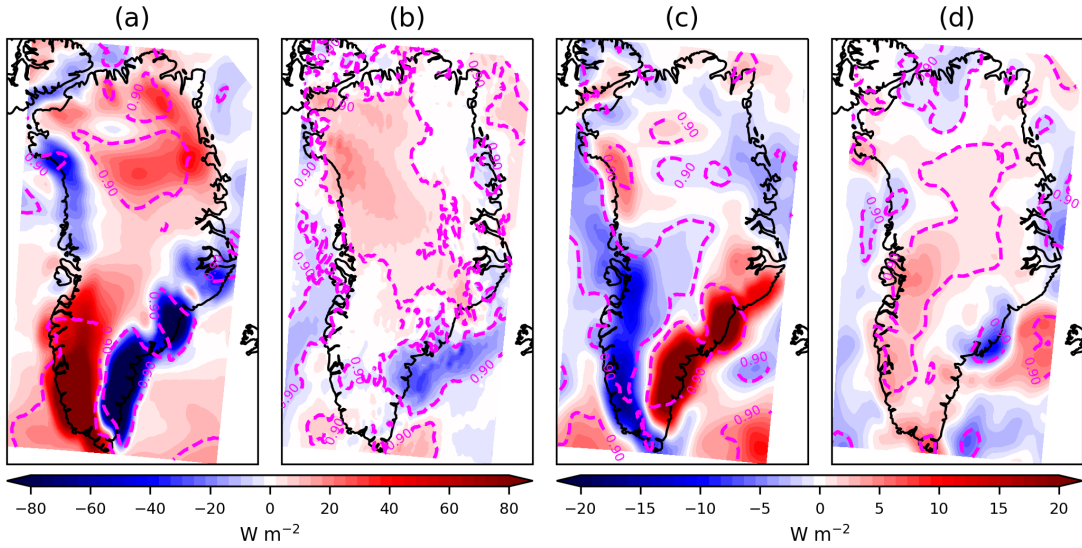


Figure 4: **Trends of convergence of dry-static and latent heat transport.** The trends are computed by taking the difference of the means of the energy transport components after and before year 2000. The ordering of the plots are as in Fig. 2. The contour lines denote the statistical significance of the trends based on a monte-carlo sampling test.

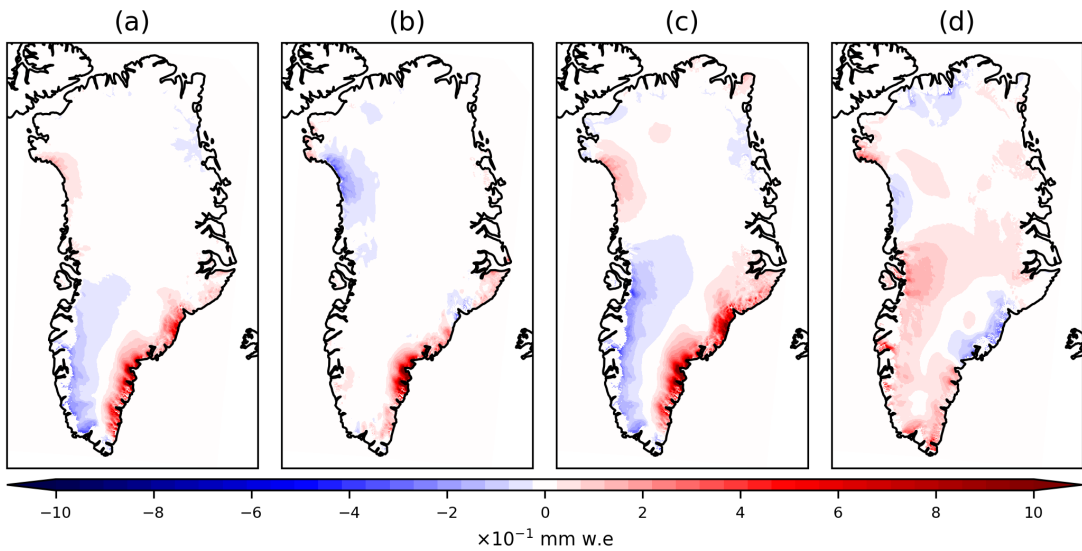


Figure 5: **Planetary and synoptic energy transport convergence trends converted to surface mass balance.** The energy transport convergence trends are converted to surface mass balance by multiplying with the regressions coefficients for the respective scales. The ordering of the trends converted to surface mass balance are as in Fig. 2.

/9

Paper IV

Heiskanen, Tuomas, Rune G. Graversen, Richard Bintanja, and Camiel Severijns (in review 2022b). “Length-scale decomposition of energy transport using machine learning techniques.” In: Submitted for review.

Length-scale decomposition of energy transport using machine learning techniques

Tuomas Heiskanen¹, Rune Graversen^{1,2}, Richard Bintanja³,
and Camiel Severijns³

¹*Department of Physics and Technology, UiT The Arctic University of Norway, Tromsø, Norway*

²*Norwegian Meteorological Institute, Tromsø, Norway*

³*Royal Netherlands Meteorological Institute (KNMI), De Bilt, Netherlands*

Correspondence

T. Heiskanen, Department of Physics and Technology, University of Tromsø, Postboks 6050, Langnes, 9037 Tromsø, Norway.

Email: tuomas.i.heiskanen@uit.no

Funding information

Research Council of Norway (NFR), Grant/Award Number: 280727

Abstract

In this study the applicability of using machine learning to estimate climate variables is investigated. Machine-learning models are applied to decompose atmospheric latent heat transport into contributions by waves. Classically the length-scale decomposition of atmospheric latent heat transport is a data and computer-intensive process. Here a machine-learning model ensemble is used to estimate the latent heat transport, which is a computationally extremely efficient approach compared to the classical methods. The machine-learning models are trained on ERA5 data, and evaluated both on ERA5 data and output from the climate model EC-Earth. Both the daily variability and the mean of the length-scale-decomposed energy transport are well captured by the machine-learning ensemble. Additionally, the machine-learning ensemble is capable of capturing trends in the energy transport in future forcing scenarios. Once trained, the data requirement for the machine-learning model is small compared to the classical method. Hence, machine-learning-based estimates may be used to compute the length-scale decomposition of energy transport from data sets where variables necessary for the classical computation are lacking, such as from model output included in the CMIP archives.

Introduction

Atmospheric motions transport energy poleward from the warm, moist, and insolation-rich tropics. The energy is transported by atmospheric circulation systems on several length and time scales (Trenberth and Caron, 2001, Graversen and Burtu, 2016, Heiskanen et al., 2020). Energy

transport by planetary and synoptic-scale systems affects Arctic climate differently; planetary-scale waves impact Arctic temperatures considerably more than waves on the synoptic scales (Baggett and Lee, 2015, Graversen and Burtu, 2016, Heiskanen et al., 2020, Rydsaa et al., 2021). There are multiple ways to decompose the meridional energy transport based on scales. Both the Fourier-based approach by Graversen and Burtu (2016) and the wavelet-based approach by Heiskanen et al. (2020) are heavily data intensive. For high accuracy, computing the decomposed energy transport following either Graversen and Burtu (2016) or Heiskanen et al. (2020) demands data on a 6-hourly temporal resolution and all vertical layers in the atmosphere. This requires large computing and storage facilities, and the required data are normally available only from the reanalysis archives. In order to circumvent these computer and data challenges, applying data-driven machine learning approaches appears as an attractive pathway forward.

The dry-static energy transport in a warmer climate is projected to decrease due to a smaller temperature gradient between low latitudes and the poles (Hwang et al., 2011, Koenigk et al., 2013). However, the meridional latent heat transport is projected to increase in a warmer climate due to enhanced moisture content in the atmosphere. Previous studies indicate a shift from synoptic to planetary scales of the latent heat transport in the mid-latitudes, especially for extreme transport events (Rydsaa et al., 2021), and that the planetary latent-heat transport increase in future projections (Graversen and Burtu, 2016). These future projections of energy transport by scales are based on a climate model run with the EC-Earth model (Graversen and Burtu, 2016). Recently a new ensemble of future projections with that model has become available. Based on that ensemble, the energy transport decomposed into wave contributions has been computed. However, the climate models vary in their responses and changes of the atmospheric circulation due to given future forcing scenarios (Shepherd, 2014). Hence it is important to assess the differences and similarities between the models when it comes to meridional energy transport as this quantity affects the climate response, especially regional responses.

Here we explore an alternative approach to achieve the length-scale decomposition of meridional energy transport using deep learning. The idea is that using a deep-learning model as a function approximator, we may extract enough information from the state of the atmosphere on a single layer to estimate the meridional energy transport separated into wave contributions. Thus the goal is to make a deep-learning model that requires considerably less data compared to the exact computations. The coupled model inter comparison project (CMIP) archives are a large collection of climate model experiments. CMIP5 (Taylor et al., 2012) provides experiments used in the IPCC AR5 report on climate changes, whilst the most recent archive CMIP6 (Eyring et al., 2016) includes models used for the AR6 report. These archives consist of standardized climate-model experiments, for a great number of models. Since the atmospheric state on a single pressure level and daily temporal resolution is in many cases archived in the CMIP5 and CMIP6 model archives, we may use the machine-learning approach to estimate the decomposed meridional energy transport from previously executed climate-model experiments. Accomplishing this yields a useful tool to examine future circulation changes and their effect on for instance Arctic climate.

Machine learning is widely used in technological applications, from object identification to natural language processing. Although the first artificial neural networks were developed decades ago, the applicability of machine learning has been revolutionized with the increase in computational power. For example, deep-learning models are successful at modelling high dimensional data in computer vision, natural language processing, autonomous cars, and so forth. Artificial neural networks are considered general function approximators; this implies that neural networks may be used to approximate any function mapping a dataset to a desired output (Ferrari and Stengel, 2005, Jordan and Mitchell, 2015). In climate sciences large quantities of data are stored in model

and reanalysis archives. Previous studies, e.g. Scher and Messori (2019), Weyn et al. (2019, 2021) and Rasp and Thuerey (2021), have shown the feasibility of deep learning in data-driven medium-range weather forecasts. Here we suggest machine learning techniques, which may be applied in order to derive important climate variables from climate-model experiments, that otherwise would require output and storage of a comprehensive amount of data.

Machine-learning models learn physical relations from data. These relations are not explicitly determined when designing the machine-learning model. Hence, such a model may learn previously undiscovered relationships between climate variables, or at least useful approximations of actual physical relations. The training process of a machine learning model requires a large amount of data (Jordan and Mitchell, 2015). However, when training is complete and the machine-learning model is used for estimation or prediction, the model requires only a limited data amounts. These models may thus be able to approximate physical quantities using far less data than exact, conventional computations.

The conventional methods for separating the transport into contributions by large-scale (planetary) and small scale (synoptic) systems were developed in earlier studies, e.g. Graversen and Burtu (2016) and Heiskanen et al. (2020). These methods require information about the atmospheric state throughout the vertical and horizontal extent of the atmosphere at high temporal resolution, preferably being 6-hourly. Typically the required data are only available from reanalysis data sets or during online runs of climate models. Thus, the decomposition's are mostly applicable to reanalysis data sets and climate model experiments where the computations are planned and implemented in the model code at before hand. Although applicable to reanalysis and model data, the computation of the decomposition is time consuming due to the large amount of data required. The classical computations are thus usually inconvenient based on reanalysis data, but often impossible based on data from model archives.

Hence, here we suggest to apply a deep-learning model to compute the energy transport separated into waves based on the future projections available in the CMIP archives. The estimation of the transport by waves in the archived model runs opens for new possibilities for validation of previous hypotheses, performing comparisons of the climate models with regards circulation to changes, and estimating the range of uncertainty in future changes of the meridional energy transport by waves.

Methods and data

Using ERA5 (Hersbach et al., 2020) and the recently computed EC-earth ensembles as training and validation data we tune an artificial neural network to perform the desired decomposition of the latent heat transport into contributions by waves on several length scales. The meridional latent heat transport is defined as

$$vQ(\phi) = \oint \int_0^{p_s} vLq \frac{dp}{g} dx, \quad (1)$$

where v is meridional wind, L latent heat of condensation, q specific humidity, p atmospheric pressure, and g is the gravitational acceleration. The meridional latent heat transport (Eq. 1) is decomposed into contributions by different length scales following the approach of Graversen and Burtu (2016)

$$vQ(\phi) = d \sum_{i=1}^N \left[\frac{a_{0,i}^v a_{0,i}^q}{4} + \frac{1}{2} \sum_{n=1}^{\infty} (a_{n,i}^v a_{n,i}^q + b_{n,i}^v b_{n,i}^q) \right], \quad (2)$$

where the $a_{n,i}^v$ and $b_{n,i}^v$ are Fourier coefficients of the massflux, $a_{n,i}^q$ and $b_{n,i}^q$ Fourier coefficients of the latent heat, $d = 2\pi a \cos(\phi)$ the circumference at latitude ϕ , n the wavenumber of the Fourier coefficients, and i denotes the discretized vertical level of a total of N levels. The transport expressed in Eq. 2 provides the complete latent heat transport. The transport is fully decomposed by splitting the wavenumber sum into length-scale-based components. Following Heiskanen et al. (2020) the transport (Eq. 2) is decomposed into meridional transport ($n = 0$), planetary-scale transport ($n = 1-3$), and synoptic transport ($n \geq 4$). The separation between planetary and synoptic-scale applied here is different from that in Graversen and Burtu (2016), where the separation was between wavenumbers $n = 5$ and $n = 6$. Heiskanen et al. (2020) argues that the separation between wavenumbers $n = 3$ and $n = 4$ is more appropriate than that in Graversen and Burtu (2016).

The latent energy transport is computed from the ERA5 reanalysis data on a $0.25 \times 0.25^\circ$ horizontal and 6 hourly temporal resolution, for the time period 1979-2018. The reanalysis data do not conserve mass; hence to obtain a realistic mass flux associated with the energy transport, a barotropic wind correction is applied (Trenberth, 1991, Graversen, 2006). In the vertical direction, the ERA5 reanalysis includes 137 layers, over which the transport is integrated in order to achieve the total meridional energy transport in the atmosphere (Graversen and Burtu, 2016, Hersbach et al., 2020).

Additionally we use data from an ensemble of five climate-model runs performed for the time period 1950-2100. For this we use the global, coupled climate model EC-Earth (Hazeleger et al., 2010, 2012), which includes the following components: atmosphere, ECMWF's Integrated Forecast System (IFS), resolution T159L62; ocean, NEMO V2, resolution 1 deg.; sea ice, LIM2, resolution 1 deg; with all of these components coupled through the OASIS3 coupler. General characteristics of EC-Earth in terms of a more detailed description of its components, as well as its performance and global climate sensitivity are given by Hazeleger et al. (2010) and Hazeleger et al. (2012). The performance of EC-Earth of the present-day climate is good, even though parts of the sub Arctic show too high winter temperatures, especially in the continental regions of Siberia and Canada. The energy transport and its length-scale decomposition is computed following (Graversen and Burtu, 2016).

As input to the machine-learning model we need a set of atmospheric fields. These are extracted from the repositories of ERA5 and the EC-Earth model runs. Multiple fields appear relevant to use as inputs to the model. However, we try to limit the amount of input to as few fields as are necessary. The fields used as input for the deep-learning model are specific humidity and geopotential height at 850 hPa. The specific humidity is the actual quantity which is transported, and the geopotential height determines the flow structure of the atmosphere, and provides information of the temperature. The 850 hPa level is chosen as it is usually sufficiently close to the ground, where most of the latent heat is transported. The model is trained using input fields on a daily resolution for the region north of 30°N . The spatial region is selected due to limited data availability from the EC-Earth runs on a daily resolution.

Regressions of temperature on length-scale-decomposed latent heat transport is computed from daily anomalies with respect to a monthly climatology computed for the period 1979-2018. The monthly climatology is computed both for the energy transports and temperatures. The daily values are then smoothed using a seven-day running-mean filter before computing the regressions.

To limit the arbitrariness of choices the network structure is based on well-established and carefully investigated designs. The chosen deep-learning model is a deep convolutional neural network following the resnet18 structure (He et al., 2016). The structure is based on residual blocks which

consist of two convolution blocks, and a skip connection of the input to the residual block to the output

$$y_i = f(x_i) + x_i, \quad (3)$$

where y_i is the output of the residual block, $f(x_i)$ the output of the convolutions, x_i the original input, and i is a block index. The resnet18 design is based on eighteen residual blocks (Eq. 3).

Similar architectures are used for data-driven weather forecasting (Rasp and Thuerey, 2021, Weyn et al., 2021). The resnet18 model is trained from randomly initialized weights. The objective of training is to minimize a cost function. The cost function quantifies the difference between the output of the machine learning model and the target value. The difference between the model output and the actual value is called loss. The main goal of the training phase is to find the global minima of the cost function, which produces the smallest possible loss. However, this is not always where the training process leads. Hence we train multiple machine learning models, as in e.g. Weyn et al. (2021), from the same training data, and use a multi-model mean as the estimated energy transport. The multi-model ensemble consists of a total of seven resnet18 models, which is an arbitrarily chosen number yet large enough to explore the range of uncertainty. The approach of training multiple resnet18s on the data yields the possibility to estimate uncertainty in the estimated energy transport decomposition.

The resnet18 models are trained on normalized ERA5 data. The training data are split temporally into validation, training and test datasets. The training and validation datasets are selected by randomly splitting the data in the time period 1984-2013. The data are split such that 75% of the data is in the training set and the remaining 25% in the validation set. Time periods 1979-1983 and 2014-2018 are used as the test periods. The test data are split temporarily from the training and validation sets to minimize the effect of temporal auto correlations between the testing and training data. A random split would lead to data leakage from the training set into the test set, since the timeseries for the atmospheric variables have an autocorrelation greater than one day. By splitting at a specific year there will still be some data leakage at the start of the first year of the test dataset. However, it will mostly be limited to the first few days of the years closest to the splits between the training and test datasets. The test dataset is chosen as the first and last five years of the considered time period. Additionally, to test the ERA5 trained model, the EC-Earth dataset is used for further testing.

Seven resnet18 models are trained for 60 epochs each. One epoch corresponds to running through all the training data once. Each of the models are trained with the same training data. The models are trained using a stochastic gradient descent algorithm (Amari, 1993) with a root-mean-squared error loss function. The stochastic gradient descent is performed with a learning rate of $lr = 0.9$ and a momentum of $m = 0.9$, and a batch size of 40 data points per mini-batch. The learning rate determines how strongly each mini-batch is affecting the weights of the network; essentially how fast the weights are moved towards the minima of the cost function. The momentum determines how strongly gradients computed in previous passes of the data are affecting the training at the current pass. The loss of the validation dataset converges after approximately 60 epochs to a value of ~ 0.16 (Fig. 1). Since the loss of the validation data does not decrease significantly after this point the training process is stopped at 60 epochs to prevent an overfitting of the model to the training data.

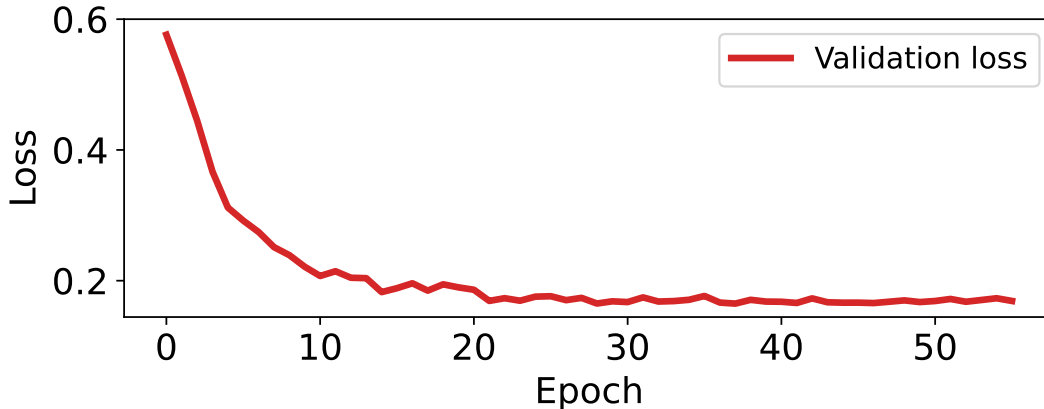


Figure 1: Validation loss of one of the resnet18 models trained to decompose the latent heat transport into length scales.

Results

After training, the model ensemble is now tested on a test period of the ERA5 data, where the resnet18 ensemble is compared to the classical computations. All components of the meridional latent heat transport of the resnet18 ensemble mean coincide well with the traditionally computed energy transport (Fig. 2). However, the trend between the first five and last five years of the test data at low latitudes is not captured as well as elsewhere by the resnet18 ensemble (Fig. 2c). At high latitudes the trends are captured well, which is apparent as the observed trend stays within the ensemble spread. A possible explanation for the reduced performance at low latitudes is that the latent heat transport across a latitude circle is dependent on the weather at adjacent latitudes. Hence, when estimating the transport using the resnet18 ensemble that is trained only on data north of 30° the model ensemble is poorer in the vicinity of low latitudes boundary than at high latitudes. It is important to note that the trend of the latent heat transport within the ERA5 period is small and not statistically significant (Rydsaa et al., 2021). However, it is interesting that although the trends are not large enough for being statistically significant, the resnet18 ensemble is capable of capturing small changes of the latent heat transport.

In the EC-Earth ensemble we have both the required input fields for the ERA5-trained resnet18 models, and an exact computation of the length-scale decomposed latent heat transport. Hence, we may evaluate the performance of the resnet18 models directly against the actual values of the length-scale-decomposed latent heat transport (Fig. 3). Although some minor differences are apparent, the computed latent heat transport is mostly within the ensemble spread of the resnet18 ensemble. The resnet18 model ensemble has some performance problems at low latitudes, which, as mentioned above, may be explained by the lack of input data at latitudes south of 30°N . Note that the test of the resnet18 ensemble is done outside the training period of 1983-2014. The first ten years in Fig. 3 is 1950-1959 of the simulation, whilst the last ten years are 2091-2100. Both of these periods correspond to different climate states than that in the training period. Capturing of trends and transport in different climate states constitute an important test for the resnet18 ensemble. From the training we can expect the ensemble to represent the latent heat transport well in today's climate. However, for the usefulness of the machine-learning model ensemble, it

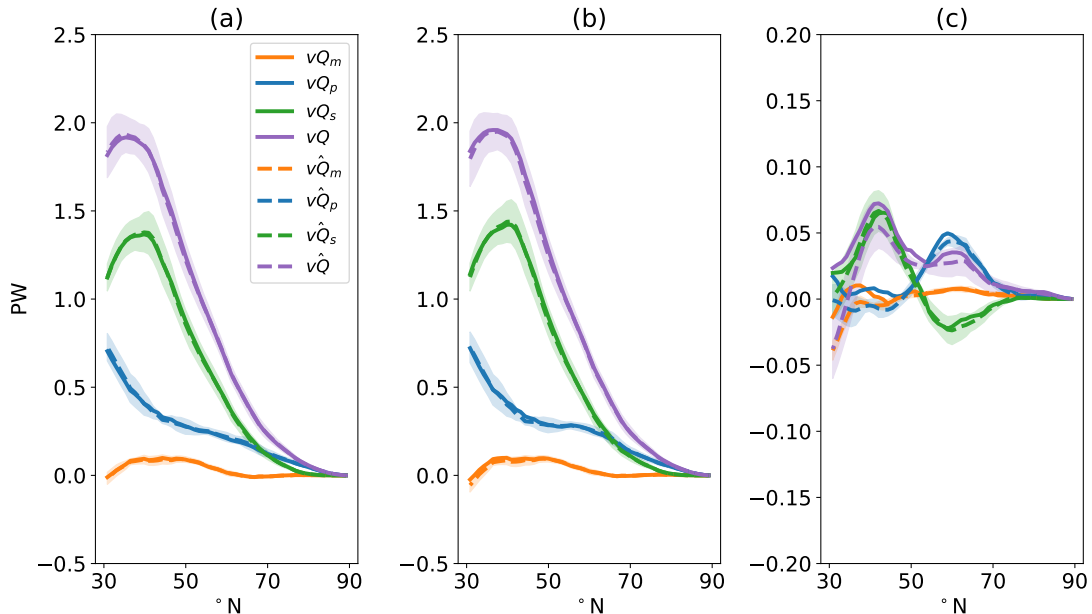


Figure 2: Validation of ERA5-trained resnet18 model ensemble on the first and last five years of ERA5 data. Panel (a) and (b) show the first five years, 1979-1983, and the last five years, 2014-2018, respectively, of the validation data, whereas panel (c) displays the difference between the later and the former period. The shadings show two times the standard deviation of the seven individually trained models. The classically computed are vQ_m : zonally symmetric, vQ_p : planetary, vQ_s : synoptic, and vQ : total latent energy transport. The hatted variables, $\hat{v}Q_m$, $\hat{v}Q_s$, $\hat{v}Q_p$, and $\hat{v}Q$ are equivalent but computed using the resnet18 ensemble.

should be capable of estimating the length-scale decomposition in other climate states as well. The change of the latent heat transport from the 1950s to 2090s is well captured by the resnet18 ensemble (Fig. 3 panel (c)).

It is important that the resnet18 ensemble estimates the mean meridional transports correctly as is verified by Fig. 2 and 3. However, to understand the effects of the transport on climate variables, an accurate estimate of the day-to-day variability of the transport components is needed. We test whether the daily variability of the resnet18 ensemble is realistic by calculating daily regressions of the zonal-mean two-meter temperature on the length-scale-decomposed latent heat transport. To assert the cause and effect relation between the latent heat transport and temperatures we use time lagged regressions of the temperature field on the components of the latent energy transport across 70°N . The regressions are computed for lags between -20 and 20 days. Negative time lags indicate regressions of temperatures before the transport anomaly across 70°N , and positive time lags indicate temperatures after. By comparing the regressions from the traditional computations of the length-scale decomposition (Fig. 4 (a) and (c)) with the regressions computed from the resnet18 ensemble latent heat transport (Fig. 4 (b) and (d)), it is evident that the main patterns of the time-lagged regressions are well captured. For planetary-scale transport, the maximum effect on temperature in the Arctic by both the clas-

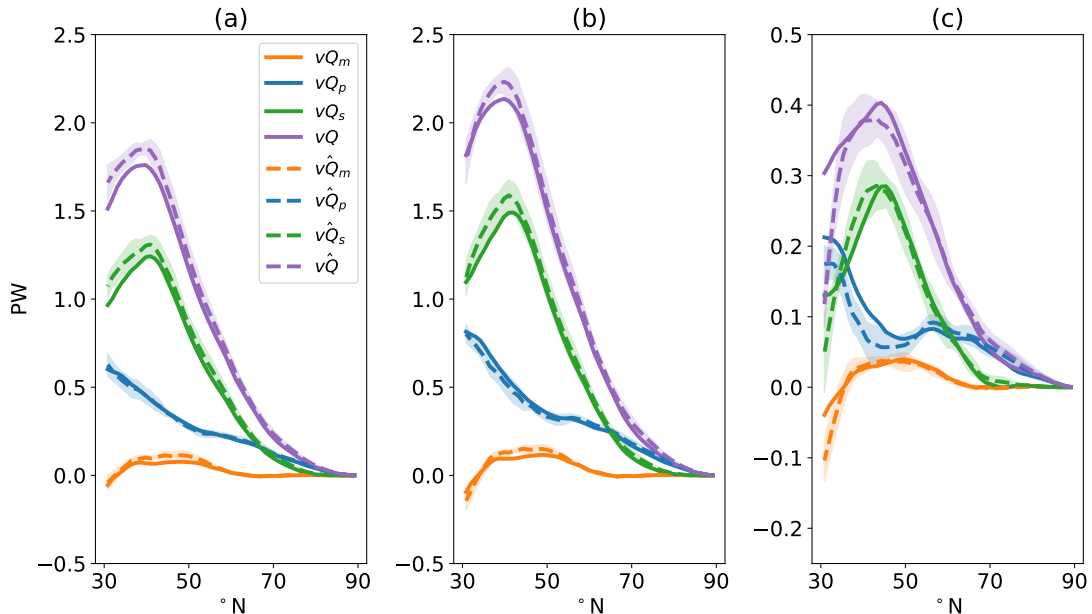


Figure 3: As in Fig. 2 but for test data from EC-Earth and for the first and last ten years of data, 1950-1959 and 2091-2100, respectively.

sically computed and resnet18-derived latent heat transport occurs five days after a transport anomaly across 70°N . For the synoptic-scale transport, the increased temperature gradient associated with baroclinic instability is present in both types of transport estimations. This physical linkage between synoptic scale transport and Arctic temperatures is discussed in further detail in Graversen and Burtu (2016). However, for both the synoptic and planetary-scale regressions, the coefficients computed from the resnet18 ensemble are somewhat more extreme than from the exact computations.

Discussion & Conclusion

Based on a comparison with classical and rather precise calculation of the components of the meridional latent energy transport (Fig. 2 and 3), and aspects of its daily variability (Fig. 4), it is evident that the resnet18 ensemble is a valid approach for estimation of the length-scale-decomposed meridional latent energy transport. The resnet18 method is computationally very efficient, especially compared the exact calculations based on reanalysis or model data. The difference in time efficiency lies mostly in the amount of data required for the two methods. The resnet18 ensemble requires a small fraction of the data that are needed for the complete computations of the energy transport decomposition. However, the resnet18 method approximates the energy transport whilst the classical computations yield almost exact estimates. Given that the approximation of the energy transport computed using the machine-learning approach is performing well, the reduced computing time relative to the classical computations opens for a range of possibilities. With the fast computations and small storage requirements, ensemble studies of the decomposed atmospheric energy transport are more feasible using the resnet18

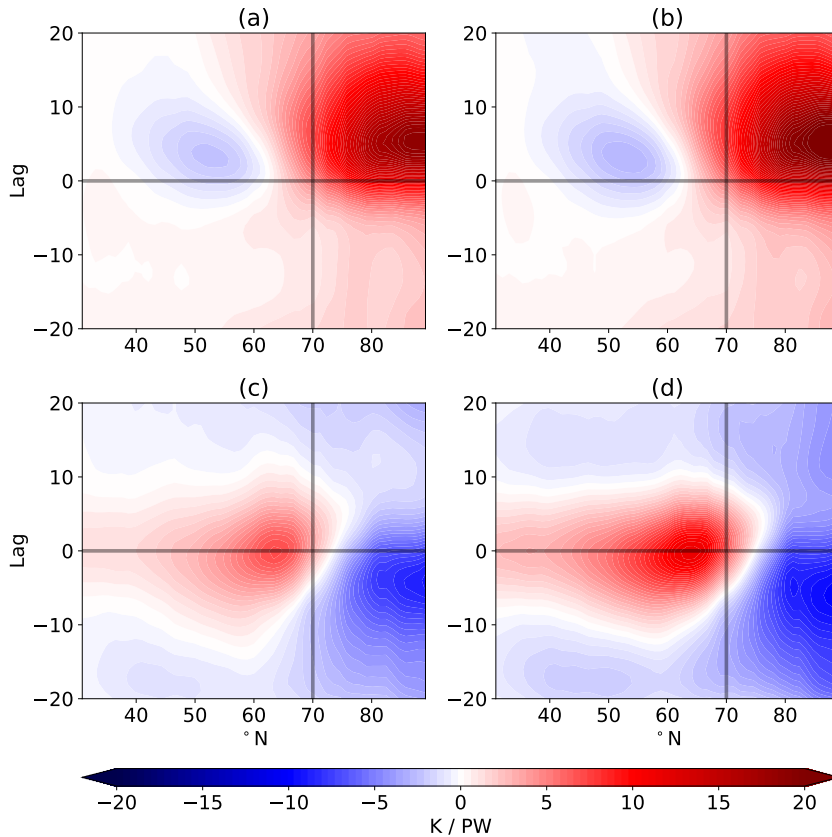


Figure 4: Regressions of temperature daily anomalies on anomalies of latent heat transport across 70°N based on EC-Earth. Panels (a) and (c) show the regressions based on the traditionally computed transport decomposition, where panel (a) shows planetary and panel (c) synoptic-scale regressions. Panels (b) and (d) show the equivalents, but for the transport computed using the resnet18 ensemble.

approach than the classical computations.

Earlier studies, e.g. Graversen and Burtu (2016) and Rydsaa et al. (2021), have investigated the changes in the decomposed energy transport in a changing climate using the classical computations. However, these studies are limited to reanalysis data and climate model experiments specifically designed for investigations of the energy transport changes. With the resnet18 approach, changes in the decomposed energy transport may be computed from previous experiments, which were not designed specifically for investigations of the energy transport. Hence, comparisons of the decomposed energy transport between models and different forcing experiments become feasible. This opens for instance for future studies of the energy transport changes for the models and experiments in the CMIP archives.

The network architecture in this study is just one of almost infinitely many possibilities. By no means do we claim that this model is the best of all the possible architectures. To achieve even better performance, the hyper-parameters of the model could be adjusted even more. In

addition, the model ensemble applied in this study only uses two atmospheric fields as input. Changing or adding atmospheric variables could also alter the performance of the model. Yet, the goal of this study was to investigate the feasibility of a machine-learning approach to estimate the energy transport decomposition. Based on the results of the study this is evidently possible and the results are surprisingly accurate given they are provided based on a small amount of data. The fact that the model trained on ERA5 is still able to accurately capture the energy transport in EC-Earth is promising for applications of the resnet18 on the CMIP archives.

It is promising that the resnet18 ensemble is capable of representing the energy transport in different climates than in which it was trained. Essentially machine-learning approaches like the resnet18 can potentially revolutionize the way we extract important climate variables from climate-model and reanalysis datasets. Although the resnet18 approach is not as accurate as the classical method, the calculation speed-up is immense. Hence the resnet18 approach is a useful tool, if one believes that the change in the decomposed atmospheric is important for an observed phenomenon we may compute the energy transport without the long computation times that the classical approach requires.

References

- Shun-Ichi Amari. Backpropagation and stochastic gradient descent method. *Neurocomputing*, 5(4):185–196, 1993. ISSN 0925-2312. doi: [https://doi.org/10.1016/0925-2312\(93\)90006-O](https://doi.org/10.1016/0925-2312(93)90006-O). URL <https://www.sciencedirect.com/science/article/pii/0925231293900060>.
- Cory Baggett and Sukyoung Lee. Arctic warming induced by tropically forced tapping of available potential energy and the role of the planetary-scale waves. *Journal of the Atmospheric Sciences*, 72(4):1562 – 1568, 2015. doi: 10.1175/JAS-D-14-0334.1. URL <https://journals.ametsoc.org/view/journals/atsc/72/4/jas-d-14-0334.1.xml>.
- V. Eyring, S. Bony, G. A. Meehl, C. A. Senior, B. Stevens, R. J. Stouffer, and K. E. Taylor. Overview of the coupled model intercomparison project phase 6 (cmip6) experimental design and organization. *Geoscientific Model Development*, 9(5):1937–1958, 2016. doi: 10.5194/gmd-9-1937-2016. URL <https://gmd.copernicus.org/articles/9/1937/2016/>.
- S. Ferrari and R.F. Stengel. Smooth function approximation using neural networks. *IEEE Transactions on Neural Networks*, 16(1):24–38, 2005. doi: 10.1109/TNN.2004.836233.
- R. G. Graversen. Do changes in the midlatitude circulation have any impact on the arctic surface air temperature trend? *Journal of Climate*, 19(20):5422 – 5438, 2006. doi: 10.1175/JCLI3906.1. URL <https://journals.ametsoc.org/view/journals/clim/19/20/jcli3906.1.xml>.
- Rune G. Graversen and Mattias Burtu. Arctic amplification enhanced by latent energy transport of atmospheric planetary waves. *Quarterly Journal of the Royal Meteorological Society*, 142(698):2046–2054, 2016. doi: <https://doi.org/10.1002/qj.2802>. URL <https://rmets.onlinelibrary.wiley.com/doi/abs/10.1002/qj.2802>.
- W. Hazeleger, X. Wang, C. Severijns, S. Ștefănescu, R. Bintanja, A. Sterl, K. Wyser, T. Semmler, S. Yang, B. van den Hurk, T. van Noije, E. van der Linden, and K. van der Wiel. Ec-earth v2.2: description and validation of a new seamless earth system prediction model. *Climate Dynamics*, 39(11):2611–2629, Dec 2012. ISSN 1432-0894. doi: 10.1007/s00382-011-1228-5. URL <https://doi.org/10.1007/s00382-011-1228-5>.

- Wilco Hazeleger, Camiel Severijns, Tido Semmler, Simona Ștefănescu, Shuting Yang, Xueli Wang, Klaus Wyser, Emanuel Dutra, José M. Baldasano, Richard Bintanja, Philippe Bougeault, Rodrigo Caballero, Annica M. L. Ekman, Jens H. Christensen, Bart van den Hurk, Pedro Jimenez, Colin Jones, Per Källberg, Torben Koenigk, Ray McGrath, Pedro Miranda, Twan van Noije, Tim Palmer, José A. Parodi, Torben Schmith, Frank Selten, Trude Storelvmo, Andreas Sterl, Honoré Tapamo, Martin Vancoppenolle, Pedro Viterbo, and Ulrika Willén. Ec-earth: A seamless earth-system prediction approach in action. *Bulletin of the American Meteorological Society*, 91(10):1357 – 1364, 2010. doi: 10.1175/2010BAMS2877.1. URL https://journals.ametsoc.org/view/journals/bams/91/10/2010bams2877_1.xml.
- Kaiming He, Xiangyu Zhang, Shaoqing Ren, and Jian Sun. Deep residual learning for image recognition. In *Proceedings of the IEEE Conference on Computer Vision and Pattern Recognition (CVPR)*, June 2016.
- Tuomas Heiskanen, Rune Grand Graversen, Johanne Hope Rydsaa, and Pål Erik Isachsen. Comparing wavelet and fourier perspectives on the decomposition of meridional energy transport into synoptic and planetary components. *Quarterly Journal of the Royal Meteorological Society*, 146(731):2717–2730, 2020. doi: <https://doi.org/10.1002/qj.3813>. URL <https://rmets.onlinelibrary.wiley.com/doi/abs/10.1002/qj.3813>.
- Hans Hersbach, Bill Bell, Paul Berrisford, Shoji Hirahara, András Horányi, Joaquín Muñoz-Sabater, Julien Nicolas, Carole Peubey, Raluca Radu, Dinand Schepers, Adrian Simmons, Cornel Soci, Saleh Abdalla, Xavier Abellan, Gianpaolo Balsamo, Peter Bechtold, Gionata Biavati, Jean Bidlot, Massimo Bonavita, Giovanna De Chiara, Per Dahlgren, Dick Dee, Michail Diamantakis, Rossana Dragani, Johannes Flemming, Richard Forbes, Manuel Fuentes, Alan Geer, Leo Haimberger, Sean Healy, Robin J. Hogan, Elías Hólm, Marta Janisková, Sarah Keeley, Patrick Laloyaux, Philippe Lopez, Cristina Lupu, Gabor Radnoti, Patricia de Rosnay, Iryna Rozum, Freja Vamborg, Sebastien Villaume, and Jean-Noël Thépaut. The era5 global reanalysis. *Quarterly Journal of the Royal Meteorological Society*, 146(730):1999–2049, 2020. doi: <https://doi.org/10.1002/qj.3803>. URL <https://rmets.onlinelibrary.wiley.com/doi/abs/10.1002/qj.3803>.
- Yen-Ting Hwang, Dargan MW Frierson, and Jennifer E Kay. Coupling between arctic feedbacks and changes in poleward energy transport. *Geophysical Research Letters*, 38(17), 2011.
- M. I. Jordan and T. M. Mitchell. Machine learning: Trends, perspectives, and prospects. *Science*, 349(6245):255–260, 2015. doi: 10.1126/science.aaa8415. URL <https://www.science.org/doi/abs/10.1126/science.aaa8415>.
- Torben Koenigk, Laurent Brodeau, Rune Grand Graversen, Johannes Karlsson, Gunilla Svensson, Michael Tjernström, Ulrika Willén, and Klaus Wyser. Arctic climate change in 21st century cmip5 simulations with ec-earth. *Climate dynamics*, 40(11):2719–2743, 2013.
- Stephan Rasp and Nils Thuerey. Data-driven medium-range weather prediction with a resnet pretrained on climate simulations: A new model for weatherbench. *Journal of Advances in Modeling Earth Systems*, 13(2):e2020MS002405, 2021. doi: <https://doi.org/10.1029/2020MS002405>. URL <https://agupubs.onlinelibrary.wiley.com/doi/abs/10.1029/2020MS002405>. e2020MS002405 2020MS002405.
- J. H. Rydsaa, R. G. Graversen, T. I. H. Heiskanen, and P. J. Stoll. Changes in atmospheric latent energy transport into the arctic: Planetary versus synoptic scales. *Quarterly Journal of the*

Royal Meteorological Society, 147(737):2281–2292, 2021. doi: <https://doi.org/10.1002/qj.4022>. URL <https://rmets.onlinelibrary.wiley.com/doi/abs/10.1002/qj.4022>.

S. Scher and G. Messori. Weather and climate forecasting with neural networks: using general circulation models (gcms) with different complexity as a study ground. *Geoscientific Model Development*, 12(7):2797–2809, 2019. doi: 10.5194/gmd-12-2797-2019. URL <https://gmd.copernicus.org/articles/12/2797/2019/>.

Theodore G. Shepherd. Atmospheric circulation as a source of uncertainty in climate change projections. *Nature Geoscience*, 7(10):703–708, Oct 2014. ISSN 1752-0908. doi: 10.1038/ngeo2253. URL <https://doi.org/10.1038/ngeo2253>.

Karl E. Taylor, Ronald J. Stouffer, and Gerald A. Meehl. An overview of cmip5 and the experiment design. *Bulletin of the American Meteorological Society*, 93(4):485 – 498, 2012. doi: 10.1175/BAMS-D-11-00094.1. URL <https://journals.ametsoc.org/view/journals/bams/93/4/bams-d-11-00094.1.xml>.

Kevin E. Trenberth. Climate diagnostics from global analyses: Conservation of mass in ecmwf analyses. *Journal of Climate*, 4(7):707 – 722, 1991. doi: 10.1175/1520-0442(1991)004<0707: CDFGAC>2.0.CO;2. URL https://journals.ametsoc.org/view/journals/clim/4/7/1520-0442_1991_004_0707_cdfgac_2_0_co_2.xml.

Kevin E. Trenberth and Julie M. Caron. Estimates of meridional atmosphere and ocean heat transports. *Journal of Climate*, 14(16):3433–3443, 2001. doi: 10.1175/1520-0442(2001)014<3433:EOMAAO>2.0.CO;2. URL https://journals.ametsoc.org/view/journals/clim/14/16/1520-0442_2001_014_3433_eomaa_2_0_co_2.xml.

Jonathan A. Weyn, Dale R. Durran, and Rich Caruana. Can machines learn to predict weather? using deep learning to predict gridded 500-hpa geopotential height from historical weather data. *Journal of Advances in Modeling Earth Systems*, 11(8):2680–2693, 2019. doi: <https://doi.org/10.1029/2019MS001705>. URL <https://agupubs.onlinelibrary.wiley.com/doi/abs/10.1029/2019MS001705>.

Jonathan A. Weyn, Dale R. Durran, Rich Caruana, and Nathaniel Cresswell-Clay. Sub-seasonal forecasting with a large ensemble of deep-learning weather prediction models. *Journal of Advances in Modeling Earth Systems*, 13(7):e2021MS002502, 2021. doi: <https://doi.org/10.1029/2021MS002502>. URL <https://agupubs.onlinelibrary.wiley.com/doi/abs/10.1029/2021MS002502>. e2021MS002502 2021MS002502.

